DISSERTATION

STUDIES OF OCEANIC, ATMOSPHERIC, CRYOSPHERIC, AND FLUVIAL PROCESSES THROUGH SPECTRAL ANALYSIS OF SEISMIC NOISE

Submitted by

Robert Ernest Anthony

Department of Geosciences

In partial fulfillment of the requirements

For the Degree of Doctor of Philosophy

Colorado State University

Fort Collins, Colorado

Fall 2016

Doctoral Committee:

Advisor: Richard Aster

Derek Schutt
David Thompson
David Reusch

ABSTRACT

STUDIES OF OCEANIC, ATMOSPHERIC, CRYOSPHERIC, AND FLUVIAL PROCESSES THROUGH SPECTRAL ANALYSIS OF SEISMIC NOISE

During the past decade, there has been rapidly growing interest in using the naturally occurring seismic noise field to study oceanic, atmospheric, and surface processes. As many seismic noise sources, are non-impulsive and vary over a broad range of time scales (e.g., minutes to decades), they are commonly analyzed using spectral analysis or other hybrid time-frequency domain methods. The PQLX community data analysis program, and the recently released Noise Tool Kit that I co-developed with Incorporated Research Institutions for Seismology's Data Management Center are used here to characterize seismic noise for a variety of environmental targets across a broad range of frequencies.

The first two chapters of the dissertation place a strong emphasis on analysis of environmental microseism signals, which occur between 1-25 s period and are dominated by seismic surface waves excited by multiple ocean-solid Earth energy transfer processes. I move away from microseisms in Chapter 3 to investigate the generally higher frequency seismic signals (> 0.33 Hz) generated by fluvial systems.

In Chapter 1, I analyze recently collected, broadband data from temporary and permanent Antarctic stations to quantitatively assess background seismic noise levels across the continent between 2007-2012, including substantial previously unsampled sections of the Antarctic

continental interior. I characterize three-component noise levels between 0.15-150 s using moving window probability density function-derived metrics and analyze seismic noise levels in multiple frequency bands to examine different noise sources. These metrics reveal and quantify patterns of significant seasonal and geographic noise variations across the continent, including the strong effects of seasonal sea ice variation on the microseism, at a new level of resolution. Thorough analysis of the seismic noise environment and its relation to instrumentation and siting techniques in the Polar Regions facilitates new science opportunities and the optimization of deployment strategies for future seismological research in the Polar Regions, and in mountain glacier systems.

Chapter 2 details the analysis of 23 years of microseism observations on the Antarctic Peninsula to investigate wave-sea ice interactions and assess the influence of the Southern Annular Mode (SAM) on storm activity and wave state in the Drake Passage. The lack of landmasses, climatological low pressure, and strong circumpolar westerly winds between latitudes of 50°S to 65°S produce exceptional Southern Ocean storm-driven wave conditions. This combination makes the Antarctic Peninsula one of Earth's most notable regions of high amplitude wave activity and one of the planet’s strongest sources of ocean-swell driven microseism noise in both the primary (direct wave-coastal region interactions) and secondary (direct ocean floor forcing due to interacting wave trains) period bands. Microseism observations are examined from 1993-2015 from long running seismographs located at Palmer Station (PMSA), on the west coast of the Antarctic Peninsula, and from the sub-Antarctic East Falkland Island (EFI). These records provide a spatially integrative measure of Southern Ocean amplitudes and of the degree of coupling between ocean waves and the solid earth with and without the presence of sea ice

(which can reduce wave coupling with the continental shelf). A spatiotemporal correlation-based approach illuminates how the distribution of sea ice influences seasonal primary and secondary microseism power. I characterize primary and secondary microseism power due to variations in sea ice, and find that primary microseism energy is both more sensitive to sea ice and more capable of propagating across ocean basins than secondary microseism energy. During positive phases of the SAM, sea ice is reduced in the Bellingshausen Sea and overall storm activity in the Drake Passage increases, resulting in strongly increased microseism power levels.

The field of fluvial seismology has emerged during the past decade, with seismic recordings near fluvial systems showing potential for a continuous, inexpensive, and non-invasive method of measuring flow and, in some cases, bed-load transport, in streams and rivers. In Chapter 3, I extend this research to the South Fork of the Cache la Poudre River in Northern Colorado where I deployed a small seismoaccoustic array while simultaneous measurements of discharge, suspended sediment concentrations, and precipitation were obtained. By placing seismometers within unprecedented proximity to the channel (~ 1 m, and during some time periods submerged), I found a broad range of frequencies excited by discharge, including novel, low-frequency (< 1 Hz) signals. After calibrating horizontal seismic power with flow rates over the course of a rainstorm event for individual sensors, I show that horizontal seismogram power in the 0.33-2 Hz band can be used to accurately invert for fluvial discharge with simple regressions, once a site is properly calibrated to a traditional hydrograph. These signals likely arise from local sensor tilt as the seismometer is directly forced by channel flow and show promise for augmenting seismic monitoring of fluvial systems by introducing a technique to estimate discharge rates from outside the channel with easily deployed noninvasive instrumentation.

ACKNOWLEDGEMENTS

Foremost, I would like to thank my advisor, Rick Aster, for his continual support, guidance, and inspiration over the course of the Ph.D. I also thank my committee members Derek Schutt, David Thompson, and David Reusch for their insight and time. The seismological community has been extraordinarily supportive of my work during the dissertation and the work presented here would not have been possible without the mentorship and assistance of Noel Barstow, Manoch Bahavar, Aaron Curtis, Michael Hubenthal, Jeff Johnson, Pnina Miller, Tim Parker, Patrick Shore, and Adam Ringler. Finally, I thank my wife, family, and friends for their unending love and support. To my late grandpa, Dr. Robert Purbrick, thank you for instilling me with a passion for the natural sciences, you are greatly missed.

The facilities of the IRIS Data Management System, and specifically the IRIS Data Management Center, were used for access to all waveform and metadata required in this dissertation. Sea ice concentration data around Antarctica used in Chapters 1 and 2 were obtained from The National Snow and Ice Data Center (NSIDC). The Global Seismographic Network (GSN) is a cooperative scientific facility operated jointly by the Incorporated Research Institutions for Seismology (IRIS), the United States Geological Survey (USGS), and the National Science Foundation (NSF). The facilities of the IRIS Consortium are supported by the National Science Foundation under Cooperative Agreement EAR-1063471, NSF Polar Programs, and the Department of Energy National Nuclear Security Administration. POLENET-Antarctica phase 1 was supported by NSF Polar Programs grant numbers 0632230, 0632239, 0652322, 0632335, 0632136, 0632209, 0632185, and POLENET-Antarctica phase 2 is supported by NSF Polar Programs

grant numbers 1246776 1246712 and 1419268. Additional funding was provided by Los Alamos National Laboratory through the Institute of Geophysics, Planetary Physics. Additional information regarding the POLENET project, data collection sites, and geophysical data is available at polenet.org.

Author Contributions

This dissertation contains contributions from multiple individuals. David Reusch acquired and prepared the sea ice data used in Chapter 2. Figure 2.1 and parts of the introduction of Chapter 2 were prepared by Dan McGrath. Sandra Ryan collected and prepared the discharge, suspended sediment, and precipitation data presented in Chapter 3 with assistance from several Colorado State University (CSU) employees and students including Sara Rathburn, David Dust, Bryce Johnson, Jay Merrill, Michael Wyatt, and Brianna Van. Additional field assistance deploying and servicing the seismoaccoustic array was provided by Michael Baker and Holden Dilalla. Richard Aster performed editing to all chapters, took the photos used in Figure 3.1, and contributed portions of the MATLAB code used in Chapter 3.

TABLE OF CONTENTS

General Introduction to Seismic Noise

The unpredictable nature of earthquakes occurring on faults across the planet necessitates continuous observations from seismic instrumentation. Traditionally, the goals of earthquake monitoring have been to either characterize the earthquake event (e.g., location, size, fault rupture characteristics) or use the seismic waves radiated from the earthquake to study earth structure (e.g., crustal thickness, mantle structure). However, in the absence of earthquakes seismometers record a wide range of signals generated from both natural and anthropogenic sources as well as from the instrument itself. As these signals have the capability of interfering with the ability to record earthquakes, they have been lumped together and given the term "seismic noise."

The broad spectrum of seismic noise can be divided into three general period bands: short period (< 1 s), intermediate period (1-20 s), and long period (>20 s) (e.g., Figure 1.2). Noise sources in the short period band are often dominated by anthropogenic noise contamination and seismic coupling due to wind, making it frequently difficult to isolate small seismic signals (e.g., *Li et al.*, 1984; *Galperin et al.*, 1986; *Peterson,* 1993; *Withers et al.*, 1996; *Wilson et al.*, 2002). Diurnal changes in anthropogenic noise have been shown to drastically change detection level thresholds and accuracy of phase picks for local and regional seismic events (e.g., *Zeiler and Velasco*, 2009; *McMahon et al.*, 2016; *Demuth et al.,* 2016). For instance, elevated daytime noise levels at stations near cities raised earthquake detection thresholds by M_L 0.75, and differences in background high frequency noise levels between individual stations caused detections thresholds to be raised by M_L 2.0 at noisy versus quiet sites (*Demuth et al.*, 2016). Thus, characterization of

seismic noise sources can have important implications for the design and placement of instruments in seismic networks. This type of analysis was a prime-motivating factor in my first study "The Seismic Noise Environment of Antarctica" (Chapter 1), as year-round data had just begun to be recovered from remote sectors of the Antarctic interior by the NSF-funded POLENET, AGAP, and other large seismograph deployments, and little was known about how seismometer emplacement styles in the Antarctic environment influenced the quality of seismic records. As I worked through these projects, and deployed instruments in the field, I became interested in using seismic noise in Antarctica as a means to not only measure station signal-to-noise for traditional earthquake detection and research, but as a way to assess Southern Ocean wave state and sea ice concentration around Antarctica.

Noise generated by ocean waves, known as microseisms, is a ubiquitous feature of the intermediate seismic period band on seismometers across the globe. Microseisms have long been subdivided into processes associated with the direct coupling of waves crashing against the continental shelf (primary microseism, approximately 13-20 s period; e.g*., Hasselmann*, 1963) and with wave-wave interactions as opposing wave trains interfere with each other and set up standing pressure oscillations on the seafloor (secondary microseism, approximately 5-10 s period; e.g., *Longuet-Higgins*, 1950). However, as the strength of microseism signals can be directly related to ocean wave state, several recent studies have begun using microseism observations as a direct proxy for near-coastal wave height (e.g., *Zhang et al., 2009*; *Ardhuin et al., 2012; Ferretti et al.,* 2016) and to assess changes in regional or global wave activity over the past several decades (e.g., *Aster et al*., 2008, 2010; *Stutzmann et al.*, 2009). During the last decade, the field of "environmental seismology" has been born as a field in which seismic

observation are utilized to study and track changing conditions within Earth's atmosphere, hydrosphere, and cryosphere (e.g., *Larose et al*., 2015).

For instance, because the formation of sea ice around the coastlines of Polar Regions can inhibit ocean waves from transferring energy to the solid earth, microseism observations from seismic stations in Antarctica and the Arctic have been suggested as a proxy for tracking near-coastal sea ice strength (*Tsai and McNamara,* 2011). In the past few years, researchers have become increasingly interested in ocean wave-sea ice-coastal interactions as the Arctic has experienced rapid reductions in summer sea ice concentrations. These reductions in sea ice create larger expanses of open ocean, which enables the generation of larger wind-driven oceanic waves that likely have the capability to further breakup sea ice and erode shorelines. Thus, the potential for a positive feedback loop between ocean wave activity and sea ice loss exists (*Asplin et al.,* 2012; *Thompson and Rogers*, 2014) and has sparked strong interest in observational studies of wave-sea ice interactions (e.g., *Kohout et al.*, 2014; *Mahoney et al.*, 2016). However, such in situ measurements and observations are rare, particularly for the Southern Ocean. In Chapter 2 of the dissertation, "Links Between Atmosphere, Ocean, and Cryosphere from two Decades of Microseism Observations on the Antarctic Peninsula," I explore the use of historical microseism records across more than two decades as a proxy for measuring wave-sea ice interactions and for determining regional microseism source locations. I also illustrate how modes of atmospheric variability can have a drastic impact on storm and wave activity as well as sea ice concentrations. These observations contribute to advance understanding of coupled climate systems and should aid future use of microseism observations to compliment and extend satellite observations of changes in wave state, storm activity, and sea ice.

More locally and on shorter time scales, seismic observations have also begun to be investigated for use in monitoring and quantifying geomorphological processes such as coastal erosion (e.g., *Adams et al.*, 2005; *Norman et al.*, 2013; *Poppeliers and Mallinson*; 2015); glacial calving, slip events, and icestream dynamics (e.g., *O'Neel et al.,* 2007; *Wiens et al.,* 2008; *Winberry et al.*, 2009); and fluvial discharge and sediment transport (e.g., *Burtin et al.*, 2008, 2011; *Hsu et al.,* 2011; *Schmandt et al.*, 2013; *Roth et al*., 2016). In contrast to microseism observations, the new field of "fluvial seismology" commonly uses short period (< 1 s) signals recorded by seismometers located in close proximity to rivers (<50 m) to infer changes in bedload transport and discharge. Previous work has been limited to predominantly larger (>100 m^3/s) fluvial systems (*Hsu et al.,* 2011; *Schmandt et al.*, 2013) and/or where discharge rates are poorly resolved (*Burtin et al*., 2008; *Bartholomaus et al.,* 2015). In Chapter 3 of the dissertation, "Seismic Monitoring of Snowmelt Runoff in the Northern Colorado Rocky Mountains," these earlier studies are extended to a small (1-16 m^3/s) and largely snowmelt-fed stream with co-located measurements of discharge, precipitation, and suspended sediment levels. By placing the sensors in exceptionally close proximity to the stream (~1 m), a novel source of longer-period (0.5-3.3 s) seismic noise that correlates remarkably well with discharge is revealed, so that a synthetic seismic hydrograph can be readily produced. Additionally, it is shown that suspended sediment loads of this system (which are small and very fine grained) are not identified in the seismic record. These findings should be beneficial to the design of future networks that incorporate seismic observations to continuously monitor fluvial systems.

Although the range of systems examined in the dissertation ranges from continent-wide studies of sea ice around Antarctica to monitoring discharge and sediment transport along ~50 m on the

Colorado River, the studies are all tied together by the common theme of using spectral analysis to characterize continuous seismic signals that arises through environmental processes. As many seismic noise sources are non-impulsive and often persist for long-durations, they are traditionally analyzed in the frequency domain (rather than analyzing waveform/time series data) usually in the form of moving-window power spectral density (PSD) spectrograms. Identifying meaningful sources of noise requires performing specialized spectral analysis techniques designed to return relatively smooth spectra with a tractable number of Fourier coefficients while mitigating spectral leakage (e.g., *Oppenheim and Schafer*, 1975; *McNamara and Buland*, 2004). Additionally, to track seasonal-to-decadal variations in noise levels; it becomes necessary to process large amounts of seismological data to resolve and interpret small changes in the seismic noise field.

The United States Geological Survey, the Incorporated Research Institutions for Seismology (IRIS), and academic researchers widely employ a version of the community software package PQLX (e.g., *McNamara and Boaz*, 2011) to evaluate the spectral amplitudes of noise recorded on seismometers over long time periods. However, PQLX has limitations in characterizing seismic noise recorded on long-running networks such as 1) requiring local archival of all time series data (~4 GB per year per station of 3-component 40 sample per second data), 2) inability to specify window lengths and smoothing parameters used in PSD estimation, 3) limited user support, and 4) a sometimes fragile MySQL database/framework. To overcome these problems, I worked directly with the IRIS Data Management Center (DMC) to develop an open Python-based community noise processing toolkit (NTK) that enables customization of spectral amplitude estimates as well as direct data processing from the DMC servers (*Bahavair et al.*,

2013). The NTK is used to perform spectral analysis in Chapters 2-3 of the dissertation and mimics the output format of PQLX. The availability of a user-friendly platform for spectral analysis, with the capability of performing near-real spectral estimates has many applications to environmental seismology. As different environmental targets excite different frequencies of interest, which vary on a wide range of time scales, the NTK was designed to enable selection of a wide range of PSD window lengths and smoothing options. The tradeoff that inherently occurs between spectral resolution and confidence in spectral estimates and how spectral estimates used in this dissertation are calculated to ensure reproducibility is discussed in Appendix 1. I discuss some applications of performing spectral analysis through the NTK such as monitoring global wave state and local sea ice conditions in the "Epilogue and Future Directions" (Chapter 4) of the dissertation.

Chapter 1: The Seismic Noise Environment of Antarctica[1]

Introduction

Seismographic coverage of Antarctica prior to 2007 consisted overwhelmingly of a handful of long running and sporadically-deployed transient stations, many of which were principally co-located with scientific research stations. Despite very cold temperatures, sunless winters, limited logistics, and extreme storms, recent developments in polar instrumentation driven by new scientific objectives have opened up the entirety of Antarctica to year-round and continuous seismological observation (e.g., Nyblade et al., 2012).

Motivations for these recent studies include improved understanding of seismogenic, volcanic, tectonic and glaciological processes, heat flow, dynamic glaciological/ocean interactions, and mantle viscosity. Such studies contribute generally to improvements in understanding the geophysical, geological, and glaciological history of the continent and how these processes interact with the past and present state of the glaciological and climate system (*e.g., Winberry et al.*, 2009; *West et al.*, 2010; *Hansen et al.*, 2010; *Winberry et al.*, 2011; *Chaput et al.,* 2013; *Heeszel et al.*, 2013; *Lough et al.,* 2013, *Accardo et al.,* 2014), including processes relevant to glacial isostatic adjustment and sea level rise (IPCC Report, 2007). Additionally, microseisms arising from ocean wave activity contain useful climate proxy information on the state and variability of the relatively poorly sensed southern oceans (*Aster et al.,* 2008; *Stutzmann et al*.,

[1] Published as: Anthony, R., Aster, R.C., Wiens, D., Nyblade, A., Anandakrishnan, S., Huerta, A., Winberry, J., Wilson, T., Rowe, C (2015), The seismic noise environment of Antarctica, *Seism. Res. Lett*., **86**.

2009; *Aster et al*., 2010) and such observations are sensitive to sea ice concentration and areal coverage in the polar regions (*Grob et al*., 2011; *Tsai and McNamara*, 2011; *Koch et al.*, 2013). This characterization of the seismic noise environment of Antarctica, documentation of instrument performance, and comparisons of installation conditions (e.g., ice vaults vs. rock sites) is intended to facilitate optimization of future seismological deployments in such environments. We analyze data from a range of recent experiments to provide a broad geographical characterization of Antarctica's seismic noise environment, which can now include more substantial observations from regions that are free from anthropogenic noise contamination.

Methods

i. Data Collection and Analysis

The Polar Earth Observing Network (POLENET ANET) and Gamburtsev Antarctic Mountains Seismic Experiment (GAMSEIS/AGAP) (e.g., *Heeszel et al.*, 2013; *Lloyd et al.*, 2013; *Wiens et al.*, 2013; *Chaput et al*., 2014) deployments of year-round temporary seismic stations have strongly contributed to improving the broadband seismic coverage of Antarctica (Figure 1.1). Stations in POLENET ANET and GAMSEIS/AGAP were first deployed in December 2007 and have continued through the present. Although most stations were deployed in snow vaults, some sensors, particularly in the Transantarctic Mountains (TAM) were installed directly on isolated rock outcrops, permitting some data quality comparisons to be performed between the two siting environments. All rock- and ice-sited temporary stations analyzed here were equipped with either Nanometrics Trillium 240 or Guralp cold-modified CMG-3T broadband sensors.

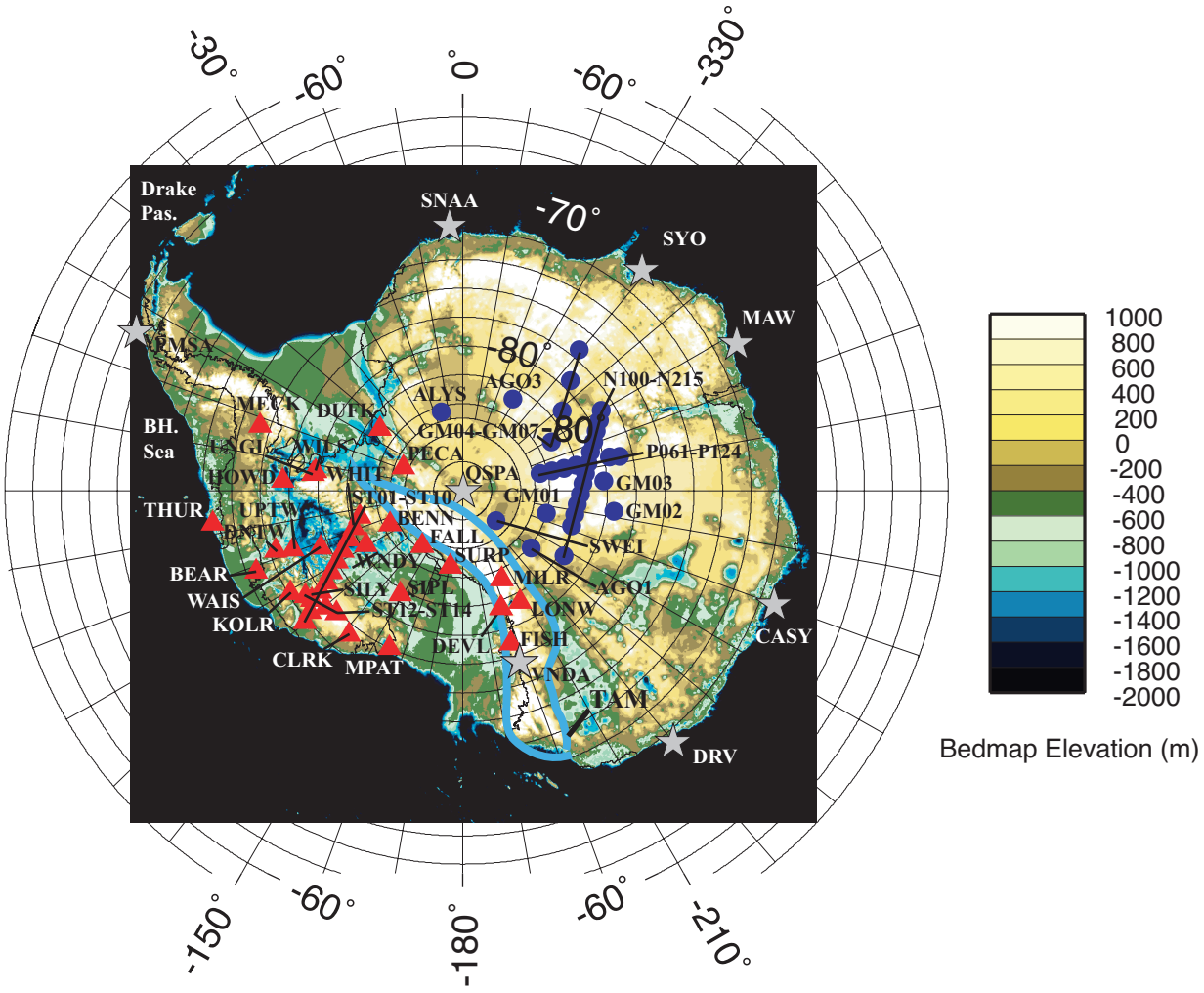

Figure 1.1 POLENET ANET (red triangles) and GAMSEIS/AGAP (blue circles) year-round seismic stations deployed since 2007. Prior to 2007, coverage was substantially limited to longer-operating stations sited near scientific bases (gray stars) and confined to the coast (with the exception of South Pole; QSPA). The Transantartic Mountains (TAM) are outlined in blue and the Bellingshausen Sea (BH. Sea) and Drake Passage (Drake Pas.) are noted near the Antarctic Penninsula. Background colormap represents bedmap elevation relative to sea level.

To characterize and analyze the seismic background of Antarctica, we examined all available 40 and 20 Hz sampling rate seismic data from 77 stations (9 permanent sites, 38 POLENET, 30 AGAP) between 2007 and 2012 using data retrieved from IRIS Data Services. The seismic time series were then used to generate acceleration power spectral densities (PSDs; in dB relative to 1 $m^2/s^4/Hz$) and PSD probability density functions (PDFs) using the methodology of *McNamara and Buland* (2004) through the software package PQLX (*McNamara and Boaz,* 2011; Figure 1.2). The PSD estimation procedure deconvolves the instrument response from archived continuous time series. 1-hr, 50% overlapping time segments are windowed into 13 sub-segments with 75% overlap. Each sub-segment is demeaned, detrended, and a 10% cosine taper is applied to reduce spectral leakage. Welch's section averaging method is utilized to estimate the PSD (e.g., *Oppenheim and Schafer,* 1975) for each 1-hr segment using the 13 sub-segments. Empirical PDFs are constructed by binning periods in 1/8-octave intervals and power in 1 dB intervals, and normalizing by the total number of PSDs. PSD PDFs and other statistics are referenced to the *Peterson* (1993) global new high- and low-noise models (NHNM, NLNM) for broader global comparison.

PSD PDFs are insightful and compact data representations for examining instrumentation and data quality as well as seismic signals and noise levels. To identify background noise conditions the PSD population was culled of obvious instrumentation artifacts associated with downtime and malfunctions. This was achieved, when necessary, by automatically identifying characteristically anomalous PSDs which contained power levels within the robust secondary microseism band that exceeded the 98^{th} percentile statistics in every period bin or that fell below median NLNM power in at least 50% or the period bins. Such PSDs were attributed to common

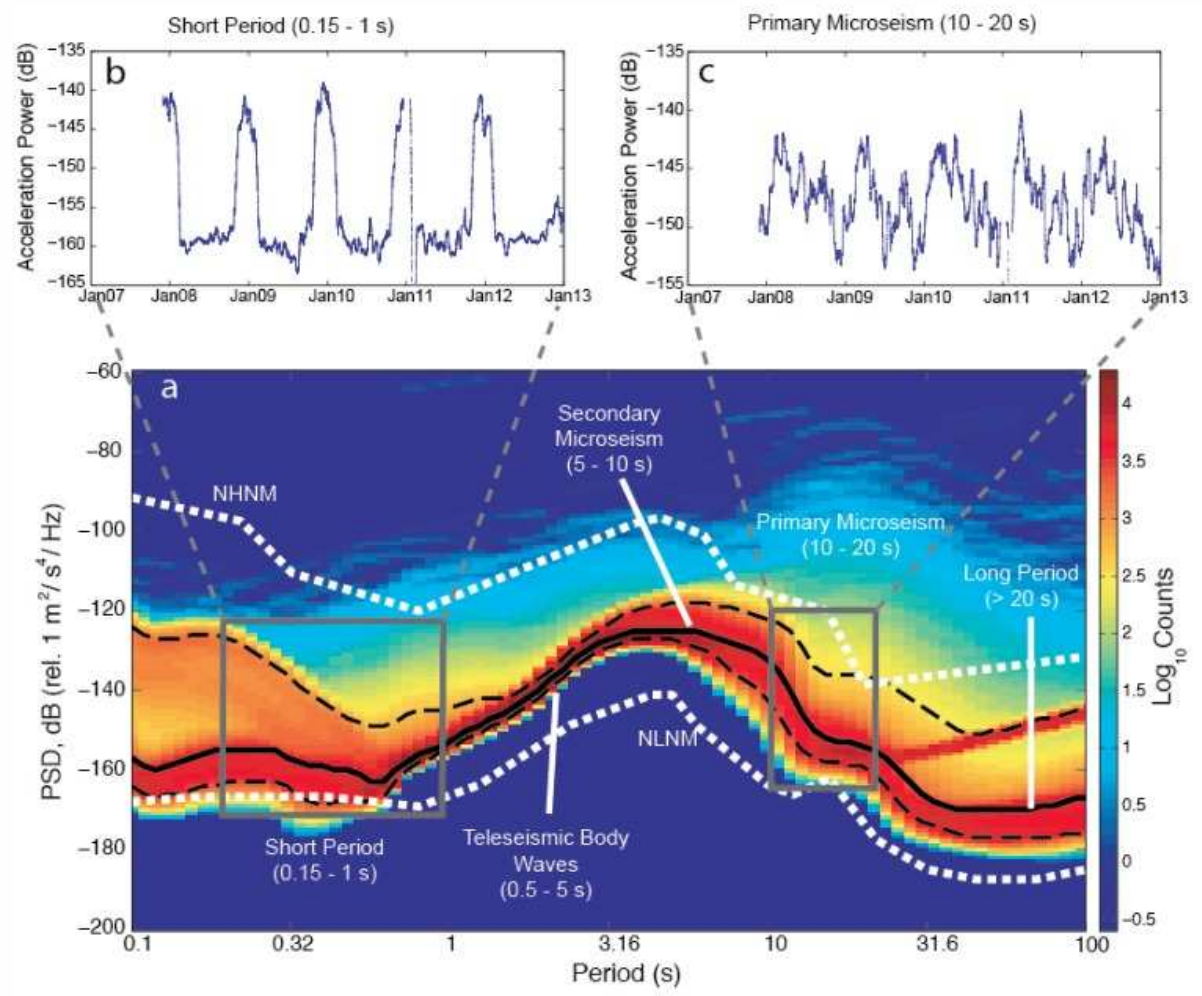

Figure 1.2. (a) Probability density function (PDF) of power spectral density (PSD) for the vertical-component of South Pole station QSPA (146 m borehole) for December 2007–December 2012 plotted on a logarithmic color scale to show transient high-amplitude signals (e.g., teleseismic earthquakes) and other probabilistically secondary features. The median PSD is plotted (solid black line) as well as 5th and 95th percentile statistics (dashed lines) and are compared to the global high- and low-noise models (NHNM, NLNM) of *Peterson* (1993). Additionally, the six period bands referred to in the text are labeled. Temporal evolutions in power in the short-period **(b)** and primary microseism band **(c)** are shown to illustrate the influence of seasonal anthropogenic noise at nearby (7.8 km) Amundsen-Scott South Pole Station and the unique seasonality (phase shifted ~90° from the rest of the southern hemisphere; *Aster et al.,* 2008) of the Antarctic microseism signal due to the annual growth and decay of sea ice.

instrumentation artifacts such as mass re-centers, calibrations (e.g., *McNamara and Buland*, 2004), and to intermittent data dropouts due to power or other issues. The number of resulting PSDs relative to the station installation time was then used to assess each station's uptime. Stations exhibiting less than 50% percent uptime and/or failing to record at least one cycle of a seasonally representative one-month or longer time segment were excluded from our noise maps, but were included in the analyses of instrumentation performance. PSDs that were strongly affected by earthquake signals do not require special consideration because they are sufficiently intermittent that they do not significantly affect the median or other central PSD PDF metrics calculated here (e.g., *Aster et al.,* 2008; 2010). For the instrumentation used in this study, the nominal digitizer/seismometer electromechanical noise level is generally substantially below the seismic noise field (e.g., *Peterson*, 1993; *Wilson et al*, 2002; *Ringler and Hutt*, 2010) and thus usually do not affect these metrics (the exception being at extremely quiet sites such as ice boreholes at short period (< 0. 1 s)).

ii. Noise Band Characterization

To evaluate the spatial distribution of the seismic noise state at these stations, we separated the median PSD of each station component into six period bands (Figure 1.2) of interest to source and imaging seismology and examined the median power in each.

The short-period band, 0.15-1.0 s, captures common sources of anthropogenic noise, seismic coupling due to wind (e.g., *Withers et al.*, 1996; *Young et al.*, 1996, *Peterson*, 1993; *Galperin et al.,* 1986; *Li et al.,* 1984), as well as signals ranging from local glaciological movements to teleseismic earthquakes.

The 1.0-5.0 s teleseismic body wave band is shared by intermittently excited local, regional, and teleseismic earthquake-generated body waves, which are key to structural and source-related studies. Additionally, several recent studies have attributed noise in this band at near-coastal and near-lake stations to local or regional swell activity (*Bromirski et al.*, 2005; *Tsai and McNamara*, 2011; *Aleqabi et al*., 2013), which constitutes the shorter-period portion of the double frequency (secondary) microseism.

The 5.0-10.0 s and 10.0-20.0 s secondary and primary microseism bands, respectively, are dominated, in the absence of earthquake or other transient source excitation, by ocean-generated Rayleigh waves. The primary microseism originates when deep-ocean waves break or shoal on a shallow seafloor and are primarily converted into Rayleigh waves (e.g., *Hasselmann,* 1963). The typically much more powerful secondary microseism is usually generated by standing-wave components of the oceanic wavefield (e.g., coastal reflections, storm-storm, or intra-storm wave interactions; *Ardhuin et al*., 2011) that generate sea-floor forcing at half the period of the constituent traveling ocean waves (e.g., *Longuet-Higgins,* 1950*; Tanimoto,* 2007*).* Variations in microseism power at specific stations in Antarctica are known to be strongly sensitive to both near-coastal storms and to wave-state (e.g., *MacAyeal et al.,* 2006) and are amplitude modulated by the annual formation and breakup of sea ice (*Aster et al.,* 2008, 2010; *Grob et al.*, 2011).

The 20-50 s intermediate period band contains power from the longest period microseisms and is strongly excited by intermediate-period surface waves from global earthquakes.

The 50-150 s long period band is controlled by low-amplitude (e.g., ~300 time smaller in power than double frequency microseism excitation) oceanic excitation of long-period waves generated through infragravity wave excitation and difference-frequency interaction of opposing ocean wave trains (*Rhie and Romanowicz*, 2004; *Traer et al*., 2012). A common source of instrumentally generated noise in this band is diurnal or other seismometer tilting that strongly couples into the horizontal components (e.g., *Sorrels,* 1971; *Peterson,* 1993; *Wilson et al.*, 2002). This period band is also intermittently excited by long-period teleseismic surface waves from large earthquakes.

Results and Discussion

i. Polar Instrumentation Performance for Different Siting Methodologies

To evaluate the absolute and relative performance of year-round seismographs in Antarctica under different siting conditions, we cull the PSD dataset of obvious instrumentation artifacts as described previously, and inter-compare median PSD metrics (Figure 1.3). Post-artifact uptimes for different emplacement types were highly variable, with permanent stations (9) recording acceptable quality data 89% ± 3% of the time, POLENET ANET sites (38) at 83% ± 5%, and GAMSEIS/AGAP sites (30) at 66% ± 4%. The lower data retrieval rate of the AGAP sites reflects the extremely cold temperatures and consequent service and technical issues of working on the high elevation East Antarctic Plateau (annual average ambient temperatures of -50 to -60° C and much colder temperatures during the winter). Subdividing the POLENET ANET sites into emplacement type shows an uptime advantage of ice sheet (91% ± 4%) and shallow snow (84 ± 8%) siting scenarios compared to rock outcrops (72% ± 14%).

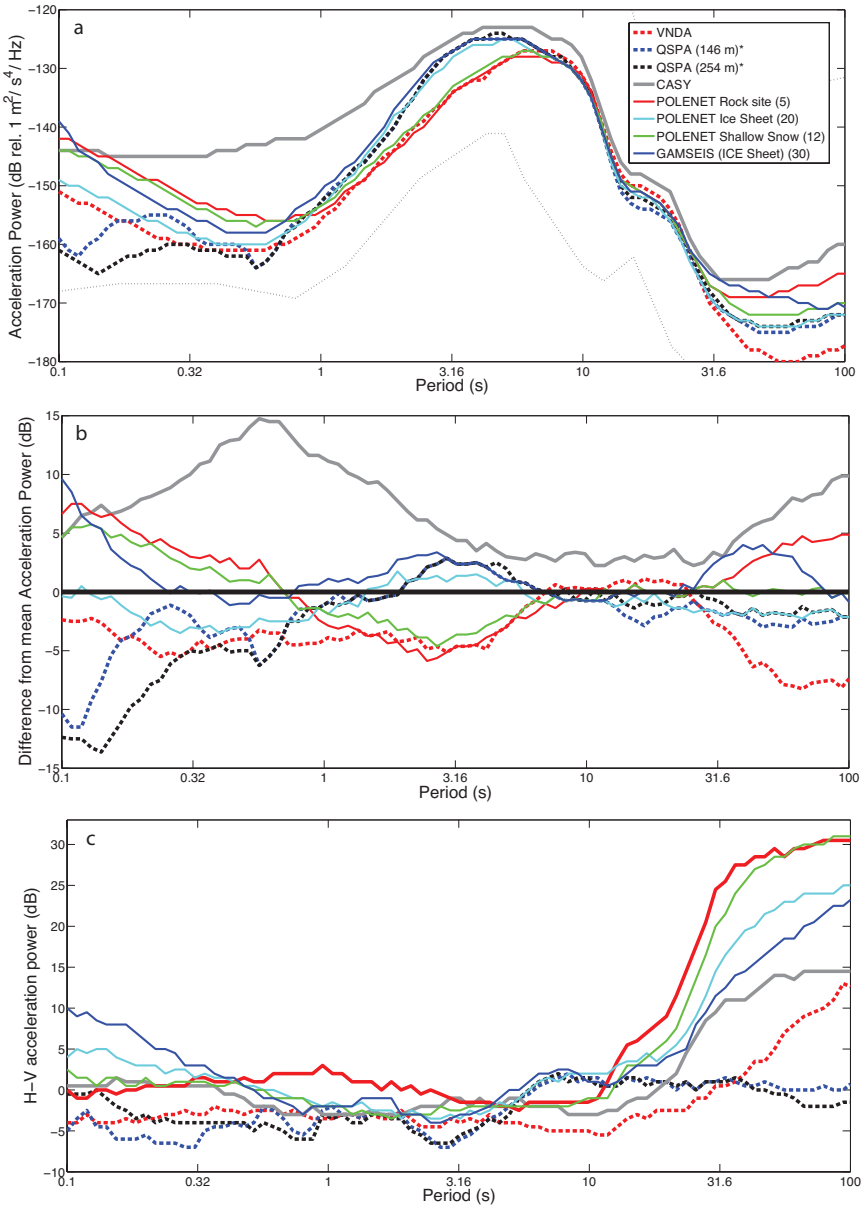

Figure 1.3. (a) Median vertical-component PSDs for different siting types, as defined in the text, between 2008-2012 with the estimated Global Seismic Network low-noise models (light gray dashed line; *Peterson*, 1993). Borehole sensors are indicated by dashed lines, and the numbers in the legend represent the number of stations included in the median estimate or borehole depth. Due to intermittent instrumentation issues**,** we only used data from February 2011 – December 2012 for characterizing the 146 m QSPA borehole and omitted 2012 data for the 254 m borehole. For comparison to a high quality North American site, we also show ANMO, which is a long-running GSN rock borehole located near Albuquerque, NM (USA). **(b)** Removing the mean value of the PSD estimates in (a) displays relative noise level differences. **(c)** Subtracting the median horizontal power (attained from averaging the BHE and BHN PSDs) from vertical power for the different emplacement types shows substantial amplification of horizontal power at several sites, which are primarily attributable to tilt-coupled horizontal noise.

Median vertical-component PSDs for the limited number of available long-term stations and installation types reveal several intriguing differences (Figure 1.3a,b). Unsurprisingly, the two borehole emplacements (VNDA, QSPA) are up to 20 dB quieter at high frequencies compared to surface sites, reflecting the effective mitigation of wind noise (e.g., *Withers et al*., 2006). Rock and shallow snow POLENET ANET sites comprise the noisiest temporary seismic installations in the short-period band, being 5-7 dB noisier than comparable ice sheet sites. This is likely explained as 1) many of these stations are located in the Transantarctic Mountains, which is one of the windiest places on the continent (e.g., *Mayewski et al*., 2009) and 2) these sites are located on/near rock outcrop topography that facilitates the coupling of wind energy into seismic noise. Additionally, stations placed directly on rock outcrops show enhanced horizontal noise, which we interpret as tilt, at periods of 0.5-3 s, as evidenced by a 5 dB difference between horizontal and vertical-component noise (Figure 1.3c). We hypothesize that this is also a result of wind forcing on the exposed outcrop and instrumentation enclosure. It should be noted that even these noisy POLENET ANET sites in the Transantarctic Mountains are characteristically 10-15 dB quieter in the short-period band than permanent base-sited coastal stations at CASY, PMSA, DRV, which are affected by persistent circumpolar westerly winds and probably also all have some significant level of anthropogenic noise for part of the year (Figures 1.3, 1.5). Between 0.3-2 s, these coastal, permanent pier and vault stations are the noisiest population by 3-15 dB and have a distinct peak in noise at ~0.5 s relative to other stations, suggestive of the buildings or other structures around the station being excited by the wind in this period band (Figure A2.1, available in Appendix 2 of the dissertation).

The teleseismic body wave band reveals that the noise levels observed between rock and ice sites diverges between 1.25-7 s period, with ice site median levels being ~9 dB noisier at 3 s (Figure 1.3b). The noise in this band is comprised mainly of Rayleigh waves generated by near-coastal primary and secondary microseism sources. Using experimentally determined seismic velocities in ice sheets beneath the fern-ice transition (V_p = 3.8 km/s; e.g., *Albert,* 1997; *Kohnen*, 1974) compared to a fast (6.2 km/s) upper crust for a bedrock site yields a local amplification of ~2.5 dB. Thus, this phenomenon cannot be entirely attributed to the simple elastic seismic wave amplitude effects of the ice sheet and could be the result of an exceptionally strong contribution from the shallower snow, including that above the firn-ice transition (V_p = ~0.5-3 km/s; *Albert,* 1997) and/or to trapped energy in the ice-sheet-atop-bedrock waveguide near these periods. We additionally note a ~4.5 dB increase in the difference between horizontal and vertical-component noise (Figure 1.3c) throughout this amplified secondary microseism band at ice sites relative to rock sites, which may reflect the influence of a smaller Poisson's ratio (i.e., $\sigma \sim 0.2$) in the upper ice sheet relative to rock sites.

Noise levels are relatively consistent in the primary and secondary microseism bands for all installation types with the exception of the near coastal site CASY. The intermediate period band between 20 and 50 s has ~5dB of elevated noise on the AGAP stations. Closer examination of these stations revealed a newly recognized source of instrument noise that was ultimately linked to the formation of convection cells within the sensor due to sensor heat dissipation under extremely cold ambient temperature conditions (*Anthony et al., 2011;* T. Parker (IRIS PASSCAL), pers. comm.). This phenomenon produces noise at periods of ~30-70 s and only

affects the vertical-components of a few sensors, mostly those located on the East Antarctic Plateau (Figure A2.2), and is generally absent during the warmer summer months.

ii. A Case Study of QSPA (South Pole): Implications for Icecap Borehole Sensors

Borehole installations at tens to hundreds of meters substantially reduce wind noise as well as some types of anthropogenic noise (e.g., *Young et al*., 1996; *McNamara and Buland*, 2004). QSPA is a unique installation that incorporates borehole sensors installed within the nearly 3000 m-thick south polar icecap. It is the only such station in the Global Seismographic Network, which includes a large number of conventional bedrock borehole sites (*Butler*, 2004). The QSPA site is a component of the South Pole Remote Earth Science and Seismological Observatory (SPRESO), sited 7.9 km from the Pole and the Amundsen-Scott (US) South Pole Station within a designated vibrational Quiet Sector for South Pole science operations. The transition from snow to compact ice as a result of pressure with increasing depth results in a laterally uniform seismic velocity gradient within the upper 200 m of the ice sheet (*Gow*, 1963,1975; *Patterson* 1994). Modeling of short-period anthropogenic noise within this velocity model indicates that surface-generated noise is trapped in the near-surface firn layer (*Albert*, 1997). Two of the three QSPA borehole sensors were installed below 200 m to be located beneath this waveguide.

The multiple seismic instruments collocated at QSPA provide an opportunity to compare the noise levels of surface vault seismometers with borehole instruments in a continental interior ice sheet environment. Recording at QSPA began in January of 2003, where three borehole instruments (at 275, 254, and 146 m) were supplemented with additional sensors located in vaults 4 m below the surface. The station received numerous sensor replacements and updates

during its development and testing between 2009-2011 (K. Anderson and T. Storm, pers. Comm.). Here, we analyze data from longer contiguous periods of the archive collected at the surface vault and with borehole Guralp CMG3-T sensors at 146 m after February 2011 and at 254 m between 2007-2011.

Overall, baseline (winter), high frequency (5-10 Hz) noise power is lower by 15-25 dB in the borehole installations on all components. This advantage diminishes with increasing period until ~1 s, beyond which noise levels for the surface and borehole sites are nearly identical (Figure 1.4a). The 254 m deep borehole is several dB quieter than the sensor at a depth of 146 m at frequencies greater than 1 Hz, with the greatest improvement of ~5 dB observed between frequencies of 3-5 Hz. Noise levels during the weekend and during the weekday are similar during austral winter months of highly reduced human activity (February-October), suggesting that the natural background noise state, free from anthropogenic contamination, is approached at the SPRESO site during this part of the year. The vertical-component noise is nearly uniform between the surface and borehole sites at long periods, but the horizontal components of the borehole sensors are 35-40 dB quieter than the surface at 100 s, due to the strongly reduced tilting of these clamped sensor packages relative to shallow ice vaults (Figure 1.3c). This reduction in long-period, horizontal-component noise is 10 dB greater than that noted between rock boreholes and nearby surface vaults in the southwestern United States (*Wilson et al*., 2002).

During the austral summer (November-January), there is a large difference between the weekday noise and the weekend noise levels (up to 26 dB), in the high-frequency band (< 1 s) showing that anthropogenic noise from the South Pole station is readily detected at all depths

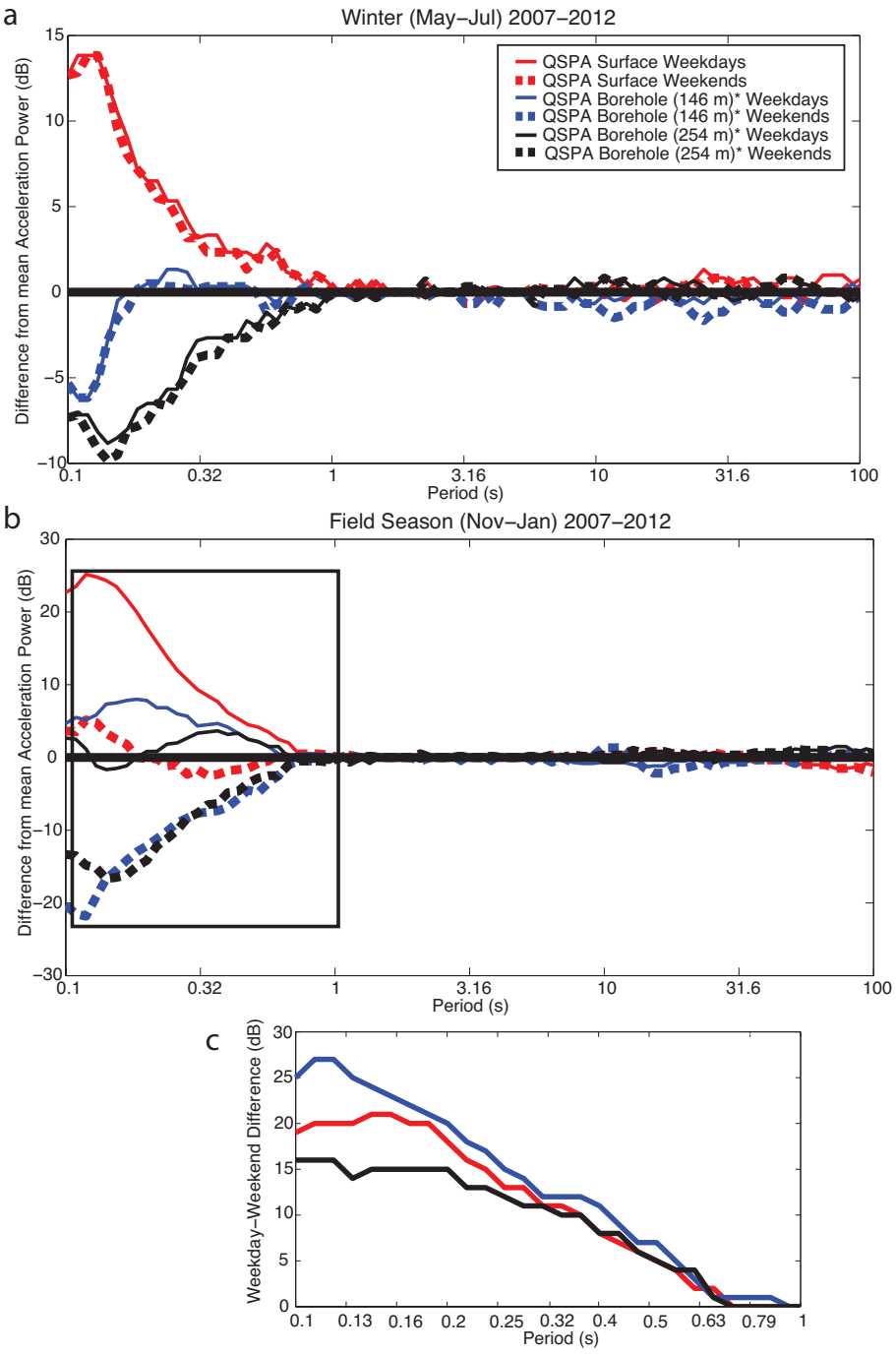

Figure 1.4. Deviations of weekday (solid lines) and weekend (dashed lines) median vertical-component PSDs for the three sensor depths at the SPRESO site, incorporated into station QSPA, between 2007-2012 during **(a)** the winter (May-July) and **(b)** the field season (November-January). **(c)** Weekday/weekend differences for the boxed region in (b) shows the influence of anthropogenic noise from nearby (7.8 km) Amundsen-Scott South Pole station during the field season. The 146 m borehole is the least effective at mitigating this cultural noise likely because it is located within the near-surface (~200 m) firn waveguide that traps high frequency energy (Albert, 1997).

(Figure 1.4b). Subtracting weekend from weekday power levels (Figure 1.4c) we observe that station activities at the South Pole during the busiest season at the base results in a 15-25 dB increase in high frequency (0.1-0.2 s) noise that decays approximately exponentially with increasing period. A likely significant source of this noise is the frequent grooming of the snow runways by heavy equipment (*Anderson et al*., 2008). The 254 m deep borehole sensor, located well below the firn-ice transition (*van den Broeke*, 2008), is seen to be most effective at mitigating anthropogenic noise by up to ~5 dB compared to the surface vault and by up to ~10 dB compared to the 146 m borehole which lies within the (upper ~200 m). These results thus support the *Albert* (1997) model prediction that high-frequency seismic energy from surface sources is substantially trapped in the shallow Antarctic icecap.

iii. The Continent-Scale Seismic Noise Environment of Antarctica

To produce estimates of median vertical-component noise level variations across the continent (recognizing that the spatial sampling is of course still very sparse), power levels in the above-defined period bands at each station were geographically interpolated on an equal-area, UTM-style, mesh grid (Figure 1.5; horizontal component noise level maps show similar trends see Figures A2.3-A2.4). A striking feature on these maps are the anomalously high and broadband (0.15–20 s), (5-20 dB) noise levels of the Antarctic Peninsula relative to the rest of the continent, with the discrepancy becoming stronger at shorter periods. This is likely primarily due to the high winds associated with the circumpolar westerlies and the resulting effects of tempestuous seas in the Drake Passage and Bellingshausen Sea, accentuated by the narrowness of the peninsula and station proximities to the coast.

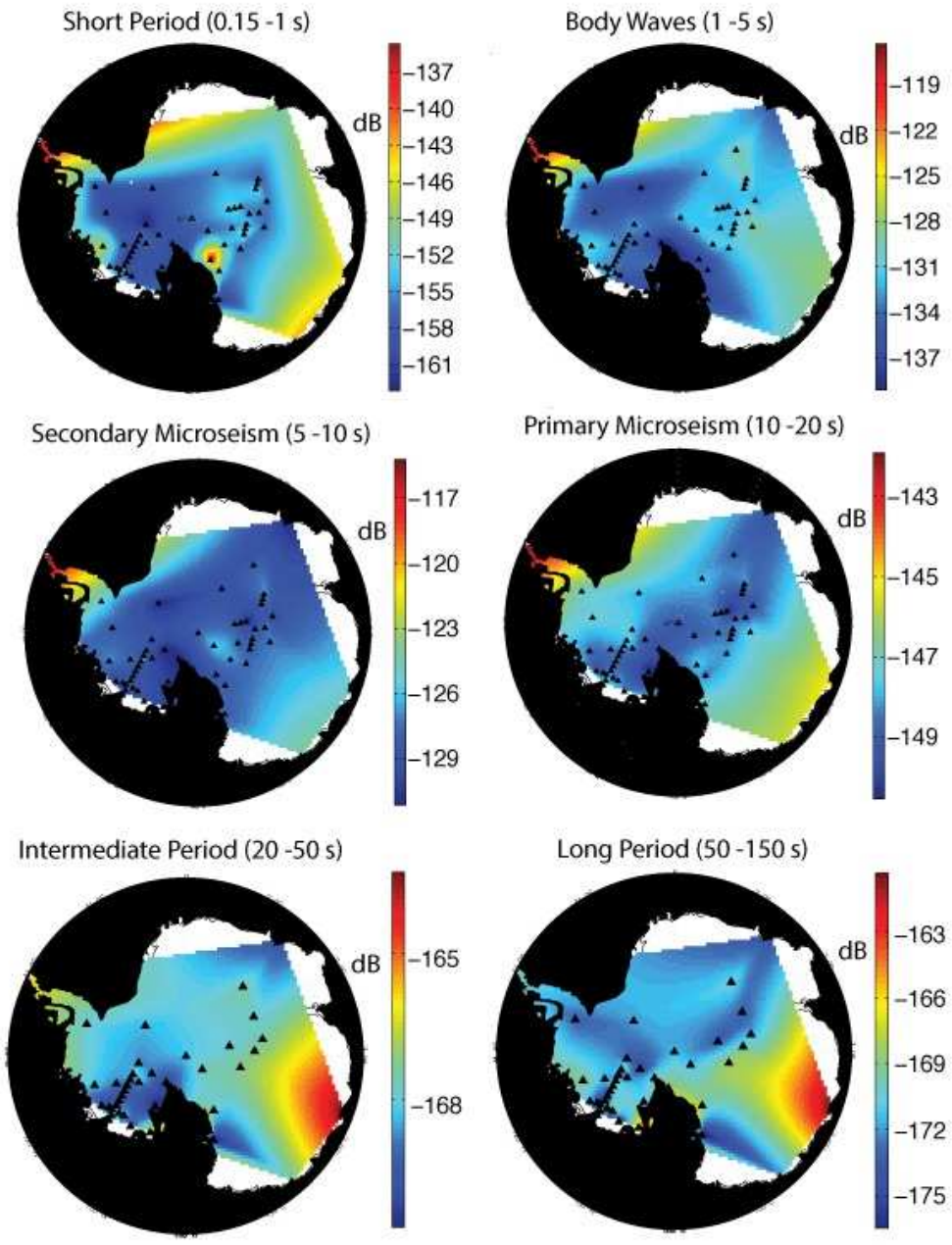

Figure 1.5. Interpolated noise-map of Antarctica for each of six separate period bands (Figure 2) using median vertical-component power in each for 59 seismic stations (QSPA surface station used) located across the continent (triangles). Note that color scale changes with each period range to illustrate contrast and represents acceleration power in dB. MILR is the red dot in the Transantarctic Mountains in the short-period map and reflects the exceptional wind coupling at this unstable rock site. Long period sensor tilt at MILR is severe and the station has been omitted from the intermediate and long period maps. Stations afflicted with the long-period convection noise (HOWD, several GAMSEIS/AGAP sites) were also omitted from these two frequency bands. Note that the large red feature in East Antarctica is controlled by one very noisy coastal station (CASY; Figure 1.3).

Noise in the short-period band is also relatively high (~10 dB above the majority of the continental interior) at non-Peninsular coastal and central Transantarctic Mountain sites. This is consistent with estimates of higher wind speeds in these areas from long-term (e.g., 40-year) weather reanalysis, for the central TAM and East Antarctic Coast (*Mayewski et al*., 2009). Away from the Antarctic Peninsula and its exceptionally strong and broadband oceanic microseism noise, PSD median levels in the teleseismic body wave band (1-5 s) become much more uniform**,** varying by just ~7 dB**,** with the highest levels recorded at near-coastal stations and for sensors sited atop thick ice sheets (e.g., GAMSEIS/AGAP; POLENET ANET Transect Stations; WAIS).

Generally, power in the primary and secondary microseism bands are highest at near-coastal stations and decay into the continental interior by up to 6 dB and 12 dB, respectively. The gradient of decay is period-correlated and is most readily observable around the Antarctic Peninsula. Compared to most of the planet, noise levels in the entire microseism band (1 – 20 s) in Antarctic are strongly affected by the annual growth and decay of sea ice around the continent (Figure 1.6; primary microseism shown for reference). In both microseism bands, seasonal power varies by at least 10 dB, with annual maxima occurring across most of the continent during the sea ice minimum, which occurs approximately three months prior to peak oceanic storm activity in the southern hemisphere (*Aster et al.,* 2008). Minimum noise in the microseism bands occurs during the summer across the continent, with the notable exception of primary microseism power at DRV. We suspect that high levels of local sea-ice loss early in the melt season may drive this phenomenon by exposing the Wilkes Land regional coastline and shelf to Southern Ocean waves earlier in the year. Previous analysis of microseism noise at DRV has

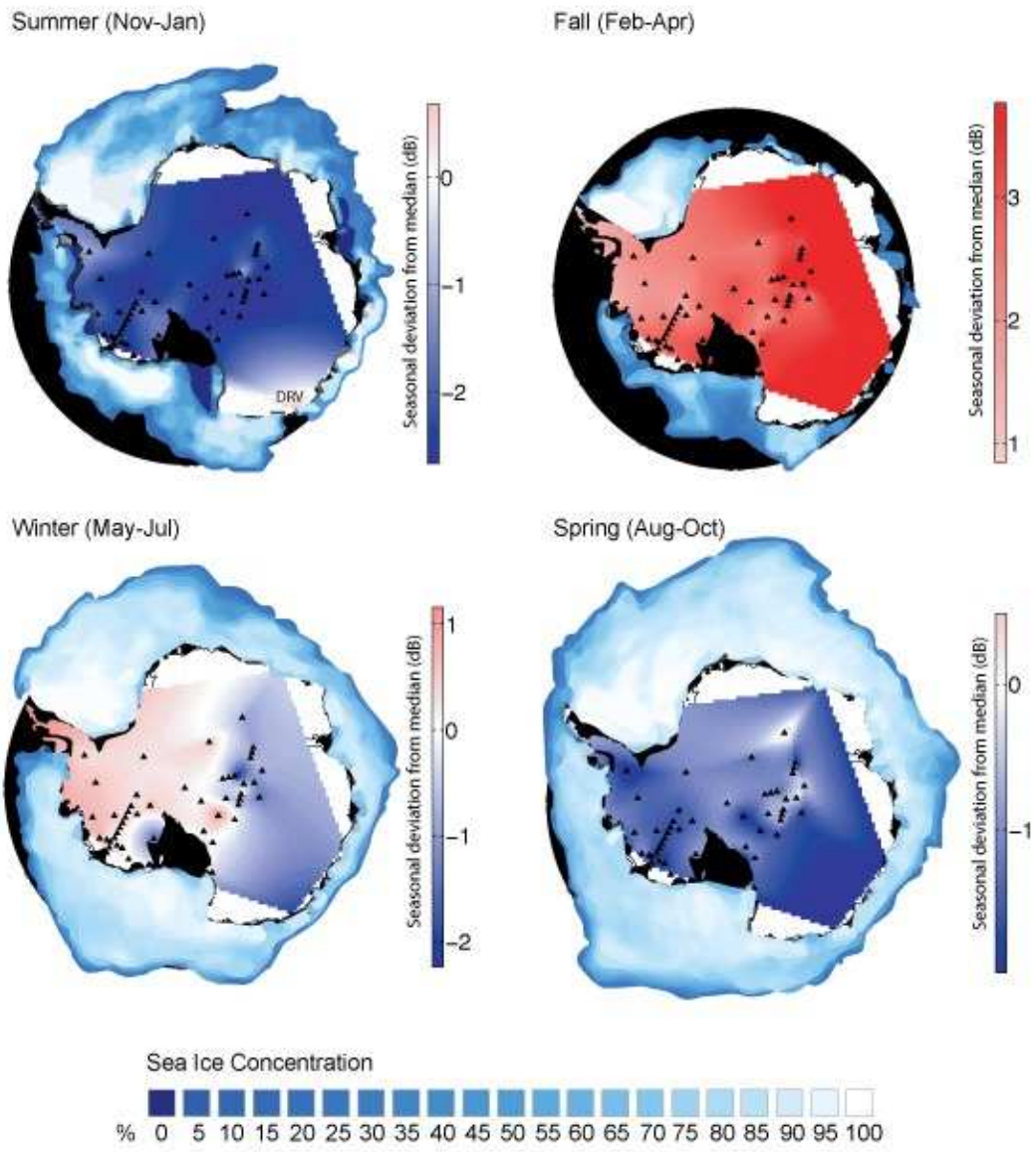

Figure 1.6. Interpolated map of seasonal median differences from year-round medians in the primary microseism band (10-20 s) overlain on representative sea ice concentration maps from the middle month of each season during 2009 (*Fetterer et al*., 2002). Red indicates station-interpolated regions that are noisier for a particular season than the median, and blue indicates regions that are quieter. Seasonal power variations in this band are strongly influenced by the annual build-up and decay of sea ice, with the entire continent experiencing highest noise levels during the fall sea ice minimum. Nearly all of West Antarctica experiences above-average noise levels during the winter, likely in response to Southern Ocean swell interacting with the ice-free northern Antarctic Peninsula (Koch et al., 2013). The Wilkes Land coastal region near Dumont d'Urville (DRV) is one of the earliest sections of Antarctic coastline to be directly exposed to Southern Ocean swell during early summer, and consequently is the only area of the continent in this study to show above average primary microseism power during this season.

shown that the primary microseism source backazimuth shifts seasonally towards the closest ice-free ocean (*Stutzmann et al.*, 2009).

Comparing the noise environment of the Antarctic continent to long-running sites in interior North America allows for a simple comparison between these Antarctic noise levels and typical data recorded in the northern hemisphere (e.g, by EarthScope USArray). We compared the median PSD metrics calculated in this study (Figure 1.3) to a 145 m rock borehole sensor at GSN station ANMO (Albuquerque, New Mexico, USA). In general, Antarctic stations are ~5 dB quieter at short-periods (< 1 s) than ANMO, likely because of limited anthropogenic noise contributions, greatly reduced wind profiles, and potentially poorly characterized short-period response at the 145 m ANMO borehole (Adam Ringler (USGS Albuquerque Seismic Laboratory), pers. Comm.). However, even without considering the ice-sheet amplification effect widely observed between ~1.25-7 s, West Antarctica is typically 2-5 dB noisier than ANMO in the microseism bands (1-20 s) despite being seasonally surrounded by a sea ice buffer. This likely reflects the more extreme wave states and storm activity present in the Southern Ocean relative to the Northern Pacific Ocean, which dominates the microseism band at ANMO (e.g., *Aster et al.,* 2008).

Conclusions

Broadband seismic background noise for Antarctica is characterized using recently collected year-round data that have greatly expanded coverage across the continent. We analyzed noise levels within six discrete bands that encompass diverse sources of natural, anthropogenic, and instrument (e.g., tilt-coupled) noise, and have broadly characterized the large-scale geographic

distribution of power in each band across the continent and nominal noise level expectations for future Antarctic stations. We conclude the following regarding the various types of installations presently available for analysis:

Ice Borehole Stations. Despite detectable short-period-dominated anthropogenic noise during the busiest part of the year from the 7.8 km-distant Amundsen-Scott South Pole Station, the borehole seismometers at QSPA are the quietest sensors in Antarctica at high frequencies (> ~2 Hz), occasionally dropping below the *Peterson* (1993) Low Noise Model, and are thus candidates for the quietest stations on earth in this frequency range. Our observations confirm that placing the sensor below the near-surface waveguide modeled by *Albert* (1997) (> ~200 m) results in an ~5 dB reduction in baseline natural high-frequency noise and a 10 dB reduction in anthropogenic noise compared to a sensor located within the waveguide. Additionally, the QSPA borehole instruments are the only ice-sited sensors in Antarctica to exhibit extremely low tilt-coupled horizontal component noise at long periods (i.e. > 50 s) and attendant low general long-period noise levels. QSPA does experience an up to ~9 dB amplification in background noise at 2-5 s similar to that observed on all thick ice sites, and that we conclude is a combination lowered seismic impedance and ice-atop-bedrock waveguide effect.

Rock Borehole Stations. The 100 m rock borehole VNDA, located in the dry valleys, does not exhibit the amplified 2-5 s noise levels of QSPA and other ice sheet sites, and is also ~5 dB quieter than the QSPA boreholes and POLENET ANET ice vaults at 50-100 s, making it the quietest long-period instrument in Antarctica. The instrument does appear to exhibit some tilt-coupled noise at >30 s period, as is visible in vertical/horizontal power ratios, but this

discrepancy between components is smaller than for any other sensor on the continent except the QSPA ice borehole sensors. Short-period (< 1 s) noise levels at VNDA are better than any other Antarctic station, except for the QSPA boreholes, despite its location in the windy Dry Valleys and at the foot of the Transantarctic Mountains. This station is generally ~10 dB quieter than comparable POLENET ANET rock sites; however, 8-30 s microseism power levels are 1-2 dB higher than typical stations in Antarctica, which we attribute to relative proximity to coastal microseism sources.

Together, the two borehole stations are the quietest sites in Antarctica between 0.15-100 s and are exceptionally impervious to wind and tilt-coupled horizontal noise. Because of their low long-period noise, establishing additional boreholes sites in Antarctica would significantly improve the ability to detect and study long period signal generated by the cryospheric and tectonic processes in Antarctica. For instance, these two sites were the only stations capable of clearly detecting the 25-83 s slip signal generated by slow cryospheric events from the Whillans Ice Stream in West Antarctica by *Wiens et al*. (2008).

Ice Sheet Stations. In general, POLENET ANET vaults, where sensors were typically deployed 1 – 2 m below the surface and atop thick ice sheets, were 5-7 dB quieter in the short-period band than comparable rock and near-rock/shallow snow vaults. These lower noise levels are partially attributable to the stations being deployed in less windy areas with flatter topography and accordingly lower levels of seismic wind coupling. In addition, many of these sites become covered drift, resulting in very low wind profiles. These sites are also 5-7 dB quieter at 30-100 s than rock/shallow snow vaults, reaching vertical noise levels that can approach the 254 m QSPA borehole in this band. GAMSEIS/AGAP ice vaults deployed on the East Antarctic Plateau

experienced greater difficulty operating continuously in the exceptionally harsh East Antarctic environment. Some of these stations experienced strong, ~30-70 s, internal convection noise on the vertical-components, a newly recognized process of internal seismometer noise generation that is now understood and being ameliorated (T. Parker, pers. Comm.).

Rock and Shallow Snow Stations. Rock and shallow snow stations are here classified as those sited on top of and adjacent to isolated Nunataks and/or in close vicinity to Transantarctic Mountain outcrops. In these locations, we found that emplacement in even shallow snow/ice was broadly superior to direct rock installation, particularly in improving long-period (> 10 s) sensor horizontal noise attributed to tilt, and in the near-elimination of shorter-period tilt, which we suspect arises from direct wind forcing on the outcrop and station. At an especially noisy rock vault from POLENET ANET (MILR, Figure 1.5), these wind-driven effects were so severe that the microseism peaks were sometimes obscured on PSD PDFs of the horizontal components and the station was rendered unusable for shear wave splitting studies (*Accardo et al.*, 2014). Additionally, we note that station uptimes for rock vaults (72%) are not as good as shallow-snow or ice vaults (84%, vs. 91%), primarily because these sites are more susceptible to damage from extreme storm events. In the future we recommend installing stations that are near outcrops on adjacent snow rather than rock when possible.

Long-term Stations with Bedrock Piers/Vaults. The longest-operational seismographic stations in Antarctica, aside from the heterogeneous installations over the years at South Pole, are collocated with coastal research stations and are consequently subject to anthropogenic, wind, and microseism noise. Between 0.3-2 s, these stations as a group are the noisiest in Antarctica.

Compared to remote, temporary shallow snow vaults, the main seismic noise advantage of these installations, which incorporate larger-scale permanent piers, is convenience and reduced sensor tilt (i.e., an ~10 dB smaller discrepancy in H/V ratios at 100s).

Using the long running GSN borehole station ANMO as an example of a long-running high quality station for reference, we find that many interior stations in Antarctica are quieter than ANMO at short-periods (< 1 s), but that they also show more energy in the microseism bands (1-20 s) due to the content being surrounded by the Southern Ocean, and despite lower noise levels arising from annual sea ice growth. Aside from the aforementioned ice-sheet-associated amplification between ~1.25-7 s, noise levels in Antarctica in the microseism-spanning bands are controlled by proximity to strong microseism source generation regions (especially the Antarctic Peninsula), and to seasonal and longer-term changes in southern ocean wave state and sea ice extent. Geographic variations in microseism power become less pronounced, but are still resolvable, at longer periods. Maximum power in these period bands generally occurs across the continent during the Austral fall, when annual ocean wave activity is increasing and sea ice coverage is at a minimum. The formation of the sea ice buffer during the winter slightly reduces yearly variations of microseism power in Antarctica (~10-15 dB) compared to non-polar stations (e.g., 12-18 dB at ANMO).

Recent year-round seismic deployments in the remote interior of Antarctica have dramatically increased the quality and quantity of broadband data from large hitherto unsampled areas of the continent. These data are helping to drive significant new understanding about solid Earth, and glacial structures and processes (e.g*., Chaput et al.*, 2014; *Lough et al.,* 2014; *Accardo et al.*,

2014; *Peng et al.,* 2014). Uptimes of temporary ice-sheet vaults utilized in the POLENET ANET deployment rival those of many long-term stations collocated with research bases, yet show substantially reduced noise levels in the period bands of local and teleseismic earthquakes and ice quakes. These results indicate that the seismological community is now capable of both interrogating additional sections of polar and other cold regions and able to move towards the establishment of more geographically extensive and long-term Antarctic and Arctic seismographic networks.

Chapter 2: Links Between Atmosphere, Ocean, and Cryosphere from two Decades of Microseism Observations on the Antarctic Peninsula[2]

Introduction

The Antarctic Peninsula (AP) has undergone profound environmental change during the second half of the twentieth century, including local trends of atmospheric warming exceeding 0.5° C per decade (*Vaughan et al*., 2003; *Turner et al*., 2005), a marked decrease in sea ice extent in the Amundsen-Bellingshausen sector (-6.63% per decade; *Turner et al*., 2009), and the disintegration of four ice shelves and significant retreat of others, yielding a loss of over 28,000 km^2 of floating ice (*Cook and Vaughn*, 2010). The loss of this floating ice has led to significant and decadal-scale dynamical thinning and acceleration of glaciers that previously fed these shelves (*Scambos et al*., 2004; *Pritchard et al*., 2009). Similarly, more than 80% of the nearly 400 steep mountain glaciers flowing west off the spine of the peninsula have accelerated and retreated substantially, likely driven by changes at the tidewater terminus (*Pritchard and Vaughn*, 2007). The spatiotemporal complexity of both the observed changes (i.e., greatest atmospheric warming during winter on the western AP and in summer/autumn on the eastern AP; *Turner et al*., 2013), along with atmospheric and oceanic circulation around the AP, precludes singular attribution of a forcing mechanism.

Modified circulation patterns, largely driven by increases in latitudinal pressure gradients, such as measured by the Southern Annular Mode (SAM) index, likely played an important role including raising surface temperatures on the AP (e.g., *Thompson and Solomon*, 2002),

[2] Manuscript in Review – Journal of Geophysical Research: Earth Surface

strengthening surface winds (e.g., *Hande et al*., 2012), reducing sea ice concentration around the AP (*Lefebvre et al*., 2004), and increasing wave activity in the Drake Passage (*Izaguirre et al*., 2011). The shifting of the SAM to a more positive phase, especially in the Austral summer, has also been linked to ozone loss over Antarctica (e.g., *Thompson and Solomon*, 2002; *Yang et al*., 2007). Compounding these surface changes associated with more positive phases of SAM, it has been recently suggested that larger wave events may be capable of mechanically damaging sea ice and creating a positive feedback loop for sea ice weakening as progressively greater fetches are capable of generating more intense wave activity (e.g., *Asplin et al*., 2012; *Thomson and Rogers*, 2014). However, few direct observations of wave attenuation in sea ice exist and properties such as the mechanical strength of sea ice are difficult to assess, especially over large areas. Furthermore, in situ measurements of historical wave activity and storm events in the Southern Ocean are sparse, making it difficult to characterize current and future impacts of extreme weather events and climate change. The intensity of seismic signals generated from ocean wave activity and recorded by long-running continuously recording seismographs at high latitude sites may be appropriate as a spatially integrated proxy for wave state, storm activity, and sea ice concentrations in the Southern Hemisphere and could usefully compliment satellite, hindcast, and buoy observations.

In the absence of earthquakes or other large transient sources of energy, Earth's seismic wavefield is dominated between ~5-25 s period by microseisms that arise when oceanic swell energy is converted to ground displacement within the solid Earth (e.g., *Haubrich and McCamy,* 1969). At land-based seismic stations, microseism energy appears to be predominantly generated in nearshore locations when swell from storm systems interacts with the continental shelf (e.g.,

Bromirski and Duennebier, 2002; *Bromirski et al*., 2013; *Ying et al*., 2014). A power peak centered near 16 s, called the primary microseism, originates when deep-ocean waves break or shoal on a shallow seafloor and are converted into Rayleigh waves (*Hasselmann*, 1963). A second, stronger source of predominantly Rayleigh waves, the secondary microseism, is commonly generated by oceanic waves reflecting off the coastline and interacting with incoming waves to form standing pressure fluctuations in the water column that oscillate and couple with the seafloor at half the period of the oceanic waves (e.g., *Longuet-Higgins*, 1950; *Tanimoto*, 2007). However, this signal can be generated whenever ocean swell of similar frequencies have opposing components of motion, such as when waves generated by distinct storm systems interact (e.g., *Ardhuin et al*., 2011). Finally, recent work has begun to define a short-period microseism band below 5 s period that has been attributed to local sea state and wave activity generated by regional winds (e.g., *Stephen et al*., 2003; *Bromirski et al.*, 2005; *Chen et al*., 2011).

Peak power in the microseism bands at mid-to-high latitude seismic stations typically coincides with enhanced synoptic scale extratropical storm activity during the winter (*Aster et al*., 2008; *Stutzmann et al*., 2009), resulting in strong annular periodicity. However, due to the winter growth of sea ice around Antarctica, oceanic waves are impeded from efficiently exciting seismic energy, and the annual microseism peak occurs during minimum sea ice extent in the Austral fall, a few months prior to the midwinter storm peak for the Southern Ocean (*Grob et al.*, 2011; *Anthony et al*., 2015). Records of microseism activity on the AP are thus sensitive to concentration and extent of AP sea ice in addition to wave state and storm activity within the Drake Passage.

Recent studies have utilized microseism analysis as proxies for climate indicators such as ocean wave state and changes in intensity and distribution of storm activity (e.g., *Bromirski et al*., 1999; *Aster et al*., 2008, 2010; *Stutzmann et al*., 2009). Additionally, microseism records in the polar regions have been suggested for use in extending sea ice observations beyond the satellite era (*Grob et al.*, 2011) and for estimating the mechanical strength of near shore sea ice (*Tsai and McNamara*., 2011). However, little has been done to characterize how the spatial distribution of sea ice impacts different microseism bands in detail, or to assess the impacts that quasi-periodic modes of atmospheric variability (e.g., El Niño-Southern Oscillation, North Atlantic Oscillation, SAM) have on the microseism record or storm activity in the Southern Ocean. Here, we utilize over two-decades of microseism, sea ice, and SAM observations around the AP to develop a correlation-based approach to estimate the seasonal locations of sea ice impacting observed microseism power, infer microseism source generation regions, and investigate the influence of the SAM on extremal storm activity in the Drake Passage.

Methods

i. Data

The seismograph at the U.S. Antarctic Program Palmer Station, (PMSA; Figure 2.1) has been operated by the Global Seismographic Network (GSN; *Butler et al.*, 2004) since early March 1993, making it one of the longest continuously operating seismic stations in Antarctica. PMSA also has few instrumentation or data gap issues across its lifetime (98.6% uptime), with the longest data gap being approximately 2 weeks. We use vertical component, 1 Hz sampling rate data (LHZ) from the Streckeisen STS-1 sensor located on a bedrock pier sited within a local corrugated steel building (IRIS FDSN Station Book, 1994). This study thus analyzes seismic

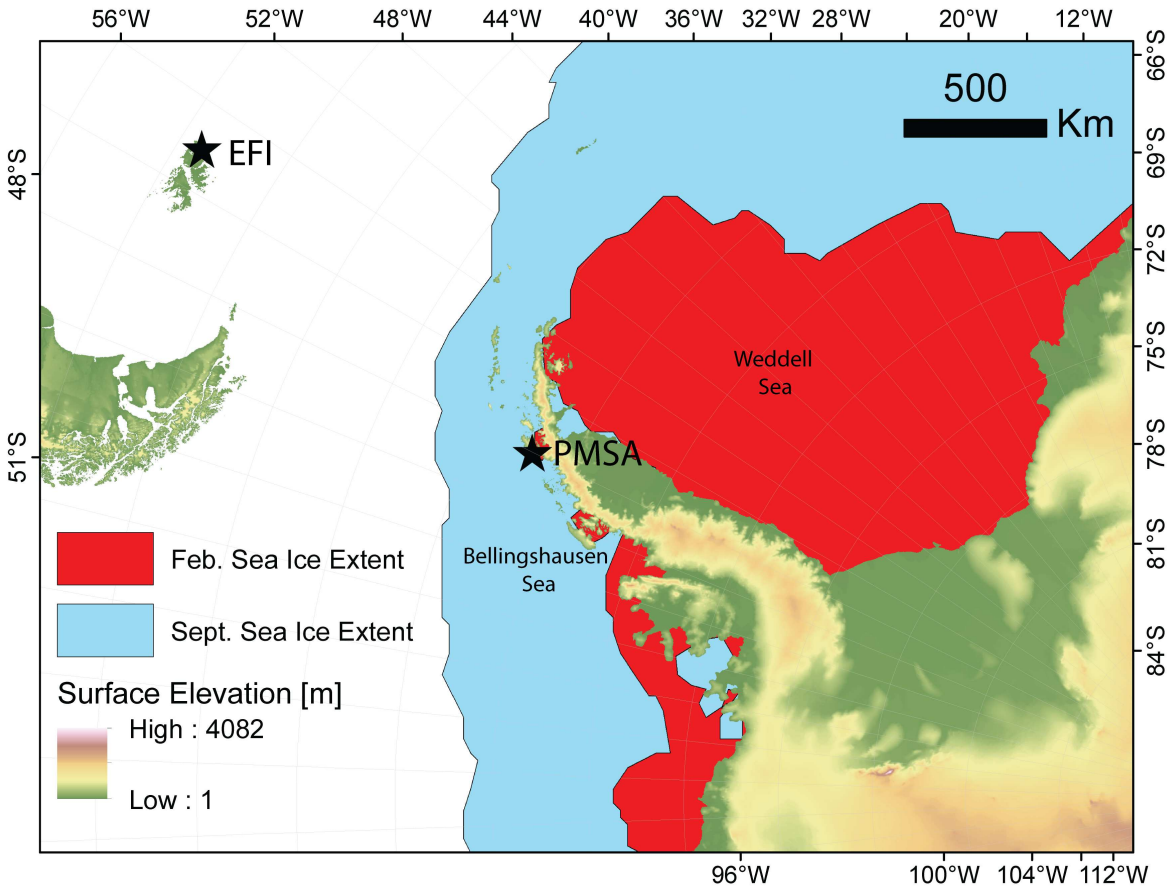

Figure 2.1. The Drake Passage is noted for strong wave activity as the circumpolar westerly winds direct storms between the Antarctic Peninsula (AP) and South America. Sea ice seasonally builds out from the AP, with a maximum extent (mean 1993-2014 values with a threshold of 15% plotted) usually occurring in September (Blue) and minimum extent occurring in February (Red). We analyze over 20 years of seismic data from Palmer Station (PMSA) on the western coast of the AP and East Falkland Island (EFI).

noise at periods longer than ~3 s; local wind-generated seismic noise, which has been noted as being particularly strong at PMSA, is well above the Nyquist frequency of this channel and thus does not affect microseism metrics used in this study (e.g., *Withers et al*., 1998; *Anthony et al*., 2015).

PMSA's location within a hundred meters of the western coastline of the tempestuous Southern Ocean, home to the largest spatial averaged waves on Earth (*Young*, 1999), and comparatively low year-round concentrations of sea ice in the Bellingshausen Sea (Figure 2.1) contribute to near-station generation of the strongest microseism signals in Antarctica, with power levels at PMSA commonly 4-15 times greater than for stations within the continental interior (*Anthony et al*., 2015). During the Austral winter, primary microseism power generated on ice-free portions of the AP coastline dominate the 10-25 s period band for the entire continent (*Koch et al*., 2011; *Anthony et al*., 2015). The combination of exceptionally intense microseism signals recorded at PMSA and highly variable sea ice conditions in the Bellingshausen Sea foster investigations of wave-sea ice interactions and sea state in the Drake Passage region (e.g., *Parkinson and Cavalieri*, 2012; Figure 2.1,2.2).

To complement microseism metrics from PMSA, we identically analyzed data from the GSN station on East Falkland Island (EFI). These data were useful to constrain regional wave activity variations in the Drake Passage without the complicating influence of local sea ice (Figure 1). We processed LHZ data from the Geotech KS-54000 80-meter deep borehole seismometer, which has been recording since February 1996. As the vertical-component microseism signals

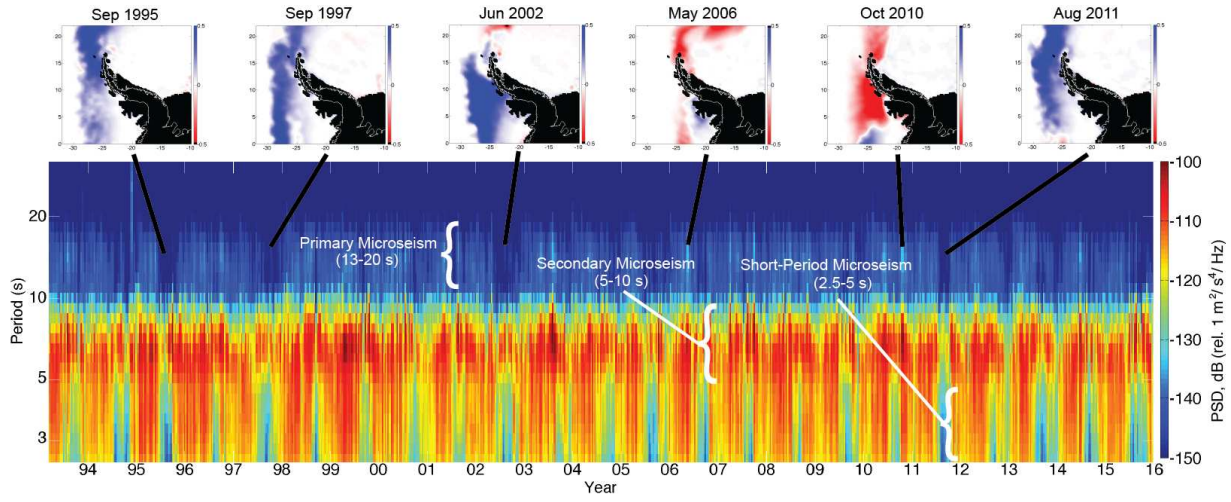

Figure 2.2. Spectrogram of 10-day median, vertical-component acceleration power at PMSA from 1993-2015 with approximate period ranges for the primary, secondary, and short-period microseism bands indicated. Top panels show sea ice anomalies for illustrative months expressed in percent deviation (maximum on colorbar is 50%) from mean monthly sea ice concentration. Primary microseism power is observed to drop strongly during winter months when sea ice concentrations on the west side of the Antarctic Peninsula become anomalously high (blue). The particularly strong primary microseism events highlighted occur during May 2006 and October 2010, and coincide with unusually low concentrations of sea ice.

we focus on in this study are within the intermediate period band (3-20 s), where power level is generally unaffected by sensor depth (e.g., *Wilson et al*., 2002; *Anthony et al*., 2015), the different seismic installation types at PMSA and EFI should have no significant impact on the recorded amplitudes of these signals.

All seismic data was retrieved from the open archives of Incorporated Research Institutions for Seismology (IRIS) Data Services. The continuous time series data were directly converted to 3-hour window acceleration power spectral density (PSD; in dB relative to 1 $m^2/s^4/Hz$) estimates with 50% temporal overlap using the IRIS Noise ToolKit (NTK), resulting in a total of 16 PSD estimates per day. Similar to the widely applied PQLX algorithm (e.g., *Mcnamara and Buland*, 2004; *Mcnamara and Boaz*, 2011), NTK returns power estimates in 1/8-octave period bins and 1 dB power intervals (*Bahavar et al*., 2013). For plotting and correlation purposes, we apply various averaging techniques to the large (>100,000 PSDs at both PMSA and EFI) database of 3-hour PSD estimates (e.g., 10-day median PSD; Figure 2.2).

Daily sea ice concentration data for the Southern Hemisphere from 1993—2014 were retrieved from the National Snow and Ice Data Center (NSIDC) as estimated from satellite microwave back-scatter data (*Cavalieri et al*., 1996; *Fetterer et al*., 2002). Concentration values are averages for 25 km^2 grid cells and have concentration values ranging from 0-1, with 1 indicating that the entire grid cell is covered in sea ice. Monthly means of the Antarctic Oscillation (i.e. SAM) Index were obtained from National Weather Service Climate Prediction Center and are obtained by projecting the 700 hPa anomalies south of 20°S onto the mean loading pattern of the AAO

from 1979-2000

(http://www.cpc.ncep.noaa.gov/products/precip/cwlink/daily_ao_index/aao/aao_index.html).

ii. Microseism Intensity

We subdivided the broad microseism spectrum into distinct primary (13-20 s), secondary (5-10 s), and short-period (2.5-5 s) bands (Figure 2). The microseism intensity (*Aster et al*., 2008) was then estimated from the integration of respective PSD bands as calculated using the IRIS NTK and fit using a 6-term Fourier reconstruction (Figure 2.3,2.4).

iii. Spatio-temporal Correlation Analysis of Microseism Intensity and Sea Ice

To investigate the spatiotemporal influence of sea ice concentration on microseism power for a single seismic station, we utilized the remarkably long and complete time series of both microseism power and sea ice around the AP to perform correlation analysis. First, we converted each 3-hour PSD estimate into normalized (by the maximum) primary and secondary microseism power by integrating across relevant period bins (e.g., Figure 2.3,2.4). We then calculated median microseism power for every month and constructed vectors of median microseism power for each of the 12 calendar months over the entire 1993-2014 time-series.

Similarly, for the daily sea ice grids, we calculated a monthly, mean sea ice concentration for each 25 km^2 grid point for each of the 12 calendar months. This returned 12 grids of vectors, with each grid representing yearly mean sea ice concentrations for one of the calendar months (e.g., 23 years of Junes). We then correlated these yearly mean sea ice concentrations at each grid point against yearly median microseism power for a given month to generate a correlation

grid between sea ice concentration and microseism power for each calendar month (Figures 2.5,2.6). A nearly identical procedure was then performed to develop the correlations between sea ice concentration and SAM phase.

iv. Extremal Storm Analysis

We applied the index hour methodology of *Aster et al.* (2010) to identify extreme wave events in the Drake Passage. The methodology searched for times in the primary and secondary microseism record where the 95th percentile statistic for integrated microseism power was exceeded for three or more consecutive 1.5-hour PSD estimates (6 hours total). We then divided total storm hours for both PMSA and EFI into normalized, 30-day months to attain the statistical distribution of large storm systems in the Drake Passage (Figure 2.7a).

Results

i. Microseism Intensity

Of the three microseism period bands, the short-period is the most annually periodic as well as having the highest dynamic range, with power levels plunging 20-30 dB every winter when sea ice in the Bellingshausen Sea builds out across the entire western AP coastline (Figure 2.2). Previous work using multiple stations with a sampling frequency of at least 20 Hz on the AP has shown that power in this band is exceptionally sensitive to local (< 200 km range) sea ice concentration and strong wind events (*Anthony et al*., 2014). Here, we focus on characterizing synoptic scale storm activity in the Drake Passage and do not analyze short-period microseism power trends further.

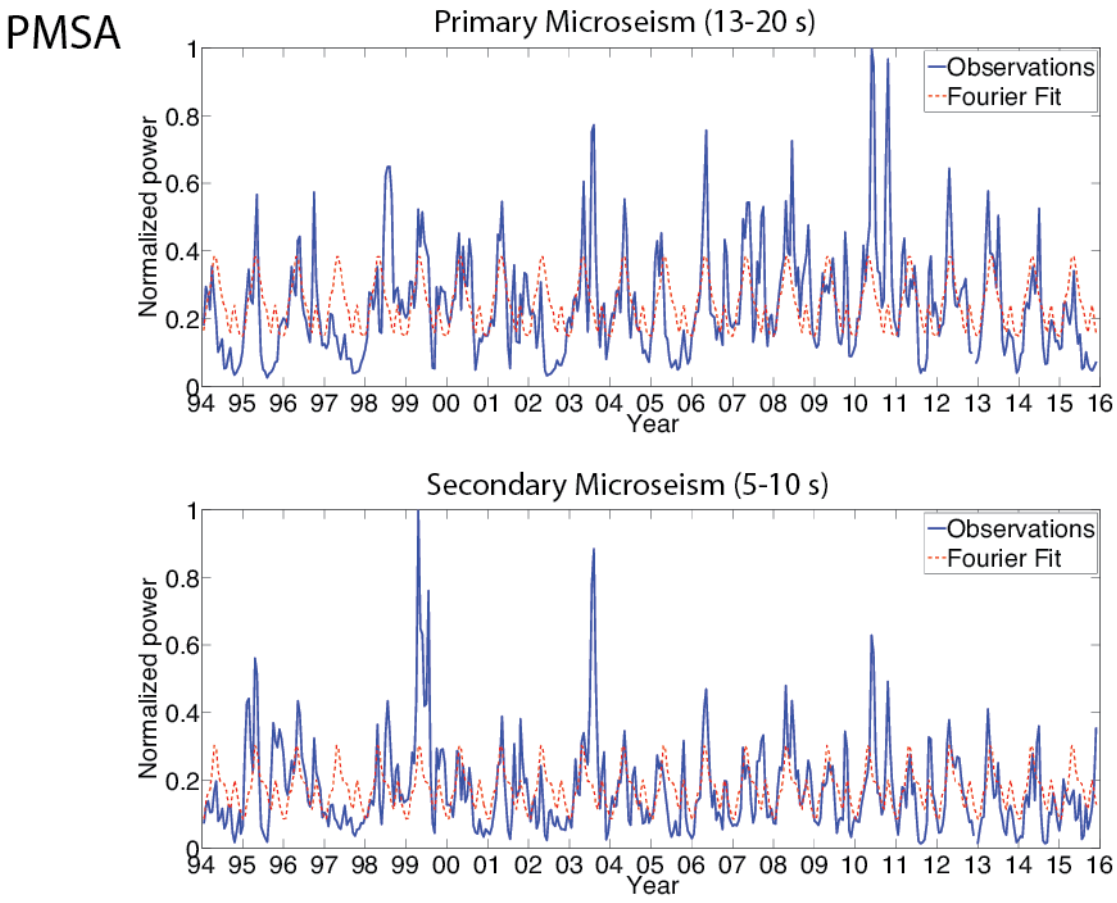

Figure 2.3. Maximum-normalized 50% overlapping deci-year (36.525-day) median, vertical component ground acceleration primary and secondary microseism power (obtained by integrating PSDs) at PMSA through the end of 2015 (blue curves). Red curves show a six-term Fourier fit to the data. The presence of two peaks per year indicate influence of sea ice on the microseism record.

EFI

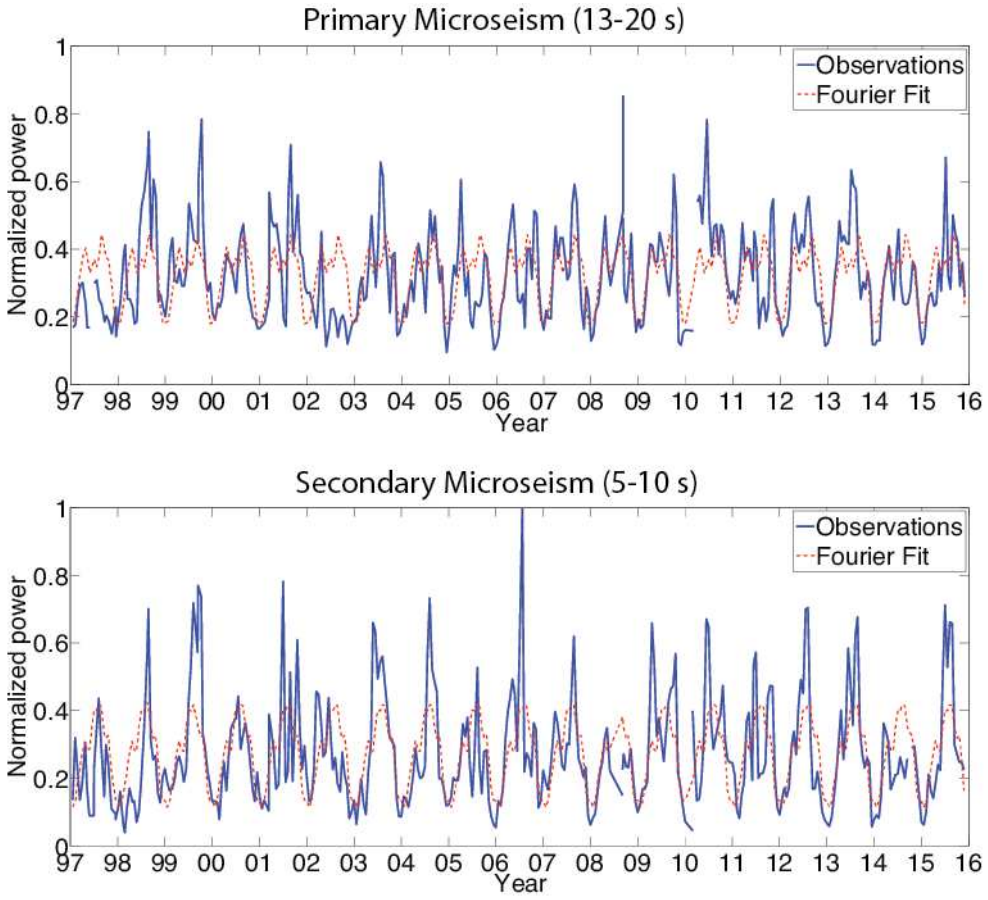

Figure 2.4. Same as Figure 2.3, but using microseism records recorded at EFI. Note that the Fourier reconstruction for the primary, but not the secondary shows a bi-annual peak.

The secondary microseism at PMSA shows the least degree of annual periodicity, in that only 70% of the signal power can be fit with six-term Fourier series. Peak power levels occur biannually, in early May and mid-October (Figure 2.3). In contrast, EFI, which is well beyond the maximal extent of AP sea ice, is far more periodic (84% of its power can be fit with six Fourier terms) and shows a single annual power peak in early September (Figure 2.4). The secondary microseism at PMSA typically varies by ~10 dB and is often observed even during anomalously high sea ice concentrations around the AP (Figure 2.2).

Similar to the secondary microseism, primary microseism power at PMSA also peaks in both early May and mid-October, shows ~10 dB of annual variation, and is not strongly periodic (76% of signal fit by 6-term Fourier analysis, Figure 2.3). However, unlike the secondary microseism, anomalously high levels of sea ice in the Bellinghausen Sea during the winter reduce primary microseism power for several months (Figure 2.2). Interestingly, primary microseism power recorded at EFI also shows an annual bi-modal distribution with peaks occurring in both early May and early September (Figure 2.4).

ii. Spatiotemporal Correlation Analysis of Microseism Intensity and Sea Ice

PMSA microseism intensity-sea ice correlation maps (Figure 2.5) show that both primary and secondary microseism power are anticorrelated with sea ice concentration in the Bellingshausen Sea. In general, we expect sea ice to impede the generation of both the primary and secondary microseism due to its attenuation and coastal/continental shelf shielding of swell from Antarctica. The expected anticorrelation between sea ice and microseism power recorded at PMSA is seen to peak during August, during which the correlation coefficient for the primary

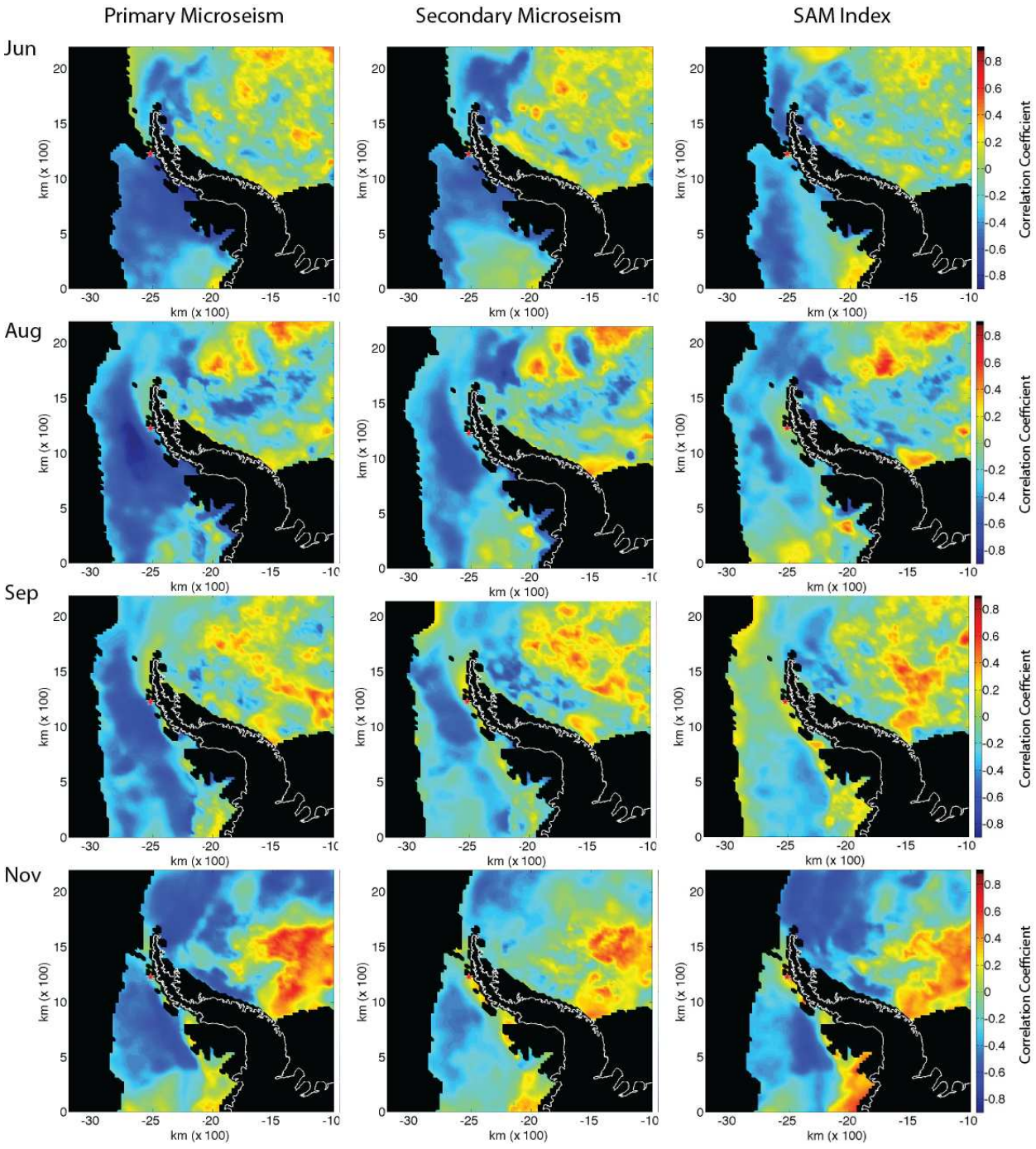

Figure 2.5. Correlations of monthly mean sea ice concentration with integrated primary and secondary microseism power recorded at PMSA (Red Star) and Southern Annular Mode (SAM) Index from 1993-2014. Blue regions indicate anticorrelation between sea ice and microseism/SAM metrics.

microseism reaches -0.90 ~150 km southwest of Palmer Station and the secondary microseism is -0.71 ~200 km due west. The secondary microseism is generally less anticorrelated with sea ice concentration than the primary and is influenced by a smaller areal extent of ice. Given that we are using 22 years of data to perform our correlations, correlation coefficients with an absolute value greater than 0.42 are considered statistically significant at the 95% confidence interval using a two-tailed t test (details and correlation maps for the entire continent available in Appendix 3).

iii. Seasonal Distribution of Extremal Microseism Events

Both EFI and PMSA share a bimodal distribution of peak storm months, with a comparable number (~15) of index hours per month during both May and September (Figure 2.7a). In contrast, secondary microseism index hours for EFI show a single sharp peak of 55 index hours per month in the late winter (late August-September) and absolutely no index hours in the middle of the summer. Meanwhile, PMSA has a large plateau of ~30 index hours per month from April-November. As we illustrate in the next section, these observations are likely due to peak storm activity in the Drake Passage occurring in the late winter coupled with annual variations in sea ice around the AP.

Discussion

i. Influence of Sea Ice on Microseism Intensity

Our results provide direct evidence for the role of sea ice in impeding the generation of both primary and secondary microseisms due to its direct attenuation of wave energy by shielding the coast/continental shelf of the AP from swell. Since major low-pressure systems move clockwise

around the continent in the Circumpolar Westerlies and arrive on the western coast of the AP, the strongest anticorrelations between microseism power and sea ice occur in the northern Bellingshausen Sea (Figure 2.5). In contrast to the Bellingshausen Sea, the Weddell Sea is shielded from the circumpolar westerlies by the AP and retains sea ice through most of the year (Figure 2.1). The accumulation of thicker and mechanically stronger multi-year ice (e.g., *Kovacs*, 1996; *Maslanik et al*., 2007), combined with predominantly westward migrating storm systems inhibits microseism generation along much of the Eastern coast of the AP. Accordingly, primary and secondary microseism anti-correlations with sea ice are often much weaker in the Weddell Sea, particularly poleward of the marginal ice zone.

Secondary microseism power observed at PMSA is much less influenced by near coastal sea ice than primary microseism power, with significant anticorrelation not developing until ~100 km away from the coastlines. This is likely indicative of differences in the source locations between the primary and secondary microseism with the primary microseism arising from direct oceanic wave forcing on the continental shelf and the secondary forming from waves reflecting off the AP and subsequently interfering with incoming waves. An exception to this occurs in the Austral fall (May, June) when secondary microseism power becomes anticorrelated with near coastal ice likely in response to completely ice free sections of the coast generating substantially stronger reflections during periods of anomalously low sea ice.

Correlations between SAM index and sea ice show reduced sea ice concentrations in the Bellingshausen Sea and northwest Weddell Sea during positive phases of the SAM. This effect is the most pronounced during the winter (June-August) and late spring/early summer (November-

January) and shows general agreement with a previous correlation and climate modeling study between sea ice around the AP and phase of the SAM (*Lefebvre et al*., 2004). Specifically, climate modeling and reanalysis results (e.g., *Liu et al*., 2004; *Lefebvre et al*., 2004) indicate that a low-pressure anomaly forms to the west of the Bellinghausen Sea during positive phases of the SAM. This pressure anomaly increases the transport of warm air masses from more northerly latitudes into the Bellingshausen and Weddell seas, contributing to a reduction in sea ice concentration in this region (*Lefebvre et al*., 2004).

We also correlated microseism power at station EFI with sea ice concentrations to investigate whether Antarctic microseism processes affect the seismic spectrum observed at the Falkland Islands, located ~1200 km north of maximum sea ice extent (Figure 2.6). As sea ice begins to build out around the west coast of the AP in May-June, primary microseism power at EFI is found to be anticorrelated with near-coastal sea ice, but secondary microseism power is not. Primary microseism anticorrelations generally weaken and move ~200 km from near-coastal regions of the AP into the northern Bellingshausen Sea as sea ice builds out during the Austral winter and early spring. When maximum sea ice extent is achieved in September, the spatial extent of microseism anticorrelations is limited to the northern tip of the AP. These correlations suggestion that longer-period microseism Rayleigh waves generated in Antarctica are indeed detectable at EFI.

ii. Microseism Propagation Across the Drake Passage

Estimating microseism source regions, particularly for the secondary microseism, can be difficult due to sources being non-impulsive, geographically diffuse, and spatiotemporally variable (e.g.,

Bromirski et al., 2013). Additionally, microseisms may be detected simultaneously at a given seismic station from multiple source regions. Array processing and/or back-projection techniques can be useful where data permit to constrain source azimuths and regions (e.g., *Cessaro*, 1994; *Gerstoft and Tanimoto*, 2007) and/or to correlate microseism observations with other wave state metrics from satellite, buoy, or other observations (e.g., *Bromirski et al*., 1999; *Bromirski and Duennebier*, 2002; *Aster et al*., 2008). However, suitable Antarctic array data and in situ Southern Ocean observations are sparse. Currently, studies of microseism source regions around Antarctica have been limited to backazimuth observations from a two-month broadband seismic array on the Whillans Ice Stream (*Pratt et al*., Submitted), 20-40 s long-period primary microseism observations over 1 year from continent-scale Antarctic arrays (*Koch et al*., 2011), and general correlations with sea ice concentration (*Grob et al*., 2011; *Anthony et al*., 2015).

It has long been established that primary microseism generation commonly occurs in shallow water in near-coastal environments (*Hasselmann*, 1963), however there is debate over whether of secondary microseisms can be generated in deep water (> ~250 m) (e.g., *Cessaro*, 1994; *Obrebski et al*., 2013; *Bromirski et al*., 2013). *Cessaro* (1994) used triangulation from three seismic arrays to locate coastal primary, as well as coastal and deep-water secondary microseism sources in the north Pacific and Atlantic oceans. Of particular interest to that study was a primary microseism source location along the Newfoundland coast that was detected with the Norwegian NORSAR array, indicating that the primary microseism signal can propagate across the Atlantic Ocean. However, *Bromirski et al.* (2013) noted that secondary microseism energy generated in the deep ocean propagates largely within the water column and is strongly reflected as it crosses the threshold between oceanic and continental crust. Therefore, secondary microseism energy

should not be capable of efficiently propagating through ocean basins into other continents. A relevant question in this regard is if primary microseism energy generated along South American and New Zealand coasts can be observed in Antarctica during periods of time when Antarctica sources are sufficiently quiet (i.e.,during maximal sea ice extent) (*Koch et al*., 2011).

The bimodal distribution in both Fourier reconstruction of annual peak primary microseism power (Figure 2.3) and annual microseism index hours (Figure 2.7a) observed at PMSA is likely due to the annual growth and recession of sea ice around Antarctica. Ocean wave activity and peak microseism power in the Southern Ocean peaks in the midst of the Austral winter (e.g., *Aster et al*., 2008), however this coincides with high concentrations of sea ice around the AP. Thus, peaks in microseism power and index hours occur both as sea ice in the Bellingshausen Sea begins to build out and wave activity is increasing (in May) and again as sea ice recedes and wave state is diminishing (in mid-October).

Despite being located well beyond maximal sea ice extent, primary microseism power and storm index hours at EFI exhibit bimodal distributions that have seasonal peaks similar to PMSA. Additionally, correlation analysis between primary microseism power at EFI and sea extent reveals similar trends to PMSA with prevalent anticorrelations in the Bellingshausen Sea during the fall and summer (Figure 2.6). By early spring, increases in sea ice extent and strength in the Bellingshausen Sea have become sufficiently large enough to attenuate microseism generation such that is likely no longer a primary contributor to microseisms observed at EFI. Thus, in contrast to PMSA, the stronger bimodal peak attained from Fourier reconstruction occurs in early September, when storm activity is peaking in the Drake Passage (as identified below from

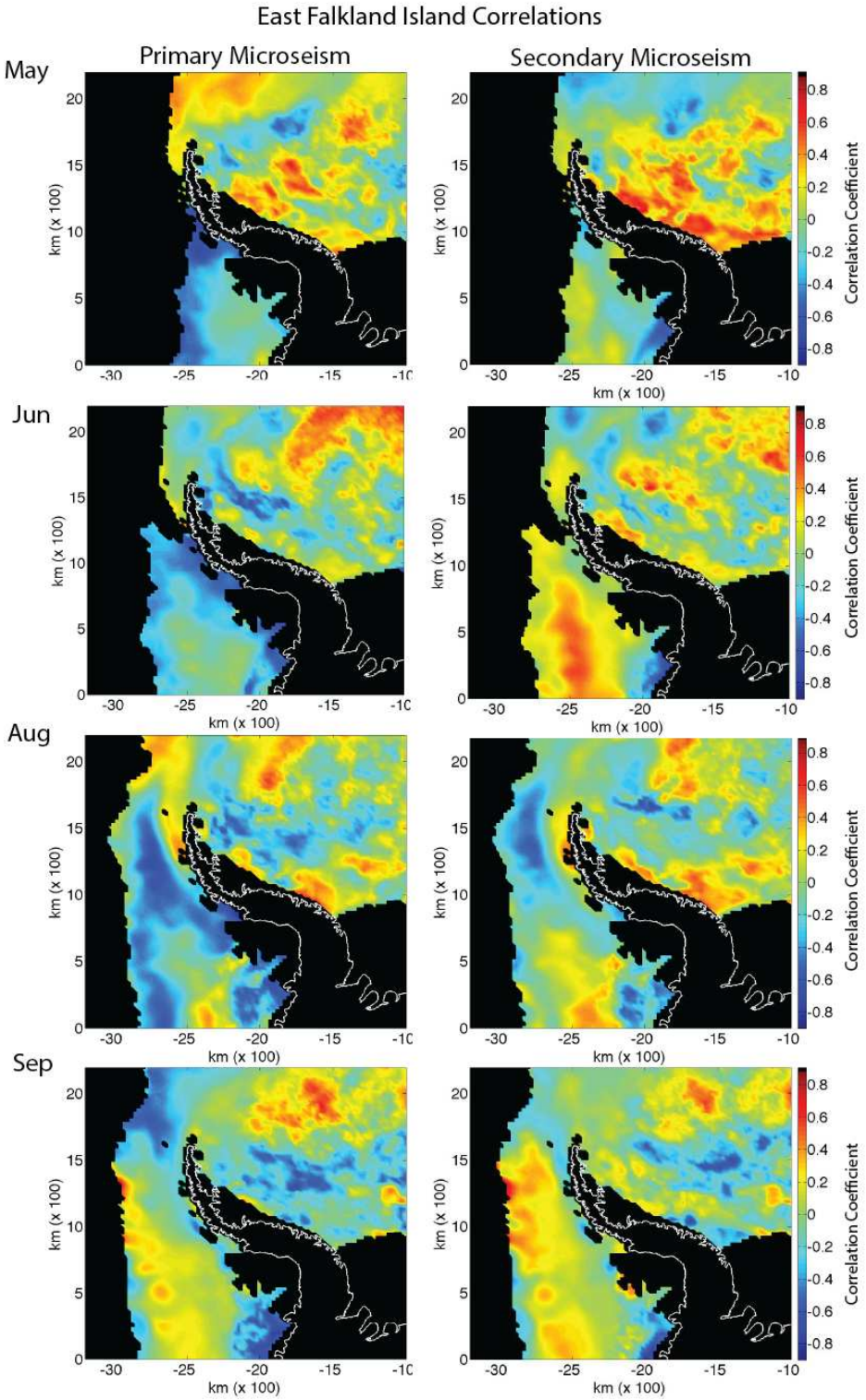

Figure 2.6. Same as Figure 2.5, but for EFI microseism power between 1996-2014.

secondary microseism analysis at EFI). We therefore conclude that during low sea ice conditions on the AP, primary microseism power generated on the western side of the AP is capable of crossing the Drake Passage and being observed at EFI. This finding corroborates the *Cessaro* (1994) observations of primary microseisms crossing the Atlantic Ocean as well as recent findings of coherent 10-25 s noise across ocean basins, including the Drake Passage (*Lin et al*., 2006).

In contrast to the primary microseism, secondary microseisms at EFI exhibit both a single peak in Fourier reconstruction and extremal index hours. Both peaks occur in late August/early September suggesting that wave state and storm activity in the Drake Passage reaches a maximum during this time. Additionally, correlation analysis between secondary microseism power at EFI and sea ice in the Bellingshausen Sea show few robust anticorrelations, again suggesting that higher frequency secondary microseism energy does not efficiently propagate across the Drake Passage.

iii. Southern Annular Mode Influence on Drake Passage Storminess and Microseism Intensity

To characterize the influence the SAM has on storm activity in the Drake Passage, we construct monthly ratios of primary and secondary index hours during negative (below 35th percentile) and positive (above 65th percentile) SAM phases with mean monthly index hours across all years (Figure 2.7b,c). These thresholds were chosen such that each calendar month for both positive and negative phases of the SAM were represented by a minimum of four months. The ratio is used to succinctly express how microseism index hours recorded during months of positive and

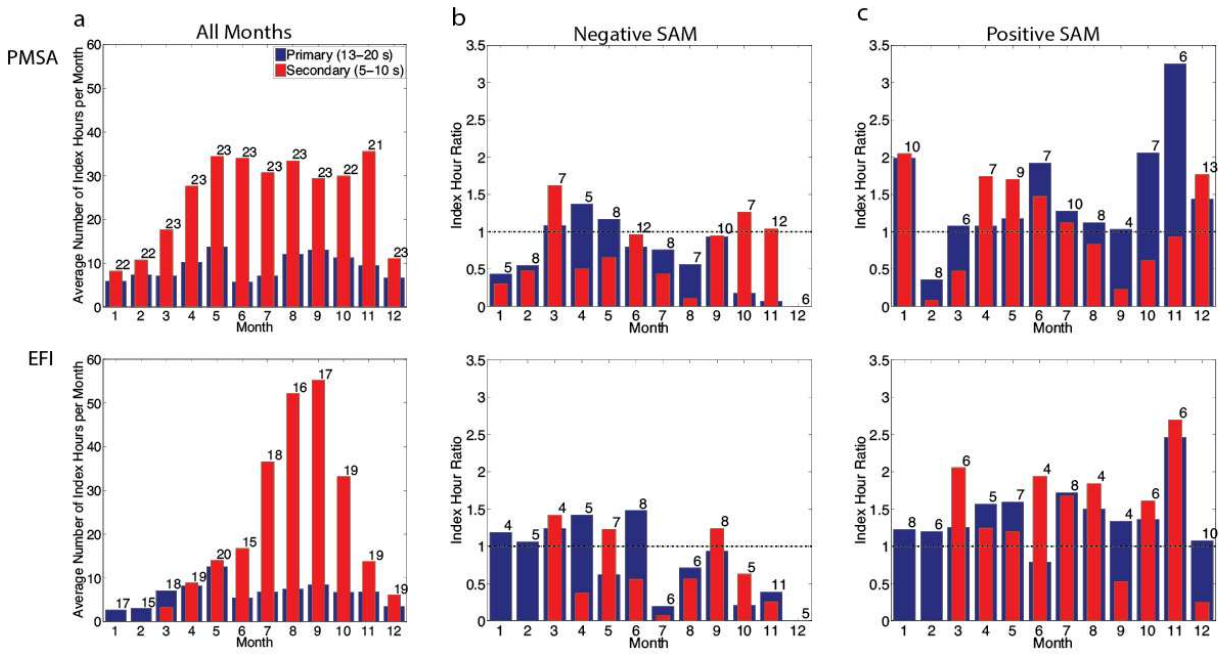

Figure 2.7. (a) Mean monthly distribution of primary (blue) and secondary (red) microseism storm index hours for PMSA and EFI for all months (minimum 65% seismic data completeness). (b,c) Ratios of microseism index hours for months falling in the bottom (b) and top (c) 35th-percentile SAM index compared to a mean month. Numbers next to bar plots indicate the total number of years that satisfy the requirements of data completeness and have a negative (b) or positive (c) SAM index for each calendar month. All monthly index hour calculations have been normalized to a 30-day month.

negative phases of the SAM compare to monthly means across all years. Values greater than 1 indicate that more extremal microseism events are occurring during the given phase of the SAM. As the secondary microseism recorded at EFI is likely not influenced by Antarctic sea ice, we use it as the most robust proxy for characterizing changing wave and storm conditions in the Drake Passage.

Our observations indicate that positive phase of the SAM is associated with greater wave and storm activity within the Drake Passage. As no secondary microseism index hour events are ever recorded in January and February at EFI, the remaining 10 calendar months were used observe the impact phase of the SAM has on storm activity. A higher number of extremal microseism events occur during positive phase of the SAM during 8 of these months, with 6 months showing an increase in index hours of at least 50% compared to monthly means (Figure 2.7c). Additionally, every month except June shows an increase in primary microseism index hours, though the effects of sea ice reduction in the Bellingshausen Sea during positive phases of the SAM likely contribute to this statistic. We infer from these results that increased storm activity is prevalent during the positive phase of the SAM, particularly in the Austral fall through spring. This is consistent with satellite altimeter data also observing larger extreme wave heights in the Southern Ocean during positive phase of the SAM (*Izaguirre et al*., 2011).

Extremal primary microseism events recorded at PMSA increase drastically during positive phase of the SAM during the months of June and October-January with anomalous activity peaking in November when the number of index hours increases by over 300%. We attribute this remarkably high sensitivity of the June and October-November index hours to high inter-annual

variability of near-coastal sea ice during these months coupled with near-coastal sea ice concentrations being highly modulated by phase of the SAM (Figure 2.5). During positive phases of the SAM, larger extents of west AP coastline are exposed to direct ocean forcing, which results in stronger primary microseism signals. Note that the secondary microseism, which is not as highly correlated with sea ice concentrations around the AP during the Austral spring, does not show October and November increases in index hour hours during the positive phase of the SAM, which further underscores the heightened sensitivity of the primary microseism to near coastal sea ice relative to the secondary.

During December and January, both primary and secondary microseism index hours observed at PMSA increases by at least 50% during positive phase of the SAM and decrease by over 50% during the negative phase of the SAM (Figure 2.7b,c). In fact, no primary or secondary index hours occur during any of the six Decembers with a low SAM index. As the coast of the AP is relatively ice free during these months, changes in Drake Passage wave activity are likely responsible. This conclusion is supported by the seasonal signature of the SAM which becomes the most coupled with the troposphere during December and January and drives strengthened westerly winds centered near 60°S during positive phases (*Thompson and Solomon*, 2002; *Thompson et al*., 2011). In contrast, winds near 40°S are reduced, which may explain the lack of strong coupling between phase of the SAM and index hours recorded at EFI (latitude 51°S) during the summer months.

Conclusions

The AP is an especially valuable locale for studying the microseism effects of large wave and weather systems interacting with annual and secular sea ice variability. We use microseism observations from Palmer Station and East Falkland Island to develop a correlation-based methodology to characterize the seasonal variability and spatial extent of sea ice which impact primary and secondary microseism power recorded at these stations. We find that primary microseism intensity is overall more sensitive to sea ice concentration than the secondary microseism, particularly near-coastal (< ~100 km) sea ice. These observations have implications for future use in using microseism intensities recorded at high latitude stations to augment sparse field observations of sea ice strength and swell attenuation (e.g., *Kohout et al*., 2014; *Mahoney et al*., 2016), which are becoming increasingly important to characterize following the rapid decline of Arctic sea ice (e.g., *Asplin et al*., 2012; *Thomson and Rogers*, 2014).

Biannual primary microseism power peaks at Palmer Station and East Falkland Island and their similar sensitivities to sea ice concentration suggested by correlation analysis indicate that longer period Rayleigh waves signals generated near the AP are capable of crossing this sector of the Southern Ocean. These observations corroborate earlier studies on primary microseism source regions and propagation paths which suggest that longer period microseism signals are capable of crossing oceanic basins (*Cessaro*, 1994; *Lin et al*., 2006). The strong dissimilarities in secondary microseism records on either side of the Drake Passage indicates that the shorter period components of microseismic Rayleigh waves are incapable of efficiently propagating from ocean basins to the continental shelf, as supported by the conclusions of *Bromirski et al*. (2013). Continued refinement of both microseism source regions and seismic wave propagation

will be important to further assess the factors affecting short and long-term microseism intensity across the Earth, and for the general use of seismic records to constrain integrated ocean wave state and storminess, both episodically and over long time periods (*Aster et al*., 2008, 2010; *Stutzmann et al*., 2009).

Finally, we demonstrate that extremal storm activity in the Drake Passage increases during positive phases of the SAM and that storm tracks appear to shift poleward during the Austral summer. As the positive phase of the SAM also introduces higher temperatures and reduced sea ice concentrations around the AP, such increases in storm activity in reduced ice situations will augment microseism generation as well as increase the exposure of tidewater glacial systems, including ice shelves, to ocean wave perturbation. The potential role of this process to 21st century ice shelf collapse events on the AP remains an open question.

Chapter 3: Seismic Monitoring of Snowmelt Runoff in the Northern Colorado Rocky Mountains

Introduction

Flow and sediment transport in fluvial systems plays a critical role in shaping river morphology and aquatic ecosystems as well in the design of societal river infrastructure such as dams, bridges and water treatment facilities. Due to spatial-temporal variability of flow, sediment flux and the hazards associated with in-channel measurements, in situ measurements of flow and sediment transport may be unable to provide a comprehensive record, especially in flood conditions or where such measurements may alter the river system (*Bunte and Abt*, 2005). Quantitative understanding of the relationships between river discharge, sediment transport, and excitation of the seismic wavefield, has the potential to usefully augment sampling methods of fluvial systems with a non-invasive methodology.

Multiple environmental processes at Earth's surface contribute significantly to the local and, in some cases, global seismic wave field (e.g., *Aster et al*., 2008, 2010; *Larose et al.*, 2015). Recent studies have begun laying the observational (e.g*., Burtin et al.*, 2008, 2011,2016; *Hsu et al*., 2011; *Schmandt et al*., 2013; *Bartholomaus et al.,* 2015,; *Roth et al*., 2016) and modeling (*Tsai et al.,* 2012; *Gimbert et al*., 2014) framework necessary to interpret riverside seismic observations for fluvial discharge and bed load transport characteristics. In general, these studies have shown that bed-load transport tends to excite higher-frequency (> 15 Hz) signals (*Schmandt et al*., 2013; *Roth et al*., 2016), while turbulent flow and discharge modulates seismic power between ~1-10 Hz (*Burtin et al.*, 2011; *Gimbert et al*., 2014; *Bartholomaus et al.,* 2015). Through calibration of

seismic signals in the Swiss Prealps with measured bed load, *Roth et al.* (2016) were able begin to accurately invert for bed load transport rates using only calibrated seismic data, precipitation rates, and discharge measurements. However, discharge measurements typically rely on in-channel measurements of stage height (e.g., pressure transducers), which may be destroyed during flood events (e.g., *Burtin et al.*, 2011; S. Ryan (USFS), pers. Comm.). As a majority of sediment transport is anticipated to happen at high levels of discharge, interpretations from the seismoaccoustic wavefield collected outside the channel have the potential to usefully augment the monitoring and advance general understanding of fluvial systems.

The fluvial excitation of infrasound (< 20 Hz) signals has been relatively unexplored outside of a study of waterfall noise (*Johnson et al*., 2006) and a study of the 2012 Controlled Flood Event in the Grand Canyon (*Schmandt et al*., 2013). In the Grand Canyon study, both the rising and falling limb of the controlled flood, 6-7 Hz acoustic and 2-12 Hz seismic signals were generated that were interpreted to be the result of fluid-air interactions, such as breaking of waves at the river surface. However, the 2-12 Hz seismic signal has subsequently been modeled and attributed to turbulent flow while the exact source of the 6-7 HZ acoustic signals remains unknown (*Gimbert et al*., 2014).

Here, we investigate signals recorded on a seismoaccoustic array co-located with discharge, suspended sediment, and precipitation measurements between May and September of 2015 from the South Fork of the Cache la Poudre River, a highly seasonal snow melt- and rain-fed mountain river in the Front Range of the Colorado Rocky Mountains. In contrast to previous studies, which generally record seismic observations ~15-50 m from the river and analyze short-

period (< 1 Hz), vertical component noise, we deploy instruments within 1 m of the river and attain both short-period (12-22 Hz) and intermediate-period (0.5-3.3 s) horizontal component signals that are highly sensitive to discharge. We propose that the intermediate-period signals arise from instrument tilt as the sensor directly interacts with channel flow within the hyporheic zone and or responds to nearby forces at the edge of the river system. We suggest these results offer the potential for a new method of estimating discharge rates and, potentially, tracking hyporheic exchange.

Field Site and Data

The South Fork of the Cache la Poudre River is a small mountain stream that originates in the Mummy Range of Rocky Mountain National Park, Colorado and has a drainage area of 231 km^2 (*Ryan*, 2007). The study site (Figure 3.1a) features a straight, north-south section of the river with a ~1% grade, a riffle channel morphology, and a 14 m bankfull channel width. The site was selected by the US Forest Service (USFS) to monitor changes in suspended sediment load following the 2012 High Park fire, which burned over 35,000 ha including a portion of the South Fork Cache la Poudre watershed. To facilitate these monitoring efforts, the USFS installed a pressure transducer, calibrated turbidity sensors, and a rain gauge to enable continuous (10 minute sampling interval) collection of discharge, suspended sediment, and precipitation data from 2013-2015 (Figure 3.1b). Stage height, as measured by the pressure transducer, is converted to discharge through a series of rating curves attained by measuring both channel geometry and flow velocity multiple times over the course of the rising and falling limb of spring snowmelt runoff. Here, we focus on data collected between 17 May and 1 September 2015,

Figure 3.1. (a) Field site along the South Fork of the Cache la Poudre River, Northern Colorado. Seismic stations SF01-SF03 are shown along with infrasound sensors locations (blue circles, sensor 1 co-located with seismic stations). (b) Locations of rain gauge, pressure transducer, and turbidity meter. (c) Three-component Sercel L28 (4.5 Hz lower corner frequency) geophones were placed ~1 m from the channel and at water table depth during low flow conditions in mid-May. This reach of the river runs nearly north-to-south, so that the N component of the seismometer is very nearly parallel, and the E component very nearly perpendicular to flow, which is to the right (south) in (a) and (b).

during which fluvial measurements were augmented by the installation of a seismoaccoustic array.

From mid-May to early September we installed three 3-component L28 geophones (corner frequency 4.5 Hz) 1 m from the river at distances of 12 m, 23 m, and 35 m downstream of the pressure transducer (Figure 3.1a). Each sensor was emplaced ~ 0.3 m deep in close proximity to the water table during moderate (~3.2 m^3/s) flow conditions (Figure 3.1c). Until early August, stations SF02 and SF03 were each supplemented with a 15 m aperture array of three ground-mounted infrasound sensors with a corner frequency of 0.05 Hz (*Marcillo et al.*, 2012). Station SF01 recorded at 250 Hz, while stations SF02 and SF03 recorded at 125 Hz. All stations experienced a small (4-5 days) data gap in mid-June when the flash cards on each data logger became full and the station stopped recording.

During the study period, discharge varied between 1-16 m^3/s including strong modulation from the rising and falling limbs of spring snow melt in June, an intense rainstorm in early July, and an upstream dam release on 26 July that more than doubled discharge over the course of an hour (Figure 3.2a). The dam release lasted for nearly three weeks and maintained elevated levels (5-6 m^3/s) of discharge during this time period before closure of the dam dropped flow rates to ~1 m^3/s in late August.

Suspended sediment loads were generally < 10 mg/L, but increased drastically (up to ~100 mg/L) following rain events and increases in discharge (Figure 3.2b). The spring snowmelt cycle shows general clockwise hysteresis between suspended sediment and discharge with higher

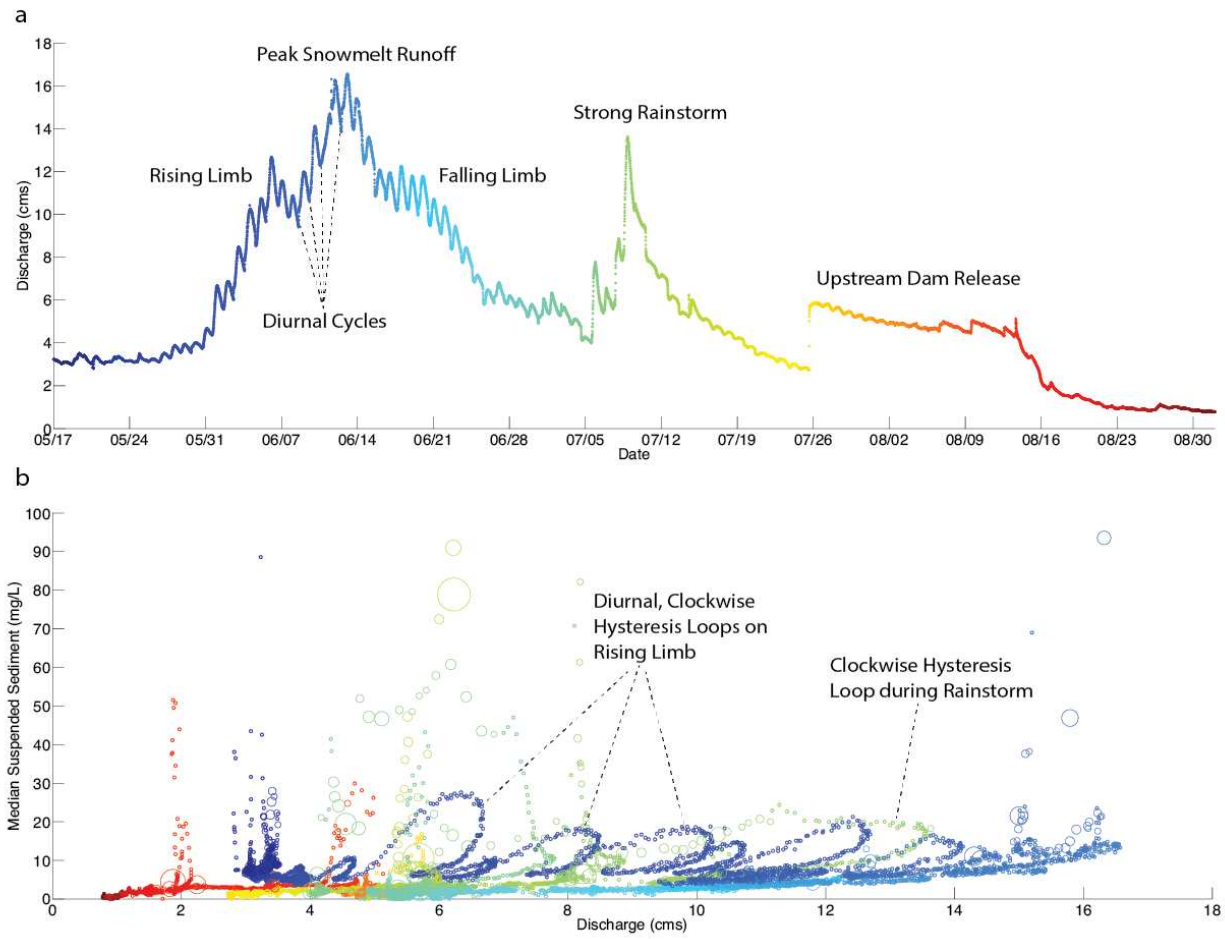

Figure 3.2. (a) Hydrograph over the study period as determined by pressure transducer measurements of stage height and multiple rating curves. The hydrograph is color coded by time and has significant events leading to changes in discharge labeled. (b) Suspended sediment concentrations versus discharge (sampled every 10 minutes) color coded by time using the same color scale as in 3.2a. Clockwise hysteresis loops are observed both on the rising limb of snowmelt runoff and during the July Rainstorm event. Marker size corresponds to co-located precipitation measurements.

levels of suspended sediment observed on the rising limb. Clockwise hysteresis loops are typical and arise from available sediment next to the channel being removed, transported, and quickly depleted (e.g., *Seeger et al.,* 2004). We additionally observe clockwise hysteresis loops accompanying each diurnal pulse of increased discharge on the rising limb and during the early July rainstorm event.

Spectral Analysis

To observe how variations in discharge and suspended sediment concentrations impact the seismoaccoustic wavefield, we perform our analysis in the frequency domain for moving time windows. After deconvolving the instrument responses, each channel of seismic and infrasound data was converted to 10-minute window acceleration power spectral density (PSD; in dB relative to 1 m^2/s^4/Hz for seismic and 1 Pa for infrasound data) estimates with 50% temporal overlap using the Incorporated Research Institutions for Seismology (IRIS) Noise Took Kit (NTK) (*Bahavar et al.,* 2013). Similar to PQLX (*McNamara and Buland*, 2004; *McNamara and Boaz*, 2011), the NTK employs Welch's section averaging method (e.g., *Oppenheim and Schafer,* 1975) to break each 10-minute window into 13 sub-segments of 75% overlap and returns PSD estimates for each 10-minute window in 1/8-octave period bins and 1 dB power increments. However, in contrast to the default 1-octave smoothing window used in PQLX, the user can specify the degree of PSD smoothing within the NTK. We specify a smaller, ¼-octave smoothing window to minimize smearing of power across period bins and attain higher resolution PSD estimates. All PSD estimate start times are converted to Mountain Daylight Time and resulting spectrograms are co-registered with the midpoint of each 10-minute fluvial measurements.

Results

i. Infrasound Spectral Analysis

Infrasound measurements were dominated by quasi-diurnal, 0.1-3 Hz spikes, that were often 180° out of phase with diurnal discharge variations (Figure 3.3). These signals show a generally red spectrum, vary in duration from 10-16 hours, and typically began in mid-late morning and subsided late in the evening. The spectral characteristics and timing of these events are consistent with wind-generated noise, a well-known and common issue when using infrasound sensors that are not equipped with wind filters (e.g., *Hedlin and Alcoverro*, 2005). We were unable to reliably identify acoustic signals originating from fluvial processes occurring on the South Fork of the Cache la Poudre River and conclude that infrasound sensors without wind filters, even when deployed at ground level, are likely unsuitable for monitoring acoustic signals originating from smaller fluvial systems.

ii. Broad Seismic Response to Changes in Discharge

Spectral analysis of ground motion reveals a fairly broadband (~0.1-45 Hz) seismic response to changes in fluvial discharge (Figure 3.4). These variations become even more pronounced after subtracting in dB space (normalizing) the signals by the median PSD recorded during times of minimal discharge (1.0-2.0 m^3/s) in late August following the dam release (Figures 3.5-3.7). We use the residual acceleration power spectrograms along with correlation analysis between seismic power and discharge (Figure 3.8) to identify three distinct bands (0.33-2 Hz, 12-22 Hz, 30-45 Hz) are excited by flow and show strong features associated with discharge variations.

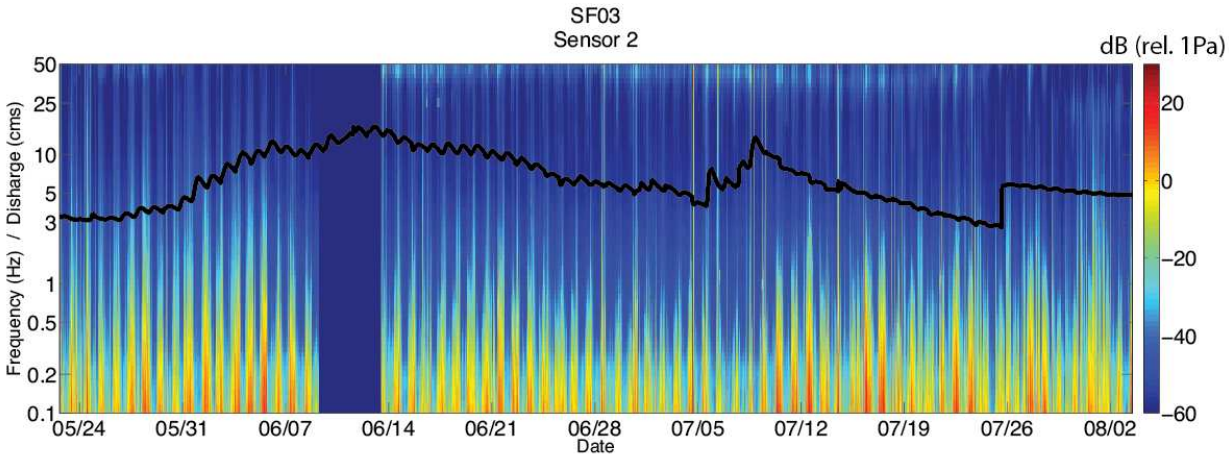

Figure 3.3. Representative infrasound spectrogram (dB rel. 1 (Pa/s)/Hz) recorded on microphone 2 of station SF03 with discharge overlain (black curve). The quasi-diurnal spikes in power between 0.1-3 Hz are likely caused by diurnal winds, which commonly peak in the afternoon.

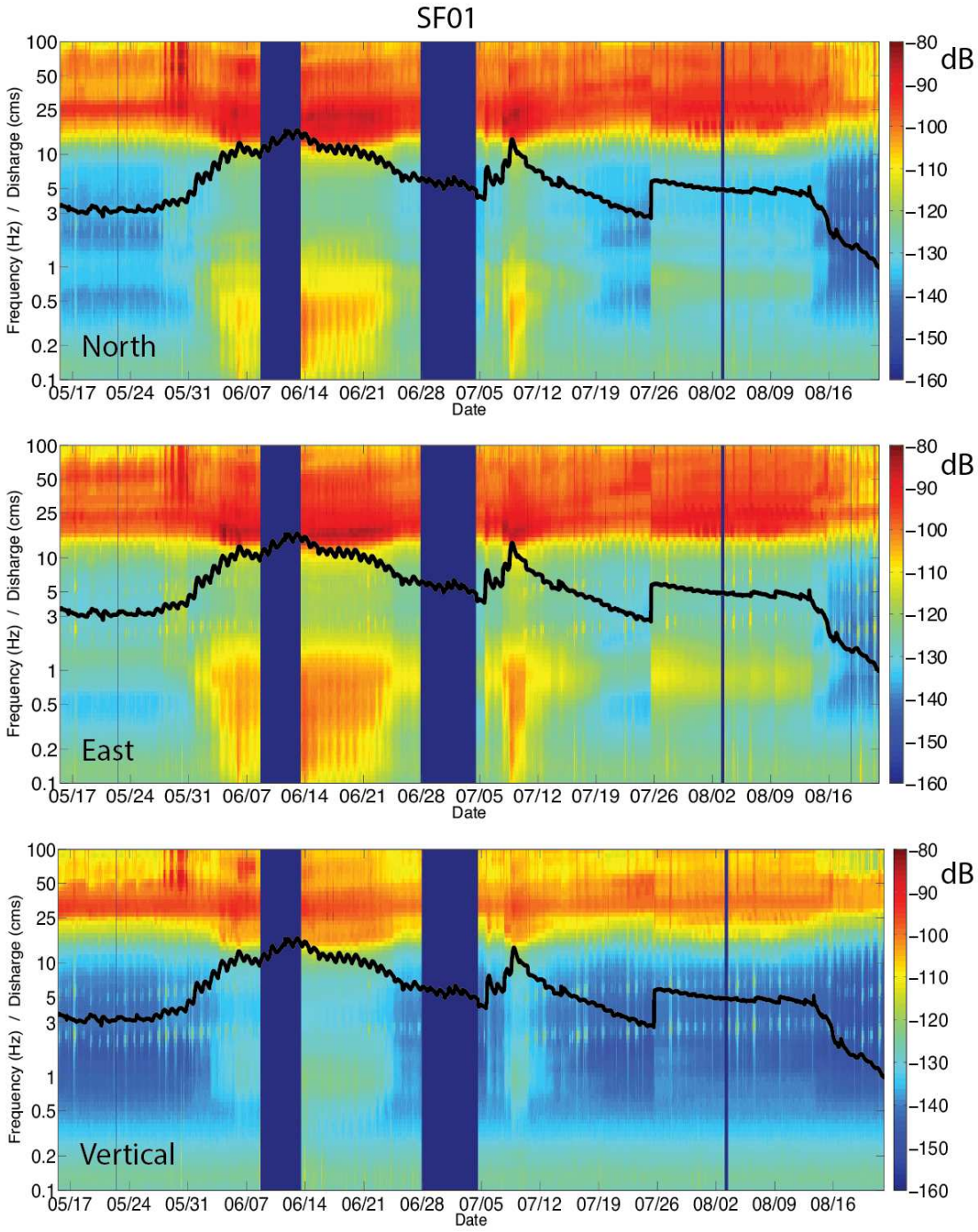

Figure 3.4. Ground acceleration spectrograms for all components of SF01 (dB rel. 1 $m^2/s^4/Hz$) with discharge overlain (black curve).

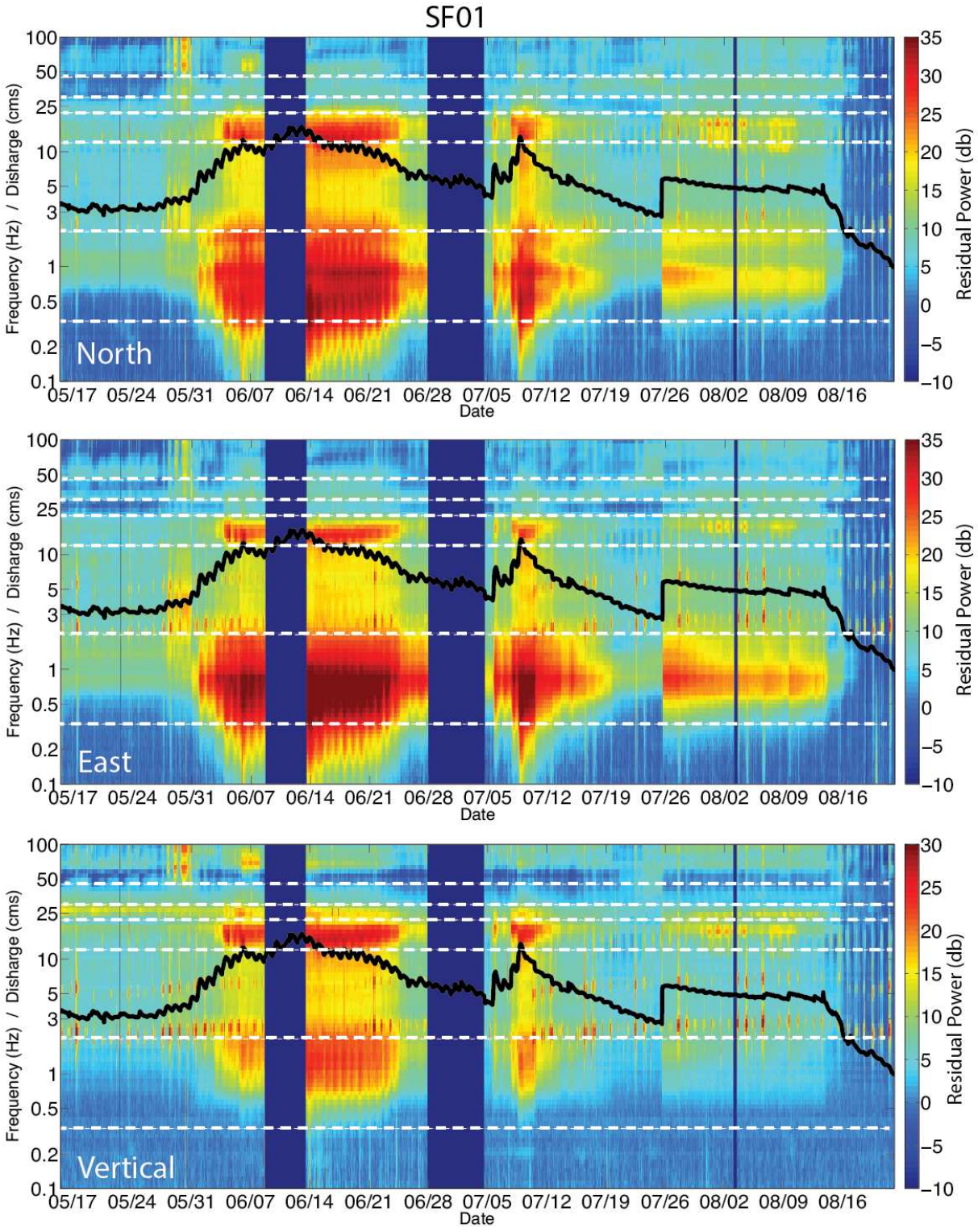

Figure 3.5. Residual ground acceleration spectrograms for all components of SF01 after subtracting the median power spectral density once discharge drops below 2 m^3/s in late August. Horizontal, white dashed lines indicate frequency bands identified through correlation analysis (Figure 3.8) to be sensitive to discharge.

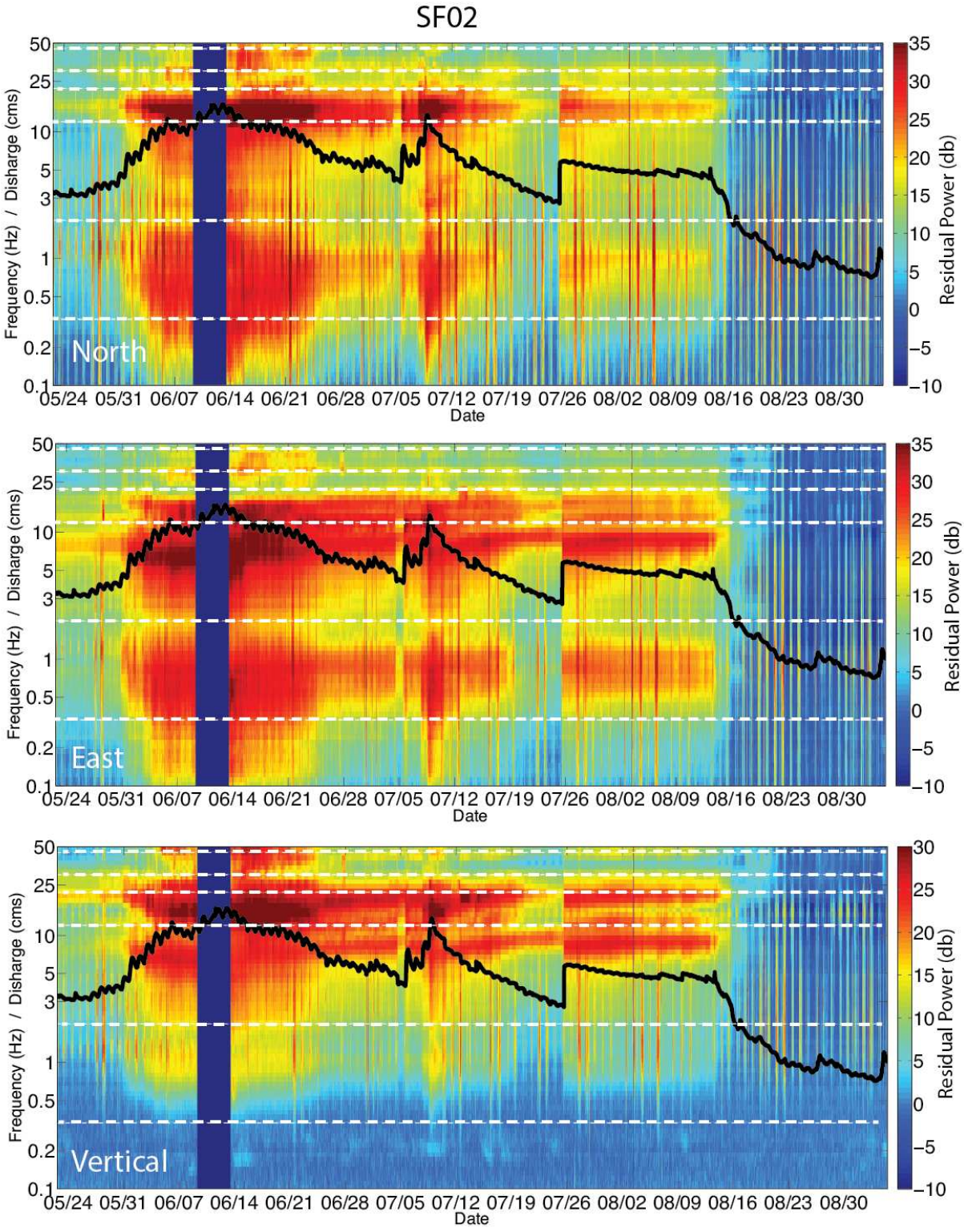

Figure 3.6. Same as Figure 3.5 but for station SF02. The quasi-diurnal higher frequency spikes in power are attributed to wind generated as described in the text.

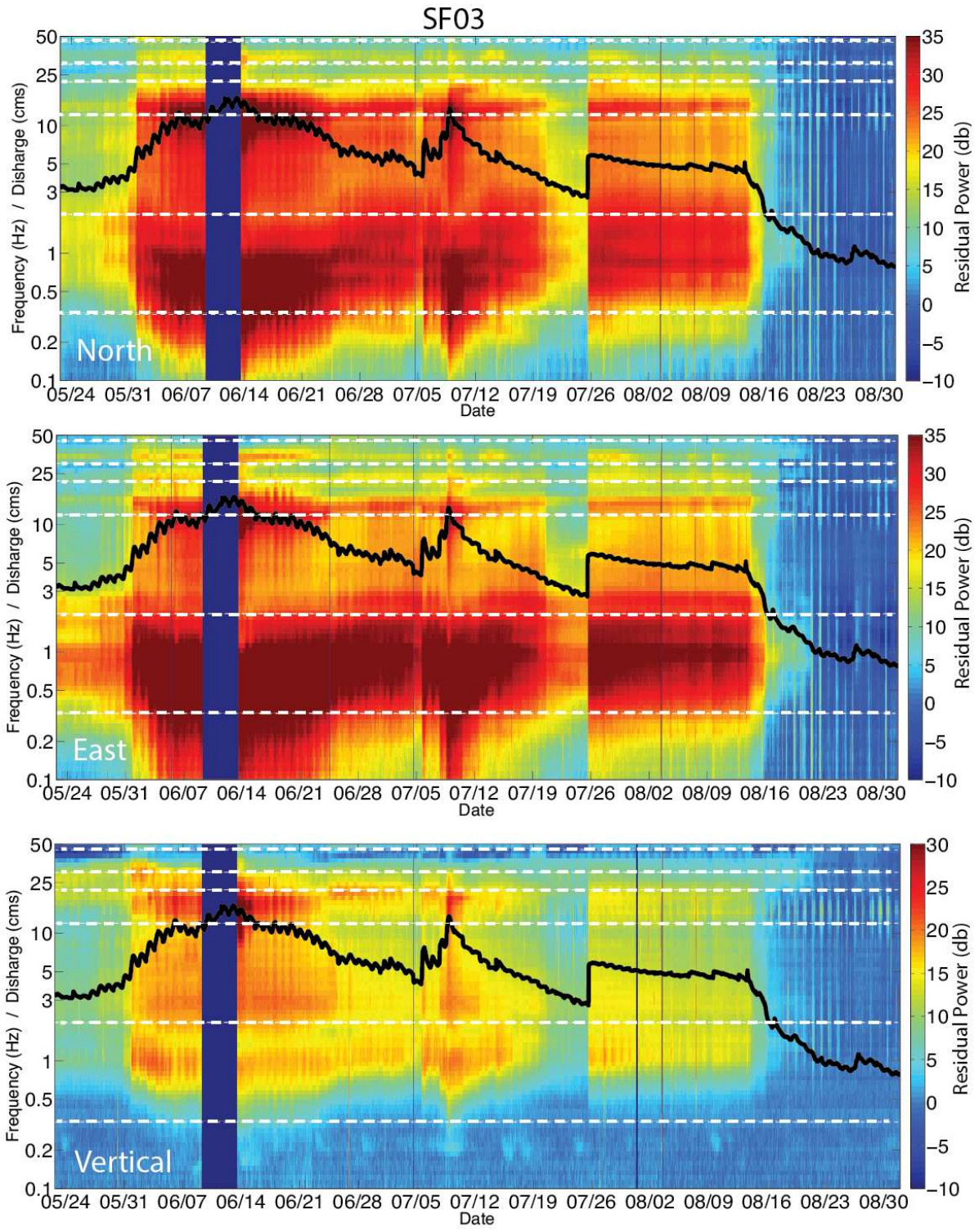

Figure 3.7. Same as Figure 3.5 and 3.6 but for station SF03.

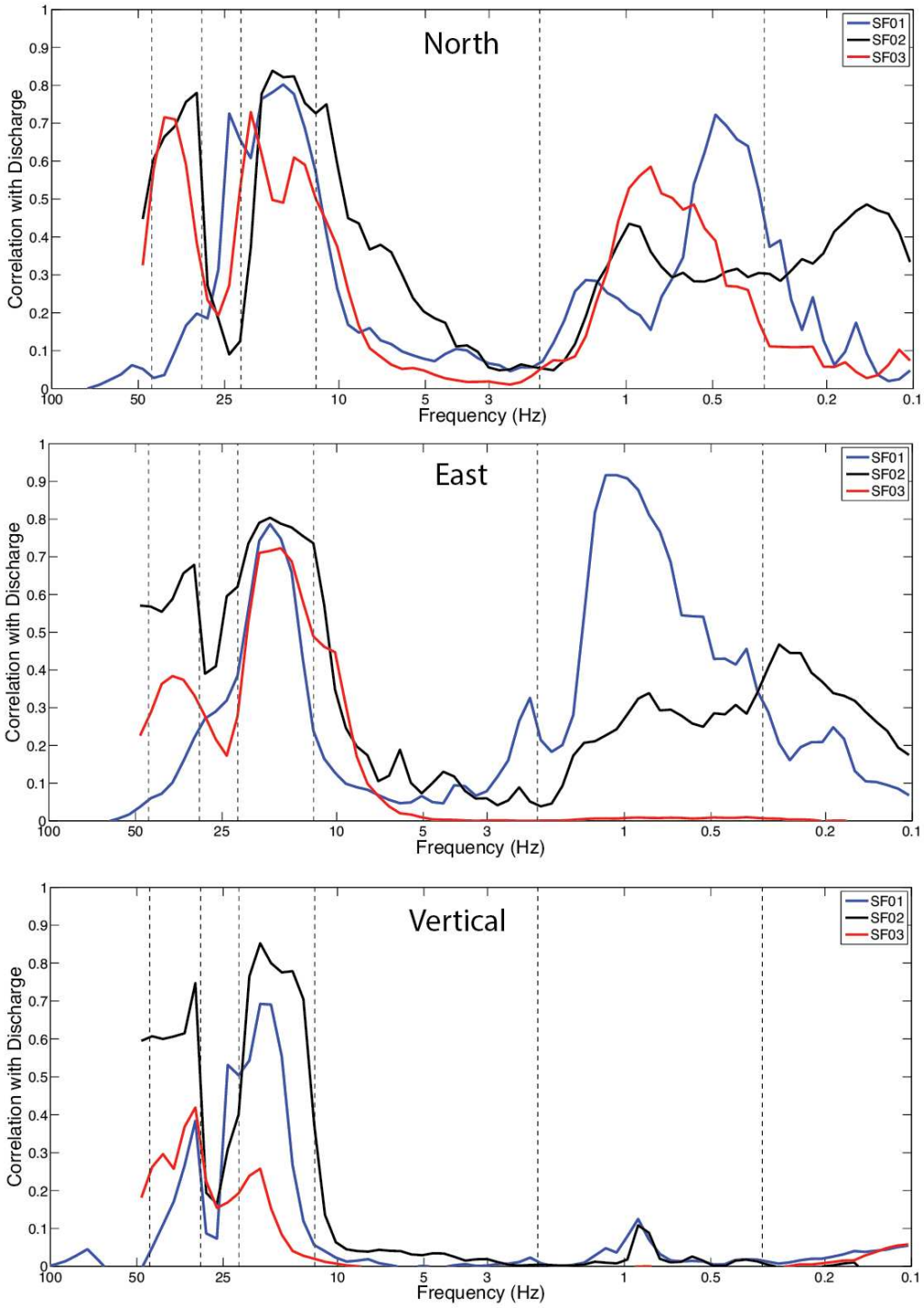

Figure 3.8. Correlation coefficients between discharge and ground acceleration power as a function of frequency at each component of all three stations. The black dashed vertical lines indicate frequencies of 0.33, 2, 12, 22, 30, and 45 Hz and delineate the three frequency bands excited by changing discharge and used in Figures 3.10-3.15.

The lowest frequency band excited by discharge occurs predominantly on the horizontal seismometer components, is readily observed at all three stations, and shows the strongest correlations with discharge between ~0.33-2 Hz. During times of maximal discharge (runoff peak, rainstorm event), the signal extends out to longer periods (up to 10 s, despite the 4.5 Hz lower corner frequency of the seismometers) on both horizontal components and shows power increases of >35 dB (over 3,100 times more power) compared to minimum discharge levels. During the rising and falling limb of snowmelt runoff, diurnal changes in power excited within this band occur exactly in phase with daily variations in discharge. The quasi-diurnal, 0.1-10 Hz spikes, that appear on station SF02 are correlated with strong wind events identified in the infrasound record and are suggested to arise through direct coupling of the geophone with nearby tree roots.

The 12-22 Hz band is, overall, the best correlated with discharge, with a correlation coefficient of at least 0.6 observed on each component of every sensor except the vertical component of SF03 (Figure 3.8). Increases in power in this band are clearly seen accompanying rising discharge on residual power spectrograms, though the band appears to extend down to ~5 Hz on the horizontal channels of SF03. Additionally, the east and vertical components of SF02 appear to show a second, lower frequency band excited by increases in discharge between 5-10 Hz.

The highest frequency 30-45 Hz band is often transiently excited in unique ways at each station. For instance, signals in this band are never observed on the horizontal components of SF01, but power in this frequency range appears to rise by ~5 dB on the vertical component during the rainstorm event. At SF02, 30-45 Hz power levels rise by >20 dB during snow melt runoff, but

record a weaker (~15 dB peak) and higher frequency (40-50 Hz) response to the rainstorm and dam release events.

iii. Seismic Response to the Snowmelt Runoff and Rainstorm Events

To infer further about the nature of each of the three frequency bands excited by changing flow conditions, we track power in each band at each station during both June snowmelt runoff and the week long rainstorm event in early July (Figure 3.9). Specifically, we examine each band for characteristic hysteresis patterns between seismic power and discharge that are typically suggestive of bedload transport (e.g., *Burtin et al.* 2008*; Hsu et al*., 2011; *Schmandt et al*., 2013) or mirror our observations of suspended sediment concentrations. To be consistent with previous studies, we integrate our acceleration PSDs and report our findings here in terms of variations in velocity power.

The 0.33-2Hz band generally shows smooth, approximately exponential increases in seismic power with discharge, especially on the horizontal components, where increases of up to 20 dB are observed during the rising limb of snowmelt runoff (Figure 3.10, 3.11). Additionally, overall power levels are generally 20-30 dB higher on the horizontal components compared to the vertical components. Moderate counter-clockwise (CCW) hysteresis occurs on all components of SF01 and weak clockwise (CW) hysteresis is experienced by the vertical components of SF02 and SF03 during snow melt runoff but not during the July rainstorm. We again note that SF02 experiences transient increases in power on all components in this band, which we attribute to wind coupling with the seismic sensor through vegetation.

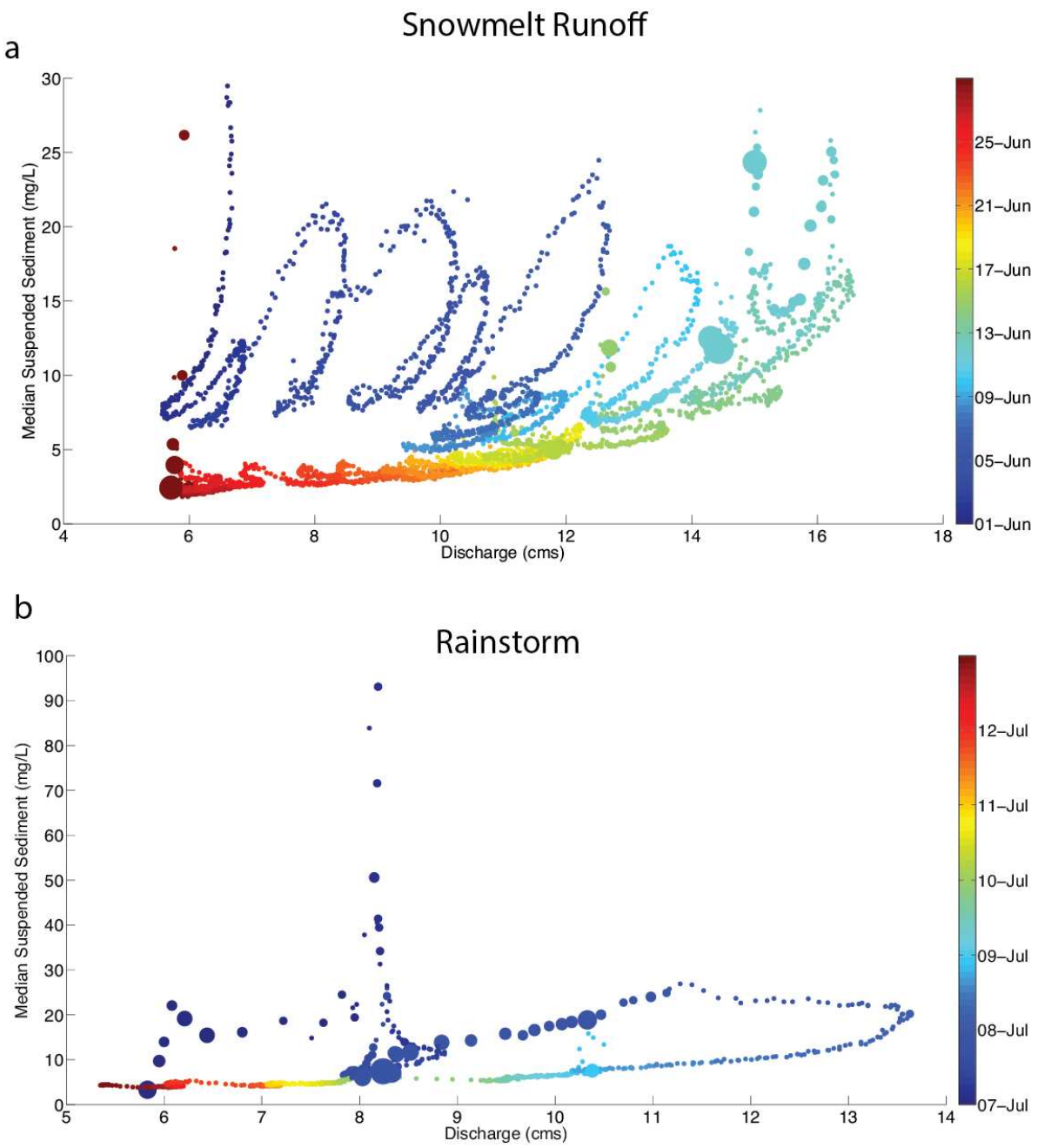

Figure 3.9. Suspended sediment concentration versus discharge for (a) the rising and falling limbs of snowmelt runoff and (b) the July rainstorm event taken at 10-min intervals. Markers are color coded by date and scaled by co-located precipitation measurements.

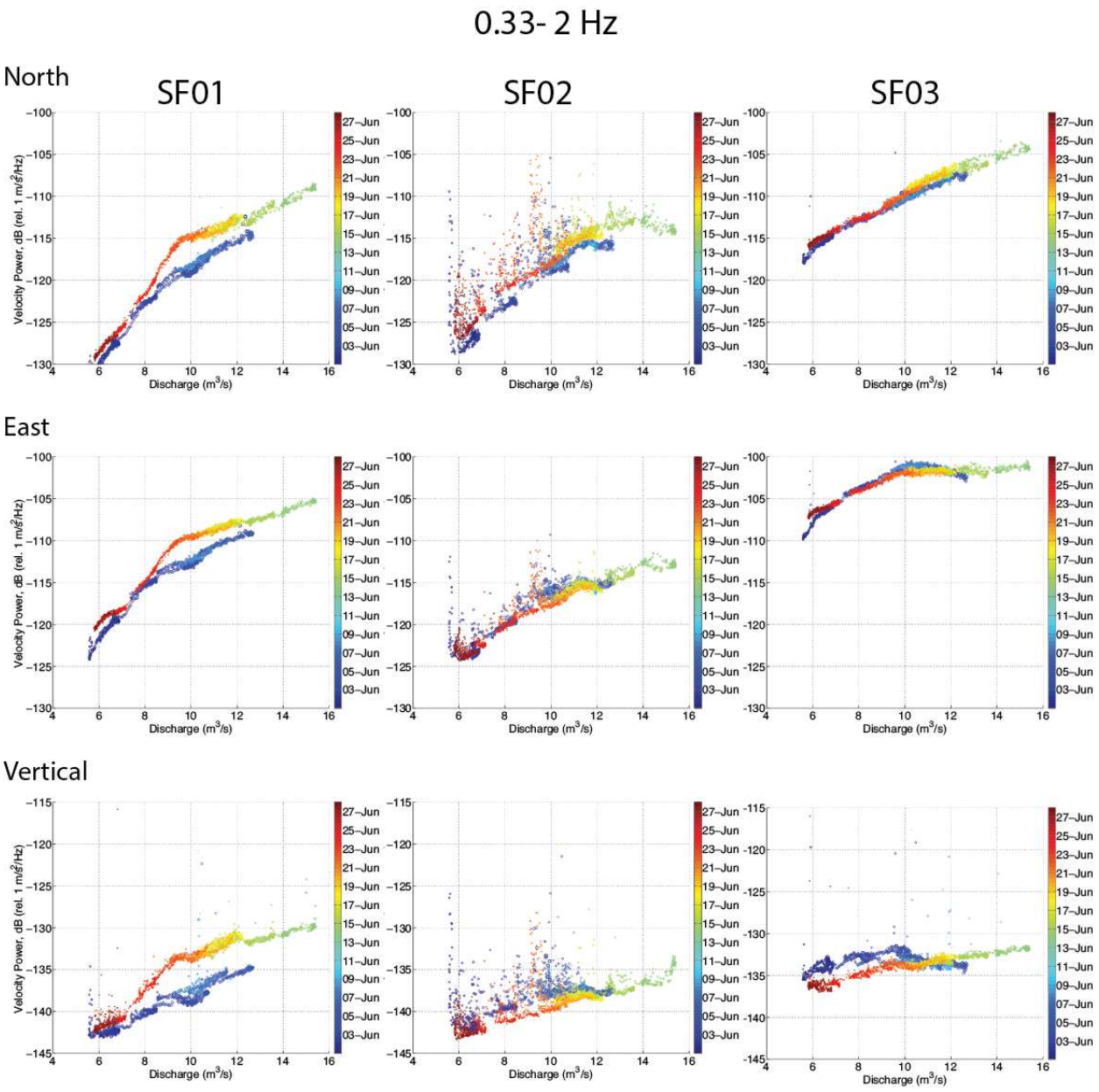

Figure 3.10. Ground velocity (dB rel. 1 (m/s^2)/Hz) from 0.33 to 2 Hz versus discharge for the rising and falling limbs of snowmelt runoff on all three components of each station. Plots are color coded by date.

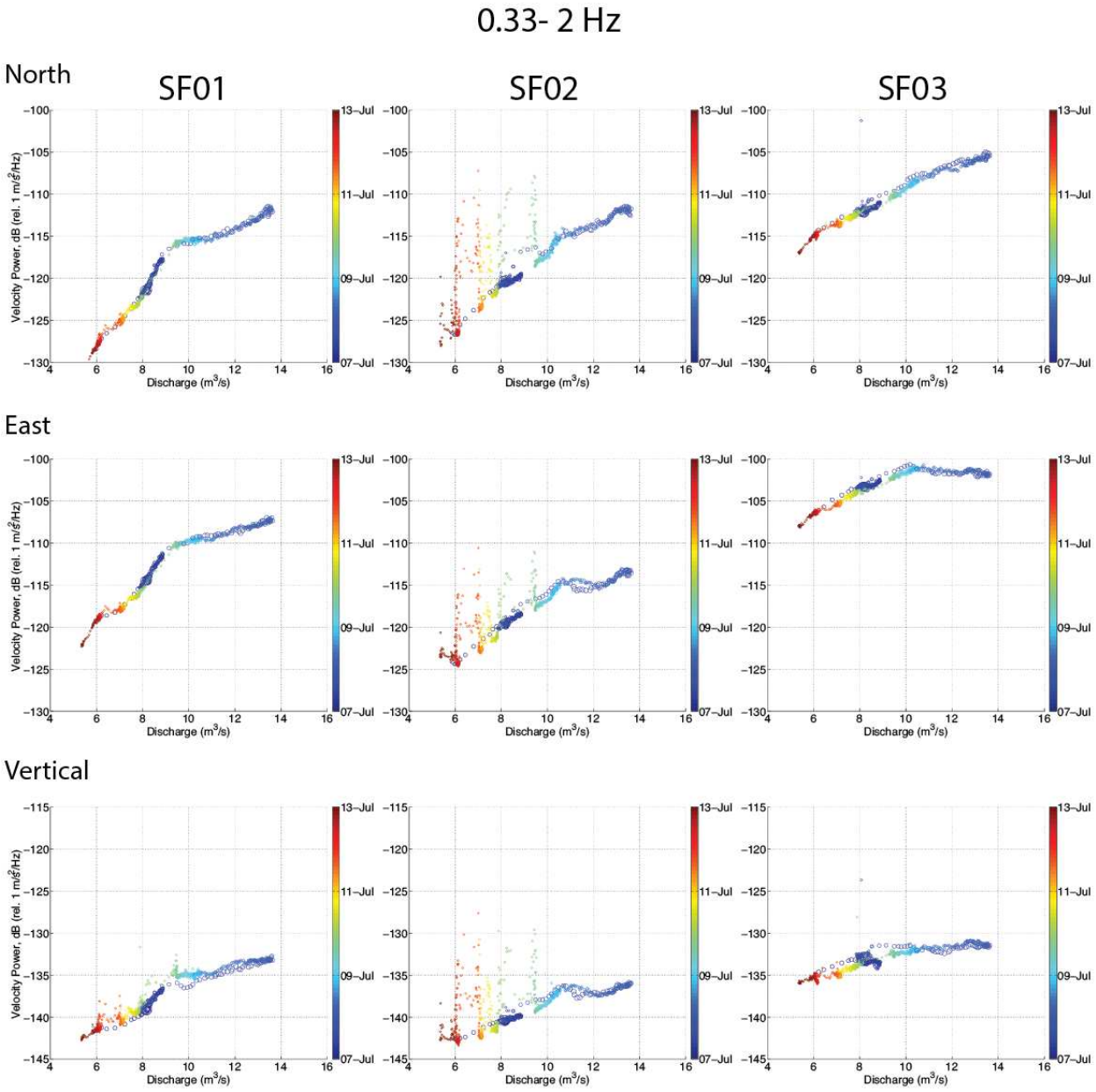

Figure 3.11. Same as Figure 3.10 except showing ground velocity versus discharge for the July rainstorm.

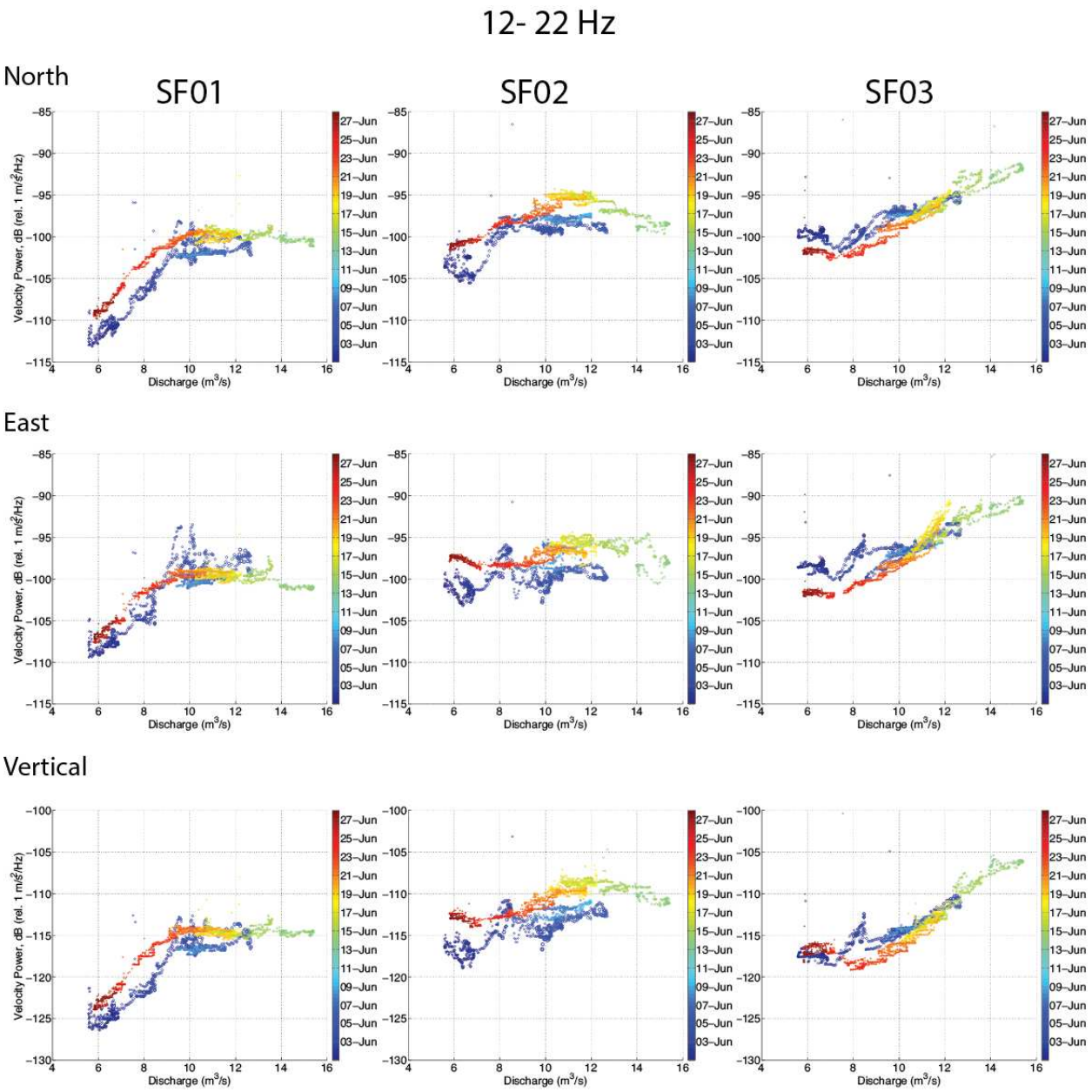

Figure 3.12. Ground velocity (dB rel. 1 (m/s^2)/Hz) from 12 to 22 Hz versus discharge for the rising and falling limbs of snowmelt runoff on all three components of each station. Plots are color coded by date.

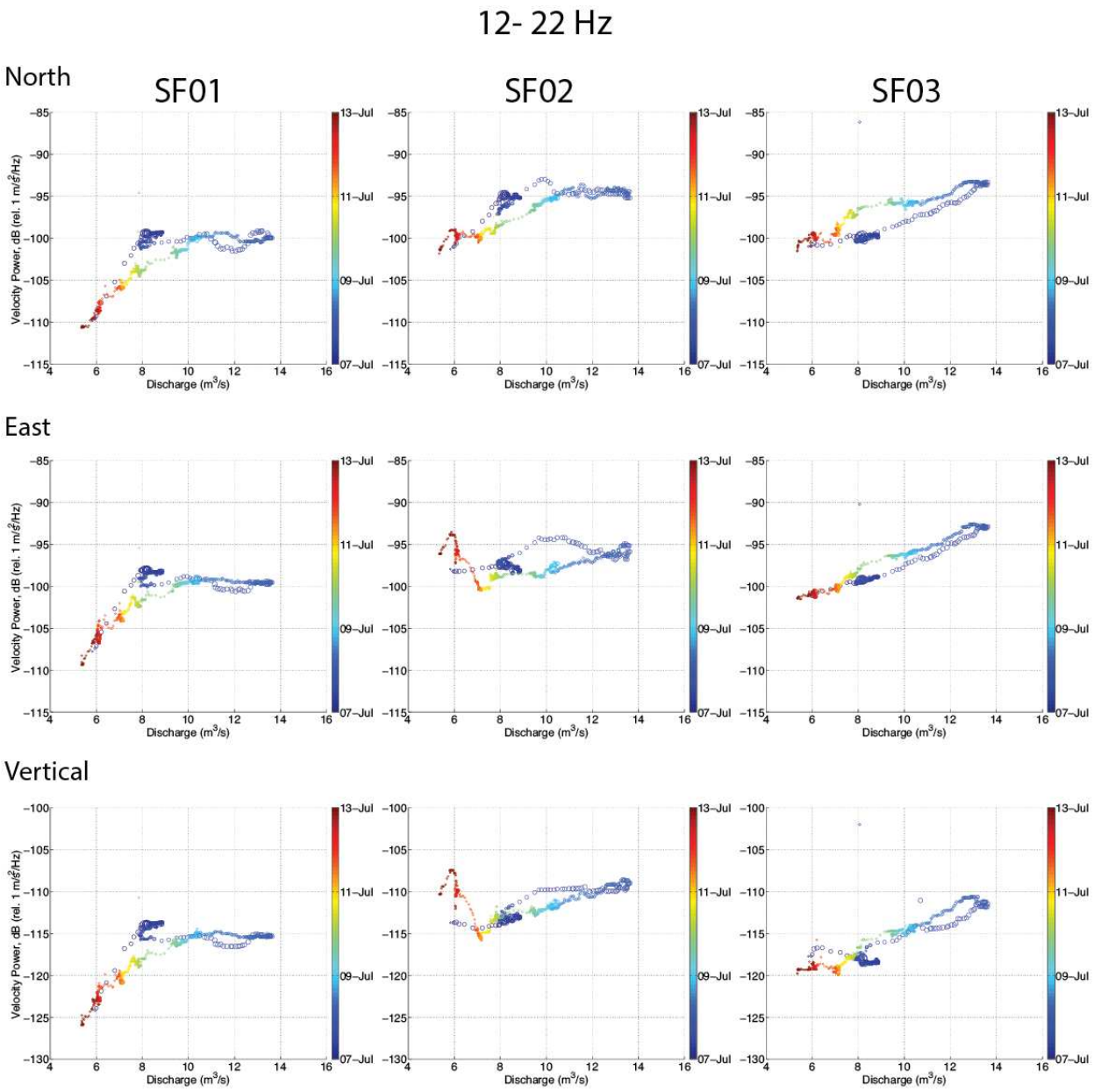

Figure 3.13. Same as Figure 3.12 except showing ground velocity versus discharge for the July rainstorm.

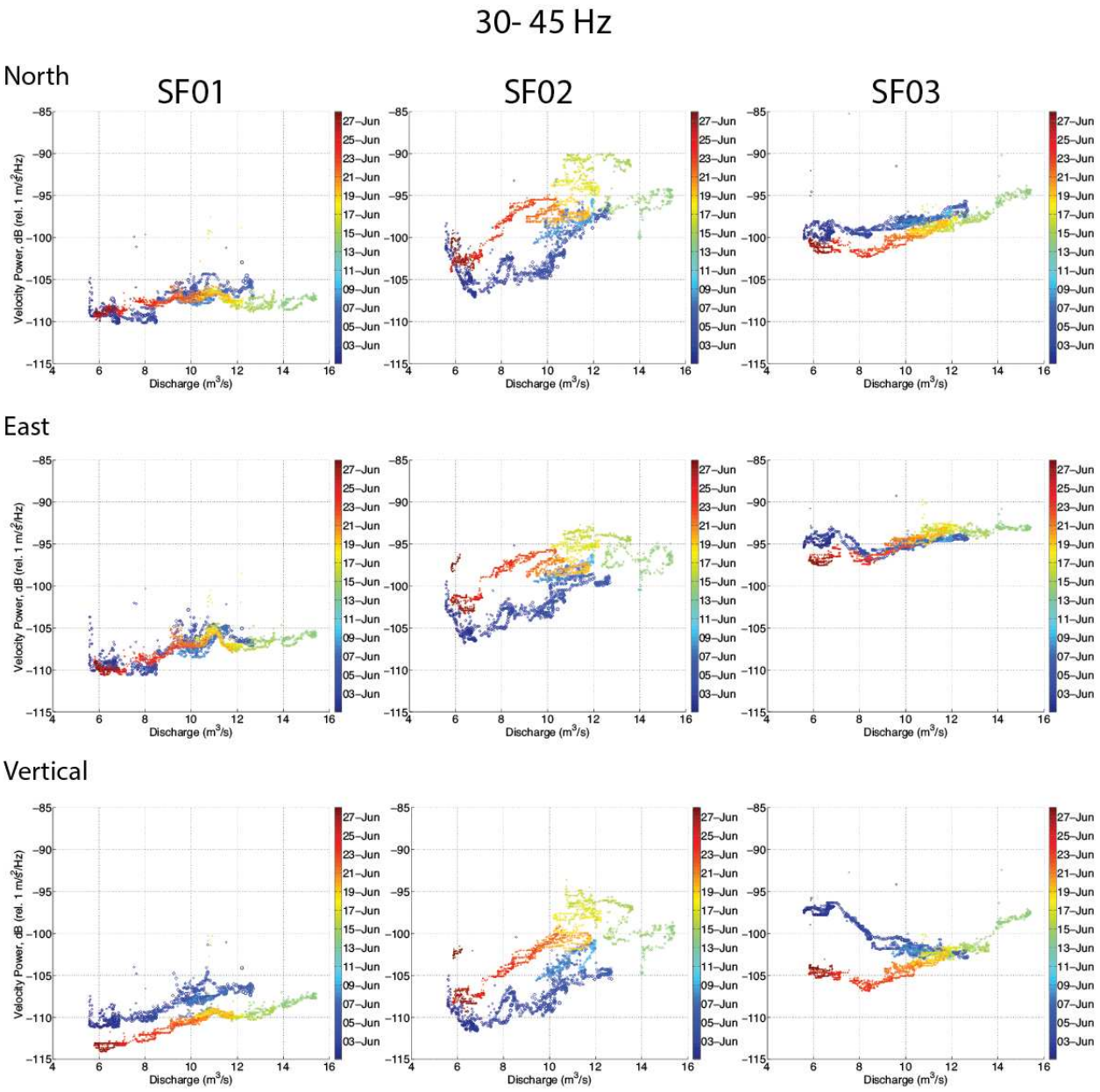

Figure 3.14. Ground velocity (dB rel. 1 (m/s^2)/Hz) from 30 to 45 Hz versus discharge for the rising and falling limbs of snowmelt runoff on all three components of each station. Plots are color coded by date.

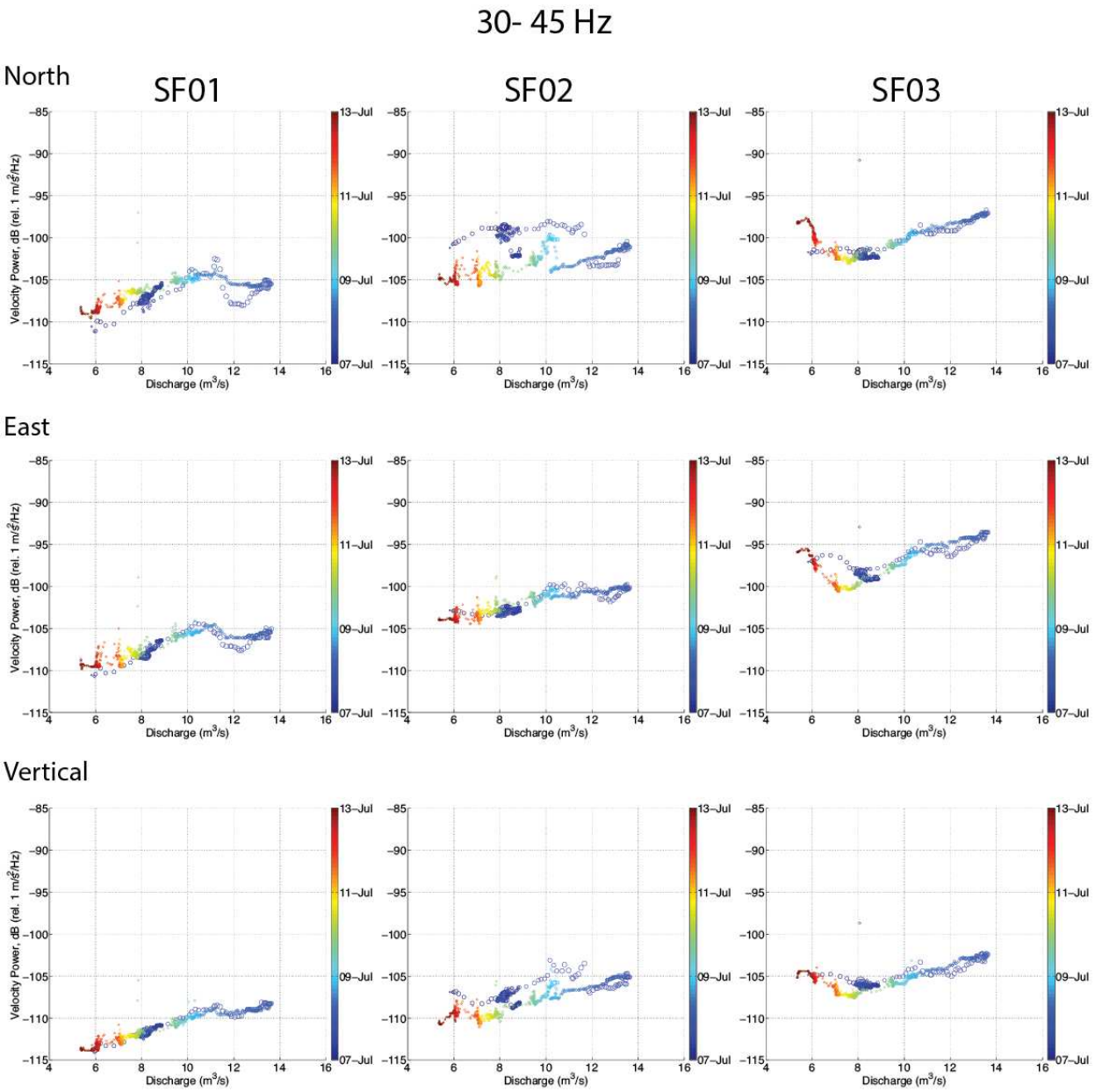

Figure 3.15. Same as Figure 3.14 except showing ground velocity versus discharge for the July rainstorm.

Seismic velocity power in the 12-22 Hz band generally increases with discharge, but does so in unique ways at each station (Figure 3.12, 3.13). At SF01, power levels on all components rise exponentially with discharge until flow reaches a given level (~10 m^3/s snowmelt runoff, ~8 m^3/s rainstorm) after which seismic power levels remain relatively constant even as discharge continues to increase. Weak CCW hysteresis occurs during snowmelt runoff and weak CW hysteresis occurs during the rainstorm event. Hysteresis is even more pronounced on SF02 and shows the same hysteresis reversal between the snowmelt runoff and rainstorm events as SF01. A reversal in hysteresis loop direction between these events is also recorded by SF03, however the sense of hysteresis for each event being opposite to that recorded on SF01 and SF02. Interestingly, horizontal component power for both components recorded at each station is consistently ~15 dB higher than the vertical component.

In the 30-45 Hz band, a 10 dB CCW hysteresis loop occurs on all components of SF02 during snowmelt runoff and contrasts with CW hysteresis seen on the vertical components of SF01 and SF03 (Figure 3.14, 3.15). Hysteresis is mild or absent in the 30-45 Hz band on all components during the rainstorm event with the exception of the north component of SF02 which exhibits general CW hysteresis and several abrupt changes in power. Unlike lower frequency 0.33-2 Hz and 12-22 Hz bands, relatively uniform levels of power are recorded on all components.

Discussion

i. Fluvial Sources of Seismic Energy

Two of the three frequency bands that appear to be excited by discharge show characteristically higher levels of seismic power on the horizontal components than the vertical. Such preferential

excitation on the horizontal components can arise from 1) source characteristics, such as predominant generation of horizontally polarized Love waves, 2) local resonance caused by siting conditions, (e.g., *Nakamura*, 1989; *Bodin and Horton*, 1999; *Bodin et al.,* 2001), and 3) instrument tilt (e.g., *Sorrels,* 1971; *Peterson,* 1993; *Wilson et al.*, 2002). Thus, understanding the enhanced horizontal power in the 0.33-2 Hz and 12-22 Hz bands may be able to provide insight into the fluvial process responsible for these signals.

Both the 0.33-2 Hz and 12-22 Hz signals are identifiable as peaks in horizontal-to-vertical ratio (H/V) spectrograms, but behave much differently under changing discharge (Figure 3.16). Peak H/V ratios in the 0.33-2 Hz band shift to lower frequencies as discharge increases and grow by over a factor of 100 as discharge rises from 2 to 15 m^3/s. We suggest that these signals result from tilt oscillations of the geophone about its vertical axis and may be generated by direct interaction with channel water in the hyporheic zone.

The hyporheic zone is defined as the space below streambeds and adjacent to stream banks where channel water and ground water mix (*White*, 1993). The transfer of water and nutrients that occurs within the hyporheic zone has been shown to be of fundamental importance to river ecology, but quantifying exchange rates has been challenging (e.g., *Boulton et al*., 1998*)*. During snowmelt runoff, strong precipitation events, and upstream dam releases, water moves from the stream to be taken up by the stream banks (e.g., *Winter*, 1998). By placing the geophone in exceptionally close proximity to the channel (~1 m) and at water table depth, it is likely directly forced by incoming bank storage water during high discharge events. If we assume that all acceleration recorded on the horizontal components is due to instrument tilt and apply first principles of the acceleration of a mass in a gravity field, then the instrument is tilting on the

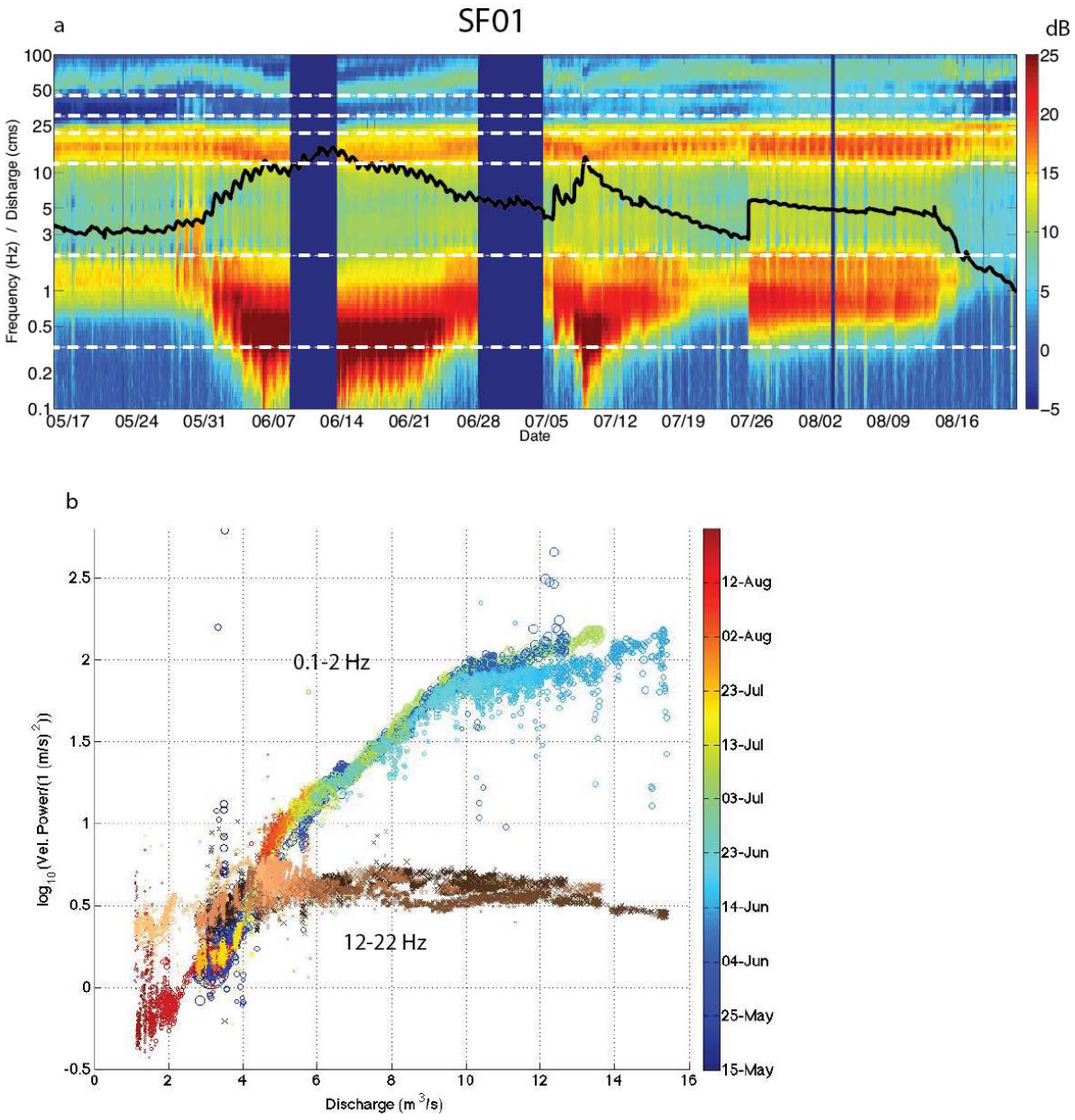

Figure 3.16. (a) Horizontal-to-vertical (H/V) ground acceleration power spectrogram at SF01 showing peaks in H/V ratios between 12-22 Hz and 0.1-2 Hz. Discharge is shown as a black curve and white horizontal dashed lines delineate the three period bands excited by discharge as described earlier in the text. (b) Velocity H/V ratios for the 12-22 Hz and 0.1-2 Hz bands plotted on a logarithmic scale versus discharge. Both bands are color coded by date and marker size indicates concentration of suspended sediment. H/V ratios in the 0.1-2 Hz band increase by over two orders of magnitude with discharge while 12-22 Hz H/V ratios remain relatively constant.

order of a few (~10 at SF03) microradians (e.g., *Wielandt and Forbriger*, 1999). Such excitation by fluid flow has some similarities to the 0.33-2 Hz tilt signal observed at exposed rock sites in the Transantarctic Mountains and interpreted to be caused by direct wind forcing on the sensor enclosure and surrounding rock (*Anthony et al*., 2015).

In contrast to the 0.33-2 Hz H/V peak, the 12-22 Hz peak remains relatively constant over a wide range of discharge conditions and persists even during minimal flow at the end of August (Figure 16). Thus, we propose that the 12-22 Hz H/V peak is not related to fluvial process and instead represents the fundamental resonance frequency of low velocity alluvium overlying higher impedance bedrock once a minimum level of fluvial excitation (e.g., above ~4 m^3/s) is present.

In a simple two-layer system, where a higher seismic impedance substrate is overlain by low impedance sediments, the fundamental seismic resonance frequency, f_r, is related to the sediment layer thickness, *Z*, by:

$$f_s = V_s/4Z,$$

where V_s is the average-shear wave velocity in the sediment layer (e.g., *Ibs-von Seht and Wohlenberg*, 1999). The fundamental frequency can be determined from peaks in the H/V ratio of ambient seismic noise (*Nakamura*, 1989). Assuming a near-surface alluvium shear wave velocity of 300 m/s (consistent with Holocene fine-grained sediment; e.g., *Williams et al*., 1998), the 12-22 Hz H/V peak corresponds to a reasonable sediment thicknesses of ~3.0-6.2 m in our study area.

Although the 12-22 Hz H/V amplitude peak remains relatively constant over time, power in the band varies strongly with discharge and shows complex patterns of hysteresis during snowmelt runoff and during the rainstorm. The two fluvial processes thought to generate seismic nose in previous studies (e.g., *Burtin et al*., 2008, 2011, 2016; *Hsu et al.*, 2011; *Schmandt et al.*, 2013; *Bartholomaus et al.,*2015) are turbulent flow and bed-load transport. Recent modeling has suggested that seismic power induced by turbulent flow scales with discharge, Q, as $Q^{7/5}$ (*Gimbert et al.*, 2016). Even though this relation is based on seismographs recording at distances from the river much greater than the river width (*Gimbert et al*., 2014) it decently fits our observations of changing 12-22 Hz power with discharge, predicting variations in horizontal power levels by ~4.1 dB and vertical power by 6.5 dB with 95% confidence (Figure 3.17). However, strong discrepancies exist on the vertical component, which, combined with hysteresis following both snowmelt runoff and rainstorm events initially suggests that signal generated by bed-load transport could be contributing to power recorded in the 12-22 Hz band.

Distinguishing turbulent flow from bed-load transport through spectral analysis generally requires multiple measurements at different distances from the river (*Gimbert et al*., 2014). As the seismic instruments are placed further away from the channel, higher frequencies signals become more attenuated and turbulent flow dominates lower frequency bands. As our sensors were placed in exceptionally close proximity to the channel, attenuation is minimal and both turbulent flow and bed-load transport signals likely contribute to the 12-22 Hz band. However, neither the 12-22 Hz or 30-45 Hz band at any sensor show hysteresis patterns similar to those observed for suspended sediment concentrations, particularly the diurnal hysteresis loops seen on

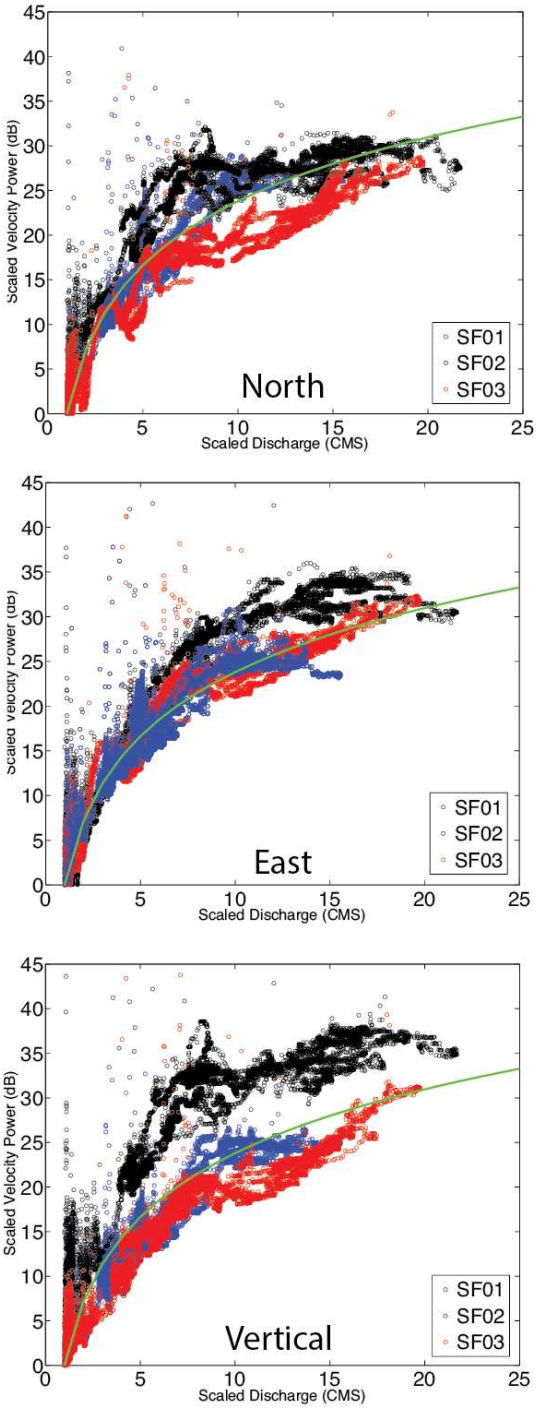

Figure 3.17. 12-22 Hz velocity power for the three components of each station versus discharge. Both velocity and discharge measurements have been scaled by values attained during late August when discharge was minimal (~ 1 m^3/s). The green curve shows the data fit with the *Gimbert et al*. (2016) relation in which seismic velocity power generated by turbulent flow (no bed-load transport) scales with discharge, Q, as $Q^{7/5}$.

the rising limb of snowmelt runoff. Thus, it is unlikely that seismic monitoring of fluvial systems will be able to characterize variations in fine-grained suspended sediment.

The opposite sense of 12-22 Hz and 30-45 Hz hysteresis recorded during the same discharge events on geophones separated by only several meters indicates asymmetric rising/falling limb influences and conditions. These must represent near-sensor site changes between the rising and falling limb of the event that could include localized changes in stream shape, bottom topography or roughness, hyporheic flow, or vegetative seismic coupling. Our observations validate the importance of making multiple measurements at different distances from the channel to avoid reaching possibly unwarranted interpretations. We recommend, given the wider availability of large numbers of high frequency seismographs (e.g., *Schmandt and Clayton*, 2013), that future research in this area incorporate high frequency seismic arrays, which would allow for much better quantification and interpretation of local high-frequency effects, and calibration of seismic measurements with stream properties and variable siting conditions.

ii. Synthetic Hydrograph from Seismic Observations

As velocity power in the 0.33-2 Hz band recorded on horizontal components follows smooth, nearly exponential relations with flow rates, we investigate the potential of mapping seismic power in this band to hydraulic discharge to create a synthetic hydrograph. Since this signal is suspected to arise through instrument tilt caused by direct forcing with channel or hyporehic flow, the response to discharge varies appreciably between individual sensor sites (Figure 3.10, 3.11), and may be sensitive to local effects such as streamside vegetation (including root structures), soil permeability, and channel geometry. SF03 in particular was located within dense

rooted (willow) vegetation which may have coupled with stream flow uniquely at this site, and thus may explain heightened sensitivity to discharge in this band as well as its differing hysteresis characteristics (e.g., Figures 3.1 and 3.7). We thus calibrate 0.33-2 Hz power recorded on each channel of stations SF01 and SF03 to discharge during a 2-week period surrounding the rainstorm event and apply these relations to generate a synthetic hydrograph spanning the entire seismic record. We do not use station SF02 in this analysis as power in the 0.33-2 Hz band at this station is strongly influenced by wind gusts as described previously.

Seismic velocity power in the 0.33-2 Hz band scales roughly exponentially with discharge and becomes a linear relationship when seismic power is expressed in dB. This enables us to use standard least-squares linear regression techniques to fit a bilinear relationship between 0.33-2 Hz seismic power (expressed in dB) and discharge during the calibration period (Figure 3.18). A bilinear regression was determined to be the best approach, as both stations observe a drastic reduction in sensitivity to discharge once a critical threshold is reached (~9 m^3/s at SF01 and ~6 m^3/s at SF03). At lower discharge rates, sensitivity between the four horizontal channels varied from 3.88-4.65 dB/m^3/s and dropped to 0.84-1.26 dB/m^3/s when flow exceeded the threshold. The exact mechanism for the change in sensitivity is not understood, but it may represent when the water table completely covers the geophone and additional rises in stage height do not increase the cross-sectional area of the sensor experiencing forcing from channel or hyporheic flow.

With the bilinear transfer functions determined, we generate synthetic hydrographs over the full seismic record for each horizontal channel. To minimize the effect of transient, non-fluvial noise

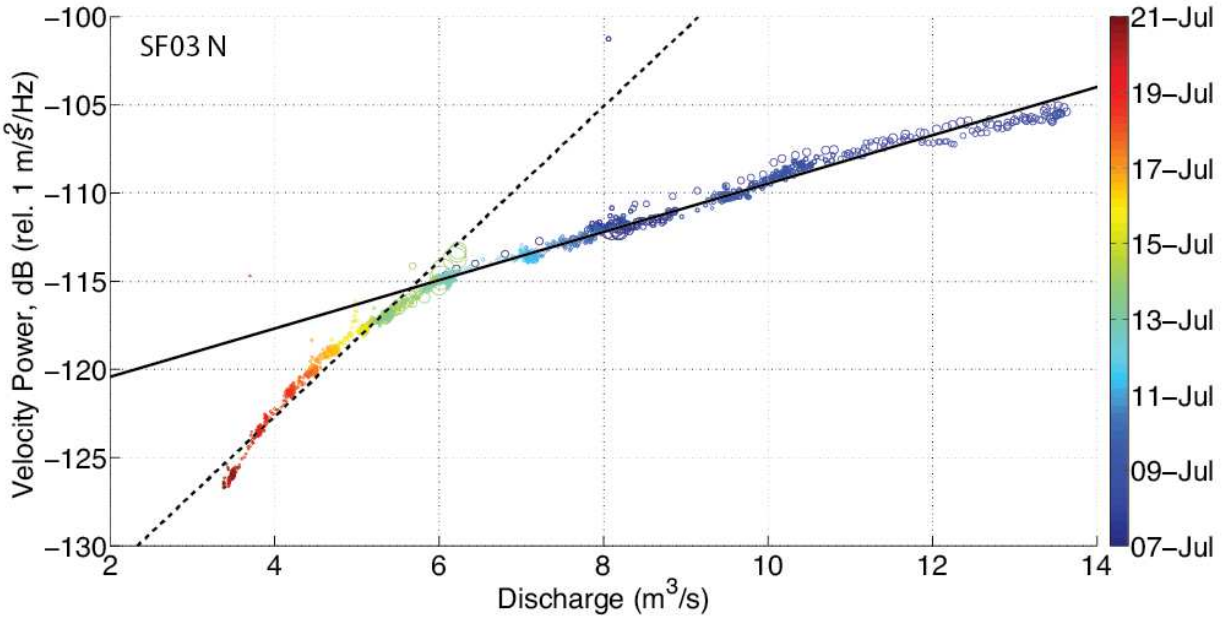

Figure 3.18. An example of the bilinear least squares regression used to calibrate integrated 0.33-2 Hz horizontal component ground velocity power to discharge over a 2-week interval surrounding the July rainstorm event. The plot is color coded by date and shows data recorded on the north component of SF03. The dashed (solid) black line is a linear regression fit to velocity power when discharge is less (more) than 6 m^3/s.

sources, discharge estimates were smoothed using a 1-hour (6 sample) moving median filter. Visual inspection of the synthetic hydrographs shows that nearly all variations in discharge, including diurnal cycles, can be determined from 0.33-2 Hz horizontal component seismic data (Figure 3.19). Correlations coefficients for the four channels between synthetic discharge and discharge determined from pressure transducer readings range from 0.96-0.99 and agree to within ~1 m^3/s at the 95% confidence interval. We note that pressure transducer and rating curve hydrographic estimates also contain substantial uncertainty for streams of this size that can easily, between background and flood stage flows, exceed the discrepancy between our seismically determined estimate and the available gauge estimate (e.g., *Benson and Dalrymple*, 1967). The largest misfits generally occur during late August when discharge levels become low enough that fluvial signals no longer exceed background noise levels. We suggest that during these times, the water table has become low enough that the geophone is no longer directly interacting with water flow. Despite this difficulty in retrieving discharge during low flow conditions, our results indicate that not only is the 0.33-2 Hz signal generated from fluid flow, but that it can be used to determine discharge rates with a reasonably high degree of accuracy in moderate flow conditions.

Conclusions

We have demonstrated that, by placing seismic instruments within close proximity to a small fluvial system, a wide frequency range of seismic signals including, < 1 Hz signals, interpreted as seismometer tilt, are recorded. Increases in >10 Hz seismic power, which correlated with changes in discharge, occurred in two distinct bands and exhibited complex (both CW and CCW) hysteresis patterns that can vary between instruments that only 10s of meters apert. No

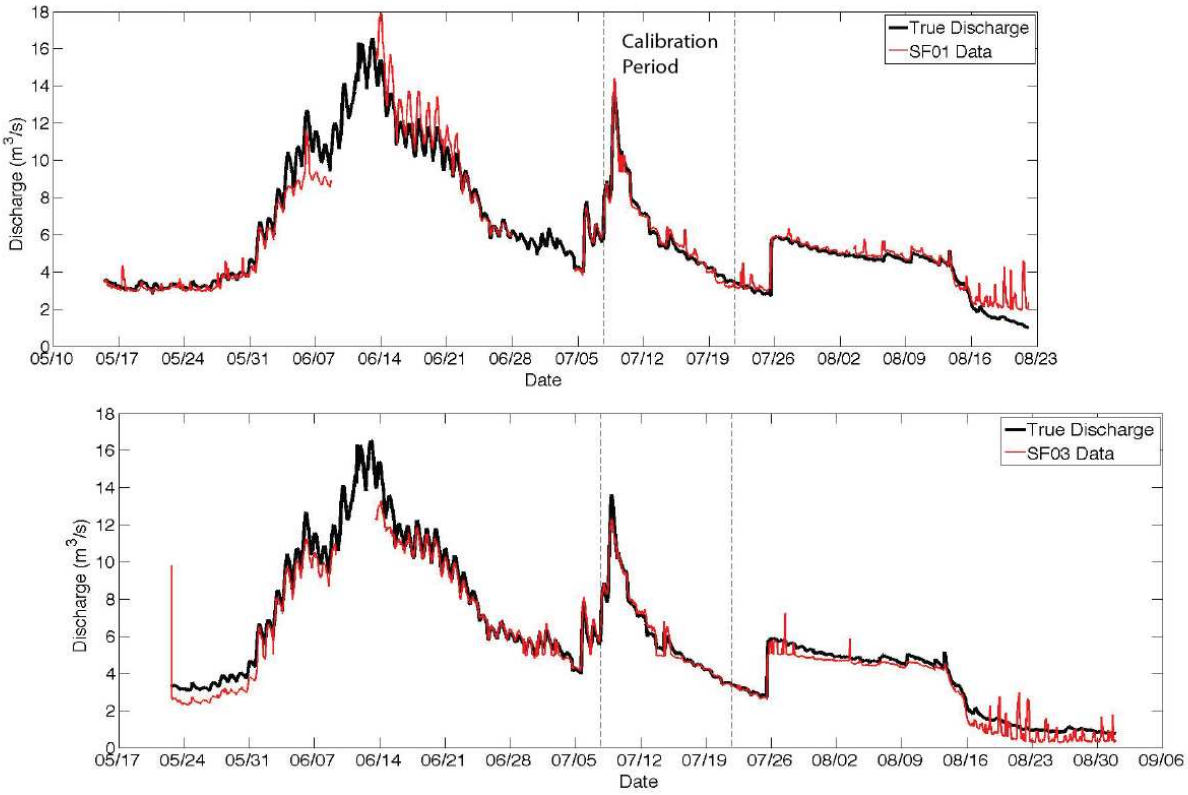

Figure 3.19. Synthetic hydrographs (red curves) calculated from 0.33-2 Hz horizontal component ground velocity power show excellent agreement with discharge estimates attained through traditional methods (i.e., pressure transducer and rating curves). The dashed black horizontal lines indicate the 2-week period around the rainstorm event where seismic data was calibrated against discharge as illustrated in Figure 3.18.

hysteresis or seismic spectral observations were found that consistently correlated with simultaneously recorded (fine) suspended sediment measurements.

However, these near-channel seismic instruments uniquely record power below 1 Hz that is exponentially sensitive to discharge. As variations in these low-frequency signals are much stronger on the horizontal components, we propose that they arise through tilting of the sensor as it is forced by channel and possibly correlated hyporheic flow. After calibrating horizontal seismic power with flow rates over the course of a rainstorm event for individual sensors, we show that 0.33-2 Hz signals can be used to accurately invert for fluvial discharge. Thus, the installation of near-channel seismometers has the ability to usefully augment seismic networks aimed at monitoring fluvial processes by providing novel signals not observed at greater distances. Estimates of discharge attained outside the channel may be especially useful over the course of high flow events when pressure transducers and other equipment placed within the channel may be destroyed.

Chapter 4: Epilogue and Future Directions

The results presented in this dissertation have demonstrated several applications of spectral analysis on continuous seismic records to assess instrumentation performance and data quality, infer near-surface structure, and characterize environmental sources of seismic signals across a broad range of frequencies. The emerging field of environmental seismology has opened up new avenues for interdisciplinary collaboration between seismologists and a broad range of earth scientists including geomorphologists, glaciologists, hydrologists, oceanographers, volcanologists, geotechnical engineers, and atmospheric scientists to investigate oceanic, atmospheric, and surface processes. Several key findings from the dissertation should usefully contribute to future environmental seismology studies, particularly 1) the insights into ocean wave-sea ice interactions and their effect on microseism signals (Chapters 1 and 2), 2) confirmation of the ability of primary microseisms, but not secondary microseisms to cross ocean basins (Chapter 2), 3) characterization of the influence the Southern Annular Mode has on Drake Passage storm activity (Chapter 2), and 4) the discovery of low-frequency signals on near-channel seismic stations that can be used to accurately invert for discharge rates in fluvial systems (Chapter 3). Additionally, limitations in current spectral analysis software (PQLX) found during the course of dissertation work drove the development of the Incorporated Research Institutions for Seismology (IRIS) Noise Toolkit (NTK). The NTK software package provides a user-friendly interface for the computation of power spectral density (PSD) estimates directly from the IRIS Data Management Center (DMC) archives. Here, I briefly highlight some further applications of utilizing spectral analysis of seismic noise to study environmental processes and improve seismic network design.

Changes in Global Wave State and Extremal Storm Activity

Recent studies of both in situ and reanalysis wind data (e.g., *Tokinaga and Xie*, 2011; *Young et al.*, 2011) have suggested that global wind speeds have increased over the past 50-60 years by 0.06-0.20 m/s per decade. Since oceanic waves are generated through ocean-wind interactions, this trend has the potential to influence wave state across the globe and could have drastic societal (e.g., shipping routes, coastal erosion and flooding) and climate (evaporation rates, cryospheric stability) implications. As microseism observations are predominantly sensitive to near-shore wave state (e.g., *Bromirski and Duennebier*, 2002), the use of historical microseism records has been suggested for use in monitoring decadal-scale changes in coastal wave activity (*Aster et al*., 2008; 2010; *Stutzmann et al*., 2009).

The *Aster et al.* (2010) study developed the index-hour methodology (See methods section of Chapter 2) of identifying extreme storm events during winter months from the microseism record at long-running Global Seismic Network (GSN) stations. The study found generally increasing trends of strong storm events in the northern hemisphere and decreasing trends in the southern hemisphere, although reliable southern hemisphere seismic records were extremely limited. Additionally, it was found that northern hemisphere storm events appear to drastically increase during El Niño years. Subsequent spectral analysis performed using PQLX on an expanded set of global stations found increasing trends in both overall primary microseism power and extremal storm events in the northeast Atlantic and southwest Pacific oceans between 1994-2012 (Figure E.1; *Anthony et al*., 2013). These results are generally consistent with satellite observations of changes in significant wave height between 1985-2008 (*Young et al*., 2011).

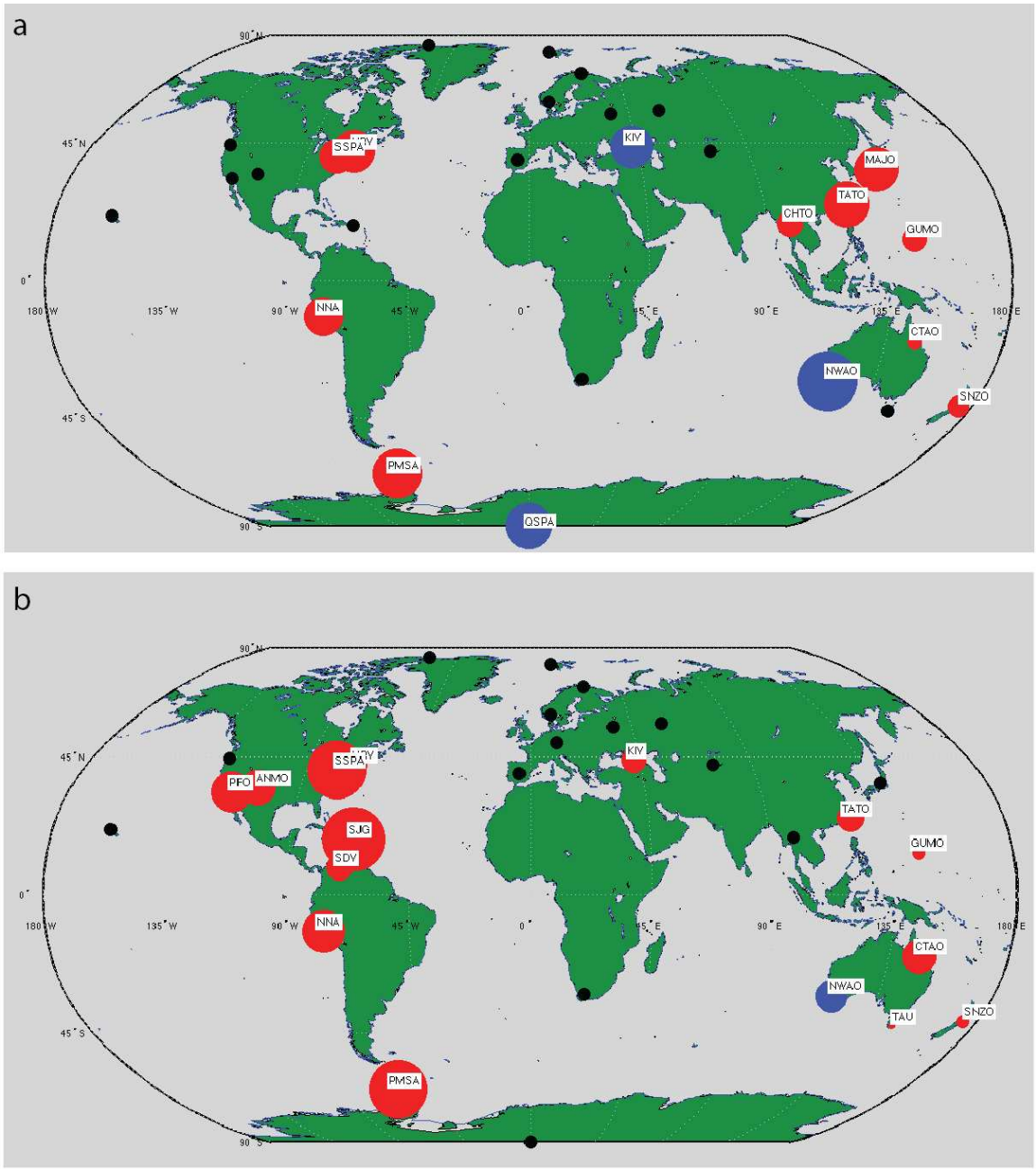

Figure E.1. Primary and microseism trends in power (top) and index hours (bottom) expressed in percent per year for global seismographic stations (1994-2012). Red circles indicate statistically significant increasing trends, blue circles represent decreasing trends, and black dots are stations that show no statistically significant trends (i.e., the uncertainty in the slope measurement is greater than the absolute value of the slope). The radii of the red and blue circles represent the amplitude of the trends after subtracting out uncertainty. After *Anthony et al.*, 2013.

Perhaps the fundamental driver behind development of the NTK was that PSD estimates produced in PQLX tended to be over-smoothed with the consequence that secondary microseism energy was undesirably smeared into the primary microseism band. As the primary microseism is thought to be the most robust indicator of identifying changes in wave-state (e.g., *Aster et al*., 2010; *Anthony et al*., 2013), the need arose for a software package that would allow for reduced smoothing of spectral estimates. Work is currently underway to utilize the higher resolution PSDs generated by the IRIS NTK to update global microseism metrics though 2016, which will include analysis of the major 2014-2016 El Niño event. Additional processing will be applied to southern hemisphere microseism records to search for evidence of the recently identified Baroclinic Annular Mode (BAM), which has been shown to modulate southern hemisphere storm activity over 20-30 day periods (*Thompson and Woodworth*, 2014).

Possible Role of Oceanic Wave Forcing in Antarctic Peninsula Ice Shelf Collapse Events

The prevalent theory for the mechanism behind recent ice shelf collapse events on the Antarctica Peninsula has been crevasse propagation following the ponding of surface meltwater (e.g., *Scambos et al*., 2000). Anomalously high surface temperatures on the eastern half of the Antarctic Peninsula driven by positive phases of the Southern Annular Mode (SAM) likely enabled melt pond formation and are correlated with both Larsen A (January 1995) and Larsen B (March 2002) ice shelf collapse events (*Marshall et al.*, 2006). Positive phases of the SAM during the austral summer are also associated with reduced sea ice around the Antarctic Peninsula as a low-pressure anomaly forms to the west of the Bellingshausen Sea and allows the transport of warm air masses poleward (*Lefebvre et al.,* 2004; *Liu et al*., 2004). After showing that strong storm events in the Drake Passage tended to occur during positive phases of the SAM

and that sea ice appears to dampen ocean waves, I concluded Chapter 2 by posing the question "could ocean wave forcing contribute to ice shelf collapse events on the Antarctic Peninsula?"

From 23 October 1994 to 25 January 1995, satellite observations show that the Larsen A ice shelf retreated 3 km, followed by a rapid 2 km retreat between 25-28 January (*Rott et al*.,1996). Between satellite passes on 28 January and 30 January, ~600 km^2 of the ice shelf collapsed, followed by an additional ~750 km^2 by 22 March. *Rott et al*. (1996) infer that forcing from unusually high surface winds during 23-26 January on the ice shelf initiated the collapse. I use the seismic record at PMSA to show that two large pulses of locally-generated ocean swell struck the region between 25 and 29 January (Figure E.2). These wave events show exceptional temporal correlation with the timing of ice shelf retreat and breakup. I plan to further investigate the hypothesis that these swell packets, aided by high surface temperatures and reduced sea ice conditions, played a substantial role in triggering the rapid disintegration of the Larsen A ice shelf after melt ponding had already taken place. Future work will include similar analysis of microseism records surrounding the Larsen B and Wilkins Ice Shelf collapse events.

Short-Period Microseism Generation in Lakes and Polynyas

Many seismic stations across the globe have fairly stable noise levels between the secondary microseism noise peak and short period (< 1 s) noise contamination (e.g., Figure 1.2). Perhaps not coincidently, many earthquake studies utilize this "noise hole" between approximately 0.5-5 s period to perform teleseismic body wave analysis, including preliminary detections of epicenters (PDEs) and magnitudes using P-waves (e.g., *Engdahl and Gunst,* 1966; *Molnar et*

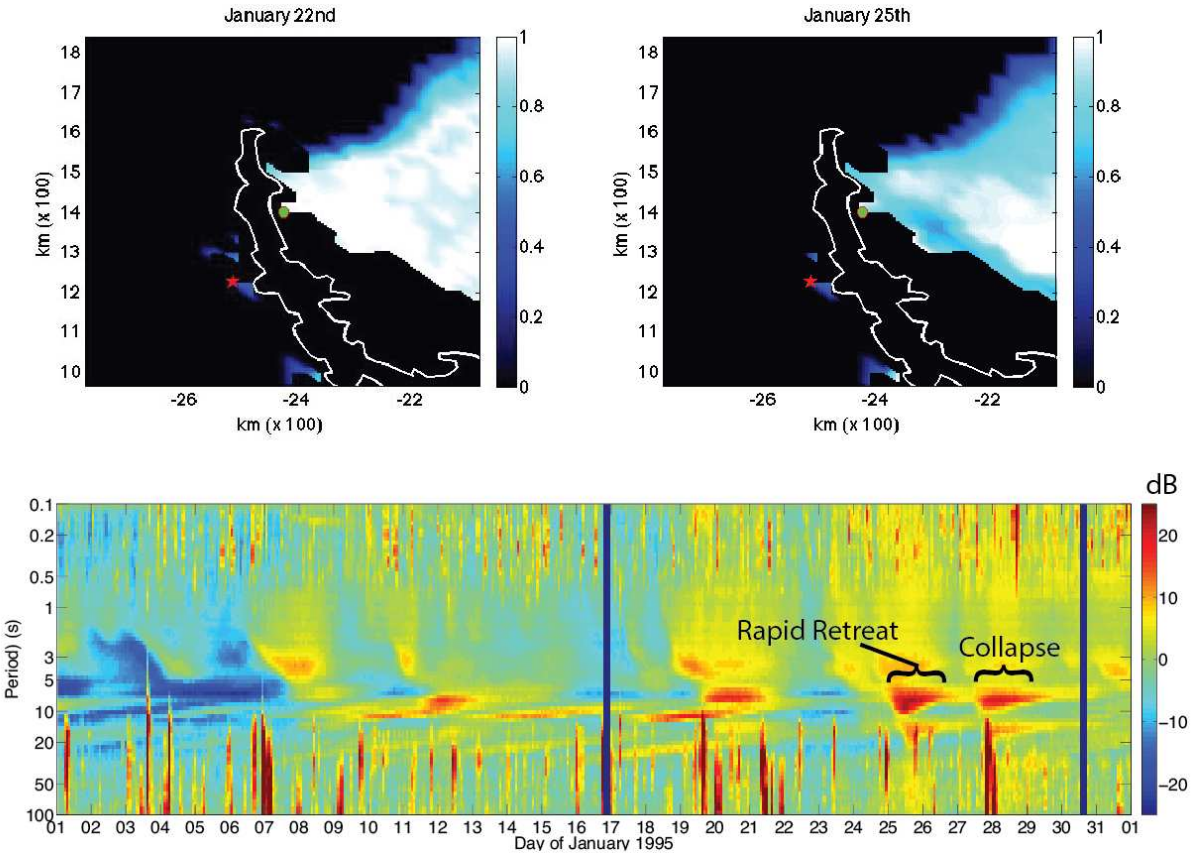

Figure E.2. (top) Sea Ice concentration around the Larsen A Ice Shelf (green dot) in the Weddell Sea in the days prior to collapse. (bottom) Vertical ground acceleration differential spectrogram for the month of January 1995 recorded at Palmer Station, Antarctica (red star in sea ice concentration maps). The differential spectrogram is created by subtracting the median Power Spectral Density estimate (PSD) for the full month from every 3-hour, 50% overlap PSD (dB rel. 1 $m^2/s^4/Hz$). Rises in 5-10 s power (secondary microseism) of >20 dB and 10-20 s power (primary microseism) of >10 dB occur on the 25th and 28th of January and are interpreted to indicate strong wave activity during the passage of two large storm systems. Lack of dispersion in the spectrogram suggests that the storms are of local origin, which agrees with Antarctic Peninsula wind speed records. These storm events coincide with phases of rapid retreat and collapse of the Larsen A ice shelf as identified through satellite imagery (*Rott et al*., 1996) and suggest that oceanic wave forcing may have contributed to the collapse of the ice shelf.

al.,1973). However, I have identified several stations where high noise levels enter this band, likely due to the generation of short-period microseism noise generated in large bodies of water during high winds (e.g., lakes, bays, oceans; Figure E.3). Noise levels at these stations may mask and interfere with earthquake detection and analysis.

During the summer of 2016, I installed two broadband seismometers on the shorelines of Lake Pontchartrain, Louisiana, a suspected source of short-period microseism noise (Figure E.3). Spectral analysis of seismic noise from these stations combined with mid-lake wind speed data and 1-hour interval imagery of the lake surface should facilitate new insights into short-period microseism generation. Quantifying the contributions of this noise source and its attenuation properties has direct implications for the design of seismic networks aimed at monitoring local and regional seismicity.

In an extreme example of short-period microseism noise, I use seismic stations located on the Ross Ice Shelf of Antarctica to track the opening of a large polynya and local wind speeds in front of the ice shelf (figure E.4). When the polynya opens up during the summer months (December-March), ground acceleration noise between 0.3-3 s period jumps 20-30 dB (rel. 1 $m^2/s^4/Hz$), dropping the mean signal-to-noise ratio of large ($>M_W$ 5.5) earthquakes to 0 dB (*Baker et al.*, 2016). Although this signal is a hindrance to seismic imaging studies using teleseismic body-waves, it shows promise for tracking near-coastal sea ice conditions.

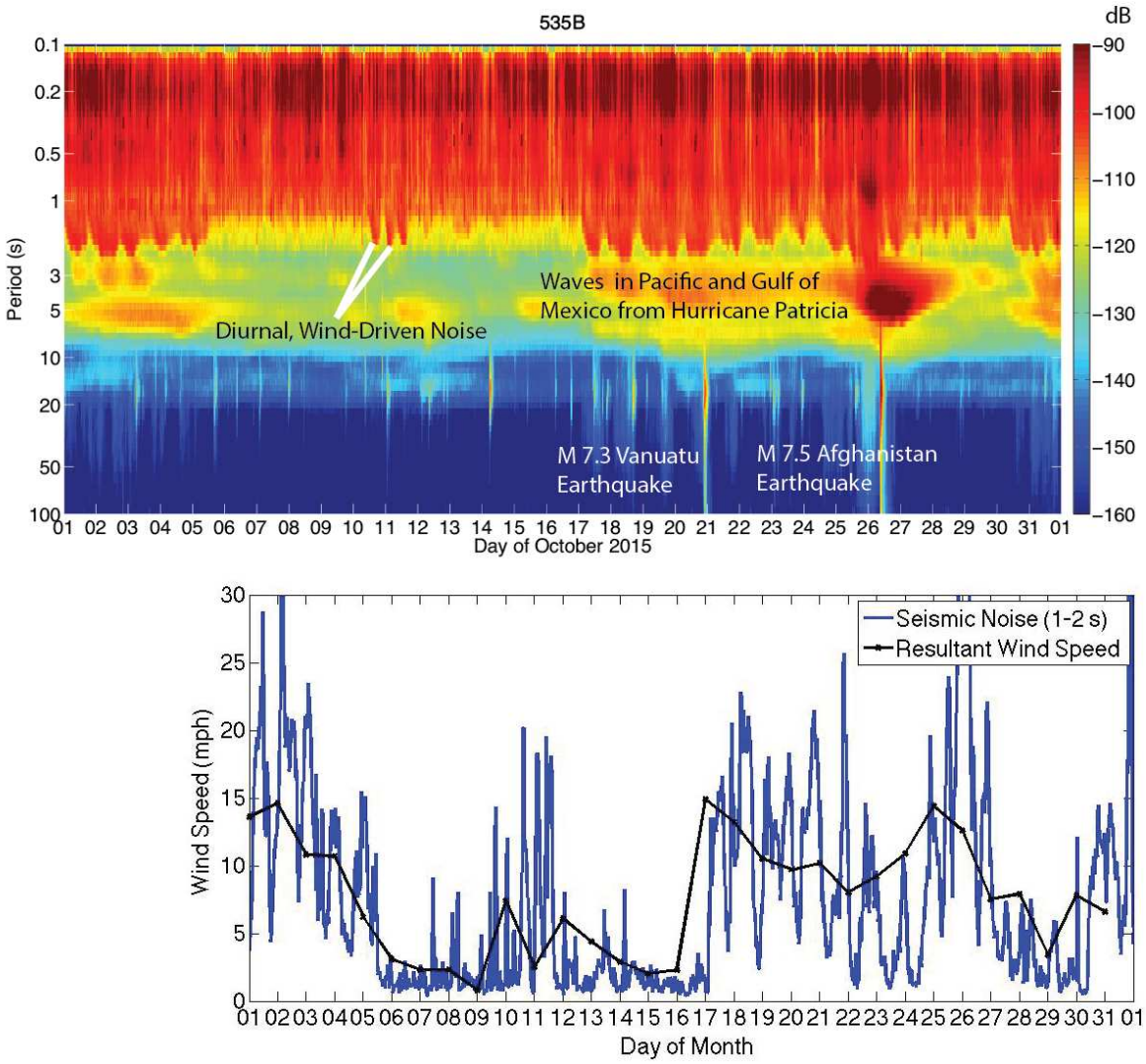

Figure E.3. (top) Vertical acceleration spectrogram for station 535B, Louisiana for the month of October, 2015. Station 535B is located ~10 km west of Lake Pontchartrain (~40 km diameter) and has an unusual diurnal signals between 1-2 s period that appears to be correlated with wind speed (bottom panel). This signal may to be generated by wind-driven waves within the shallow (~20 ft deep) lake. Hurricane Patricia passes into the Gulf of Mexico on October 26th, and the waves formed in the Gulf raise power between 3-5 s period by >20 dB. Large earthquakes are also shown here and appear in the spectrogram as vertical spikes between ~5-100 s period.

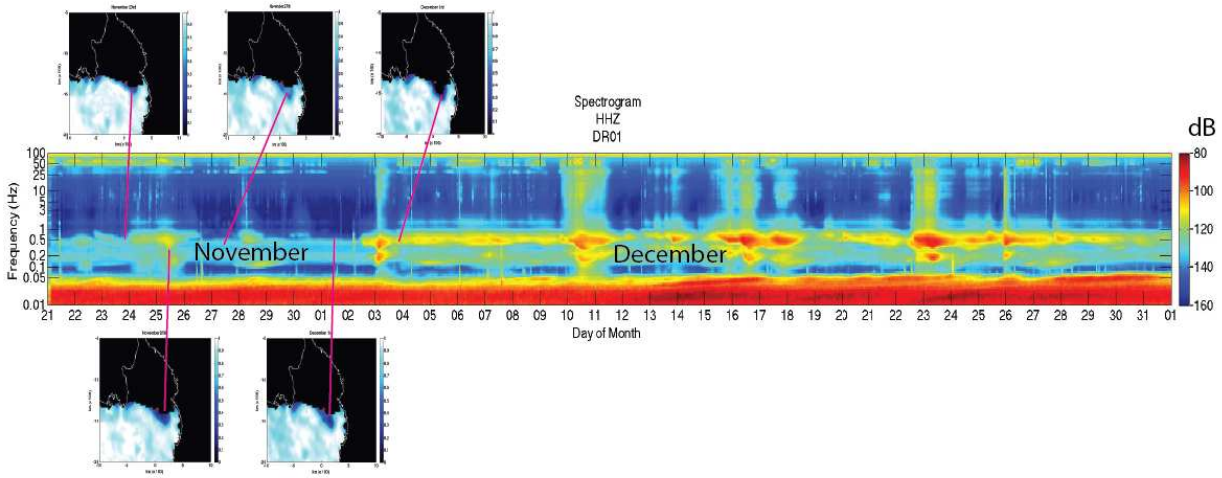

Figure E.4. Acceleration vertical component spectrogram of DR01 (Ross Ice Shelf, Antartica; red star) for late November and December of 2014. Acceleration power between ~1-3 s period increases drastically following the December 3rd opening of an annually occurring polynya in front of the ice shelf. Noise in this period band is likely excited due to the generation of wind waves in the open water with particularly strong events correlating to known strong wind events.

Seismometer Emplacement Techniques to Mitigate Noise

In the conclusion of Chapter 1, I recommended that Antarctic seismic stations emplaced directly on rock be moved to shallow snow in order to mitigate noise induced by sensor tilt. I pointed to station MILR as an example of a rock site that had exceptionally high levels of noise, particularly on the horizontal components. Upon my recommendation, MILR was moved into shallow snow in early 2014. After retrieval of data during the 2015 field season, this enabled a direct comparison of noise levels at a windy rock site and a nearby (< 20 m) shallow snow vault.

Reducing the station wind profile by moving it off the rock outcrop reduced short-period noise levels by up to 15 dB on the vertical components and by 20 dB on the horizontal components (Figure E.5). A reduction in noise of at least 10 dB at all periods between 0.1-100 s is observed on the horizontal components and suggests that reducing wind profiles and moving station away from strong wind-coupled sources can drastically reduce wind noise as well as sensor tilt. Utilizing spectral analysis to quantify reductions in noise levels attained through a variety of sensor emplacement techniques should facilitate improvements in the design of both temporary and permanent seismic networks and will be the main component of my recently funded United States Geological Survey Mendenhall Research Fellowship.

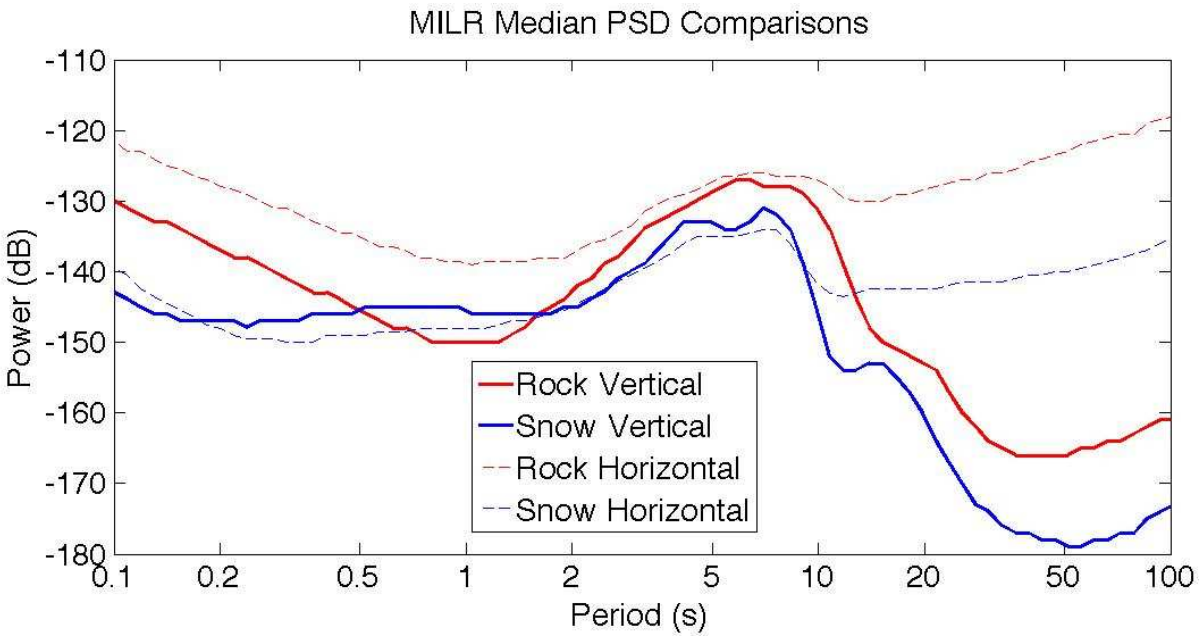

Figure E.5. Median acceleration PSDs for vertical (solid lines) and horizontal components (dashed lines) at MILR station, Antarctica for when the station was emplaced directly on rock (2008-2013 data analyzed) and after it was moved to a shallow snow vault (2014-2015).

References

Accardo, N., Wiens, D., Hernandez, S., Aster, R., Nyblade, A., Huerta, A., Anandakrishnan, S., Wilson, T., Heeszel, D., Upper mantle seismic anisotropy beneath the West Antarctic Rift System and surrounding region from shear wave splitting analysis, *Geophysics Journal International* **198***,* 414-429*,* 2014.

Adams, P. N., C. D. Storlazzi, and R. S. Anderson (2005), Nearshore wave-induced cyclical flexing of sea cliffs*, Journal of Geophysical Research,* **110**, F02002.

Albert, D.G (1997). Seismic noise propagation in firn at the South Pole, Antarctica, US Army Cold Regions Research and Engineering Laboratory, Contract report.

Aleqabi, G., Euler, G., Wiens, D., Wysession, M., van der Lee, S., Revenaugh, J., Frederiksen, A., Darbyshire, F., Stein, S., and D. Jurdy (2013). Array Analysis of Lake Superior Microseisms, Abstract: 2013 EarthScope National Meeting.

Anderson, K., Butler, R., Aster, R., Comparison of Antarctic seismic station quality performance to aggregate GSN network power spectral density probability density functions, Annual Meeting of the Seismological Society of America, Santa Fe, NM, *Seism. Res. Lett*., 79(2), 2008.

Anthony, R.E., R.C. Aster, D.A. Wiens, A. Nyblade, and C.A. Rowe (2011), Seismic noise levels across Antarctica, AGU Fall Meeting Abstracts, 2204.

Anthony, R.E., R.C. Aster, and C.A. Rowe (2013), Global Trends in Ocean Wave State and Extremal Storm Events Examined with Microseism Analysis, *AGU Fall Meeting Abstracts*, 2310.

Anthony, R.E., R.C. Aster, C.A. Rowe, and D.A. Wiens (2014), Effects of Seasonal and Secular changes in Antarctic Sea Ice on Microseismic Noise, *AGU Fall Meeting Abstracts*, 07.

Anthony, R.E., R.C. Aster, D. Wiens, A. Nyblade, S. Anandakrishnan, A. Huerta, J.P. Winberry, T. Wilson, and C. Rowe (2015), The seismic noise environment of Antarctica, *Seismological Research Letters* **86**, 1, 89-100.

Ardhuin, F., E. Stutzmann, M. Schimmel, and A. Mangeney (2011). Ocean wave sources of seismic noise, *Journal of Geophysical Research* **116**, C05002, doi:10.1029/2011JC006952.

Ardhuin, F., A. Balanche, E. Stutzmann, and M. Obrebski (2012). From seismic noise to ocean wave parameters: General methods and validation, *Journal of Geophysical Research **117***, C05002.

Asplin, M. G., R. Galley, D. G. Barber, and S. Prinsenberg (2012). Fracture of summer perennial sea ice by ocean swell as a result of arctic storms, *Journal of Geophysical Research: Oceans* **117** (C6), doi:10.1029/2011JC007221.

Aster, R.C., D. E. McNamara, and P. D. Bromirski (2008). Multidecadal climate-induced variability in microseisms, *Seismological Research Letters* **79**, 194-202.

Aster, R.C., D. E. McNamara, and P.D. Bromirski (2010). Global trends in extremal microseism intensity, *Geophysical Research Letters* **37**, L14303, doi:10.1029/2010GL043472.

Bahavar, M., A.R. Hutko, C.M. Trabant, K.D. Koper, R.E. Anthony, R.C. Aster (2013). The New IRIS DMC Noise Toolkit, Poster, *AGU Fall Meeting*, San Francisco, CA.

Baker, M.G., R. Aster, J. Chaput, R. Anthony, D. Wiens, A. Nyblade, P. Bromirski, P. Gerstoft, R. Stephen, A. Diez (2016), Teleseismic Earthquake Signals Observed on an Ice Shelf: Propsects for Earth Imaging Employing Floating-Platform Seismographs, Poster, *SSA Annual Meeting*, Reno, NV.

Bartholomaus, T. C., J. M. Amundson, J. I. Walter, S. O'Neel, M. E. West, and C. F. Larsen (2015), Subglacial discharge at tidewater glaciers revealed by seismic tremor, *Geophysical Research Letters*, **42** (15), 6391–6398.

Benson, M.A. and T. Dalrymple (1967), General field and office procedures for indirect discharge measurements, *U.S. Govt. Print. Off.*, No. 03-A1.

Bodin, P., and S. Horton (1999), Broadband microtremor observation of basin resonance in the Mississippi embayment, central U.S.: Implications for seismic hazard assessment, *Geophys. Res. Lett*., **26**, 903-906.

Bodin, P., K. Smith, S. Horton, and H. Hwang (2001), Microtremor observations of deep sediment resonance in metropolitan Memphis, Tennessee, *Engin. Geol*., ***62***, 159-168.

Boulton, A. J., S. Findlay, P. Marmonier, E. H. Stanley, and H. M.Valett (1998), The functional significance of the hyporheic zone in streams and rivers. *Annual Review of Ecology and Systematics*, 59-81.

Bromirski, P. D., R. E. Flick, and N. Graham (1999). Ocean wave height determined from inland seismometer data: Implications for investigating wave climate, *Journal of Geophysical Research*, **104** (C9), 20–753.

Bromirski, P. D., and F. K. Duennebier (2002), The near-coastal microseism spectrum: Spatial and temporal wave climate relationships, *Journal of Geophysical Research: Solid Earth*, **107** (B8).

Bromirski, P.D., F. K. Duennebier, and R. A. Stephen (2005), Mid-ocean microseisms, *Geochemisty, Geophysics, Geosystems* **6**, Q04009, doi:10.1029/2004GC000768.

Bromirski, P. D., R. A. Stephen, and P. Gerstoft (2013), Are deep-ocean-generated surface wave microseisms observed on land?, *Journal of Geophysical Research: Solid Earth*, **118** (7), 3610–3629.

Bunte, K., and S.R. Abt (2005), Effect of sampling time on measured gravel bed- load transport rates in a coarse-bedded stream, *Water Resources Research*, **41**, W11405.

Burtin, A., L. Bollinger, J. Vergne, R. Cattin, and J. Nabelek (2008), Spectral analysis of seismic noise induced by rivers: A new tool to monitor spatiotemporal changes in stream hydrodynamics, *Journal of Geophysical Research: Solid Earth*, **113** (B5).

Burtin, A., R. Cattin, L. Bollinger, J. Vergne, P. Steer, A. Robert, N. Findling, and C. Tiberi (2011), Towards the hydrologic and bed load monitoring from high-frequency seismic noise in a braided river: The torrent de St Pierre, French Alps, *Journal of hydrology*, **408** (1), 43–53.

Burtin, A., N. Hovius, amd J. M. Turowski (2016), Seismic monitoring of torrential and fluvial processes, *Earth Surface Dynamics,* **4**, 285-307.

Butler, R., et al. (2004). The global seismographic network surpasses its design goal, *Eos Transactions AGU*, 85(23), 225–229, doi:10.1029/2004EO230001

Cavalieri, D. J., C. L. Parkinson, P. Gloersen, and H. Zwally (1996), Sea ice concentrations from Nimbus-7 SMMR and DMSP SSM/I passive microwave data, Digital media, NASA National Snow and Ice Data Center Distributed Active Archive Center, Boulder, Colorado USA.

Cessaro, R. K. (1994), Sources of primary and secondary microseisms, *Bulletin of the Seismological Society of America*, 84 (1), 142–148.

Chaput, J., R. Aster, X. Sun, D. Wiens, A. Nyblade, S. Anandakrishnan, A. Huerta, P. Winberry, and T, Wilson (2014), Crustal thickness across West Antarctica, *Journal of Geophysical Research* **119**, 378-395.

Chen, Y.-N., Y. Gung, S.-H. You, S.-H. Hung, L.-Y. Chiao, T.-Y. Huang, Y.-L. Chen, W.-T. Liang, and S. Jan (2011), Characteristics of short period secondary microseisms (SPSM) in Taiwan: The influence of shallow ocean strait on SPSM, *Geophysical Research Letters*, **38** (4).

Cook, A. J., and D. G. Vaughan (2010), Overview of areal changes of the ice shelves on the Antarctic Peninsula over the past 50 years, *Cryosphere***, 4** (1), 77–98.

Demuth, A., L. Ottemöller, and H. Keers (2016), Ambient noise levels and detection threshold in Norway, *Journal of Seismology,* 1-16.

Engdahl, E.R. and R.H. Gunst (1966), Use of high speed computer for the preliminary determination of earthquake hypocenters, *Bull. Seismol. Soc. Am.,* **56,** 2, 325–336.

Fetterer, F., K. Knowles, W. Meier, and M. Savoic (2002), *Sea Ice Index*, digital media, Natl. Snow and Ice Data Cent., Boulder, Colorado USA.

Ferretti, G., D. Scafidi, L. Cutroneo, S. Gallino, M. Capello (2016), Applicability of an empirical law to predict significant sea-wave heights from microseisms along the Western Ligurian Coast (Italy), *Continental Shelf Research* **122**, 1, 36-42.

Galperin, E. I., I. L. Nersesov, and R. M. Galperina (1986). *Borehole Seismology and the Study of the Seismic Regime of Large Industrial Centers,* Reidel, Dordrecht, 315 pp.

Gerstoft, P., and T. Tanimoto (2007), A year of microseisms in southern California, *Geophysical Research Letters*, **34** (20).

Gimbert, F., V. C. Tsai, and M. P. Lamb (2014), A physical model for seismic noise generation by turbulent flow in rivers, *Journal of Geophysical Research: Earth Surface*, **119** (10), 2209–2238.

Gimbert, F., V. C. Tsai, J. M. Amundson, T. C. Bartholomaus, and J. Walter (2016), Subseasonal changes observed in subglacial channel pressure, size, and sediment transport. *Geophysical Research Letters*, ***43*** (8), 3786-3794.

Gow, A.J. (1963). Age Hardening of snow at the South Pole, *Journal of Glaciology* **4**(35), 521-536.

Gow, A.J. (1975). Time-temperature dependence of sintering in perennial isothermal snowpacks, *International Association of Hydrological Sciences Publications* **114**, 25-41.

Grob, M., A. Maggi and E. Stutzmann (2011). Observations of the seasonality of the Antarctic microseismic signal, and its association to sea ice variability, *Geophysical Research Letters* **38***,* L11302, doi: 10.1029/2011GL047525.

Hande, L., S. Siems, and M. Manton (2012), Observed trends in wind speed over the southern ocean, *Geophysical Research Letters*, **39** (11).

Hansen, S.E., A. Nyblade, D.S. Heezel, D.A. Wiens, P. Shore, and M. Kanao (2010). Crustal structure of the Gamburtsev Mountains, East Antarctica, from S-wave receiver functions and Rayleigh wave phase velocities, *Earth and Planetary Science Letters* **300**, 395-401.

Hasselmann, K (1963), A statistical analysis of the generation of microseisms, *Reviews of Geophysics,* **1** *(2)*, 177-210.

Hedlin, M A., and B. Alcoverro (2005), The use of impedance matching capillaries for reducing resonance in rosette infrasonic spatial filters, *The Journal of the Acoustical Society of America,* **117** (4), 1880-1888.

Heeszel, D.S., D.A. Wiens, A.A Nyblade, S.E. Hansen, M. Kanao, M. An, Y. Zhao (2013). Rayleigh wave constraints on the structure and tectonic history of the Gamburtsev Subglacial Mountains, East Antarctica, *Journal of Geophysical Research* **118**, 2138-2153.

Hsu, L., N. J. Finnegan, and E. E. Brodsky (2011), A seismic signature of river bedload transport during storm events, *Geophysical Research Letters*, **38** (13).

Ibs-von Seht, M., and J. Wohlenberg (1999), Microtremors measurements used to map thickness of soft soil sediments, *Bulletin of the Seismological Society of America*, **89**, 250-259.

IRIS (1994), Federation of Digital Seismographic Networks Station Book, Seattle, Wash.

Izaguirre, C., F. J. M´endez, M. Men´endez, and I. J. Losada (2011), Global extreme wave height variability based on satellite data, *Geophysical Research Letters*, **38** (10).

IPCC (2007). Solomon, S., D. Qin, M. Manning, Z. Chen, M. Marquis, K.B. Averyt, M. Tignor, and H.L. Miller (eds.), Climate Change 2007: The Physical Science Basis. Contributions of the Working Group 1 to the Fourth Assessment Report of the Intergovernmental Panel of Climate Change, Cambridge University Press, Cambridge, United Kingdom and New York, NY, USA.

Johnson, J.B., J. M. Lees, and H. Yepes (2006), Volcanic eruptions, lightning, and a waterfall: Differentiating the menagerie of infrasound in the Ecuadorian jungle, *Geophysical Research Letters*, **33** (6).

Koch, F.W., D.A. Wiens, G.G. Euler, A.A. Nyblade, S. Anandakrishnan, A. Huerta, T.J. Wilson, and R.C. Aster, Tracking the Effect of Sea Ice Cover on Microseismic Noise Using Two Seismic Arrays in Antarctica (2013). Abstract Seismological Society of America Annual Meeting.

Kohnen, H. (1974). The Temperature Dependence of Seismic Waves in Ice, *Journal of Glaciology* **13**, 144-147.

Kohout, A., M. Williams, S. Dean, and M. Meylan (2014), Storm-induced sea-ice breakup and the implications for ice extent, *Nature*, **509** (7502), 604–607.

Kovacs, A. (1996), Sea ice: Part ii. estimating the full-scale tensile, flexural, and compressive strength of first-year ice, Tech. rep., DTIC Document.

Larose, E., et al. (2015), Environmental seismology: What can we learn on earth surface processes with ambient noise?, *Journal of Applied Geophysics*, **116**, 62–74.

Lefebvre, W., H. Goosse, R. Timmermann, and T. Fichefet (2004), Influence of the southern annular mode on the sea ice-ocean system, *Journal of Geophysical Research: Oceans*, **109** (C9), doi:10.1029/2004JC002403.

Li, T. M. C., J. F. Ferguson, E. Herrin, and H. B. Durham (1984). High-frequency seismic noise at Lajitas, Texas, *Bulletin of the Seismological Society of America* **74***,* 2015-2033.

Lin, F.-C., M. H. Ritzwoller, and N. M. Shapiro (2006), Is ambient noise tomography across ocean basins possible?, *Geophysical Research Letters*, **33** (14).

Liu, J., J. A. Curry, and D. G. Martinson (2004), Interpretation of recent Antarctic sea ice variability, *Geophysical Research Letters*, **31** (2).

Lloyd, A., A. Nyblade, D. Wiens, S. Hansen, M. Kanao, P. Shore, D. Zhao, (2013). Upper mantle seismic structure beneath the East Antarctic Shield from body wave tomography: Implications for the origin of the Gamburtsev Subglacial Mountains, *Geochemistry, Geophysics and Geosystems* **14**, doi: 10.1002/ggge.20098.

Longuet-Higgins, M. S. (1950). A theory of the origin of microseisms, *Philosophical Transactions of the Royal Society A* **243***,* 1-35.

Lough, A.C., D.A. Wiens, C.G. Barcheck, S. Anandakrishnan , R.C. Aster, D.D. Blankenship, A.D. Huerta, A. Nyblade, D.A. Young, and T.J. Wilson (2013), Seismic detection of an active subglacial magmatic complex in Marie Byrd Land, Antarctica, *Nature Geoscience* **6**, 1031-1035.

MacAyeal, D., E. Okal, R. Aster, (2006), Transoceanic wave propagation links iceberg calving margins of Antarctica with storms in tropics and N. hemisphere, *Geophysical Research Letters* **33***,* L17502, doi: 10.1029/2006GL027235.

Mahoney, A. R., D. O. Dammann, M. A. Johnson, H. Eicken, and F. J. Meyer (2016), Measurement and imaging of infragravity waves in sea ice using insar, *Geophysical Research Letters*, **43** (12), 6383–6392, doi:10.1002/2016GL069583.

Marcillo, O., Johnson, J. B., and Hart, D. (2012), Implementation, characterization, and evaluation of an inexpensive low-power low-noise infrasound sensor based on a micromachined differential pressure transducer and a mechanical filter. *Journal of Atmospheric and Oceanic Technology*,**29** (9), 1275-1284.

Marshall, G. J., A. Orr, N. P, Van Lipzig, and J. C. King (2006), The impact of a changing Southern Hemisphere Annular Mode on Antarctic Peninsula summer temperatures, *Journal of Climate*, *19*(20), 5388-5404.

Maslanik, J., C. Fowler, J. Stroeve, S. Drobot, J. Zwally, D. Yi, and W. Emery (2007), A younger, thinner arctic ice cover: Increased potential for rapid, extensive sea-ice loss, *Geophysical Research Letters*, *34* (24).

Mayewski et al. (2009). State of the Antarctic and Southern Ocean Climate System, *Reviews of Geophysics* **47**, RG1003.

McMahon, N.D., H.M. Benz, C.E. Johnson, R.C. Aster, D.E. McNamara, and W.L. Yeck (2016), The 6 November 2011 M5.6 Prague Oklahoma aftershock sequence studied using subspace detection, Poster, *SSA Annual Meeting*, Reno, NV.

McNamara, D. and R. Buland (2004). Ambient noise levels in the continental United States, *Bulletin of the Seismological Society of America* **94***,* 1517-1527.

McNamara, D. and R. Boaz (2011). PQLX: A seismic data quality control system description, applications, and users manual, *U.S. Geological Survey Open-File Report 2010-1292*.

Molnar, P., B.E. Tucker, and J.M. Brune (1973), Corner Frequencies of P and S Waves and Models of Earthquake Sources, *Bull. Seism. Soc. Am***, 63***,* 6, 2091-2104.

Nakamura, Y. (1989), A method for dynamic characteristic estimation of subsurface using microtremor on the ground surface, *QR Railway Tech. Res. Inst*., **30**.

Norman, E. C., N. J. Rosser, M. J. Brain, D. N. Petley, and M. Lim (2013), Coastal cliff-top ground motions as proxies for environmental processes*, Journal of Geophysical* Research *Oceans* **118**, 6807–6823.

Nyblade et al. (2012), A facility plan for polar seismic and geodetic science, Joint IRIS/UNAVCO Workshop Report, IRIS Consortium, http://www.iris.edu/hq/files/publications/other_workshops/docs/APOS_FINAL.pdf

Obrebski, M., F. Ardhuin, E. Stutzmann, and M. Schimmel (2013), Detection of microseismic compressional (p) body waves aided by numerical modeling of oceanic noise sources, *Journal of Geophysical Research: Solid Earth*, **118** (8), 4312–4324.

O'Neel, S., H. P. Marshall, D. E. McNamara, and W. T. Pfeffer (2007), Seismic detection and analysis of icequakes at Columbia Glacier, Alaska, *Journal of Geophysical Research* **112**, F03S23

Oppenheim, A. V. and R. Schafer (1975), *Digital Signal Processing.* Englewood Cliffs, NJ: Prentice-Hall.

Parkinson, C. L., and D. J. Cavalieri (2012), Antarctic sea ice variability and trends 1979-2010, *The Cryosphere*, **6**, 871-880.

Patterson, W. S. B. (1994). *The Physics of Glaciers, Third edition*, Pergammon Press, NY.

Peng, Z., Walter, J., Aster, R., Nyblade, A., Wiens, D., Anandakrishnan, S. (2014). Dynamically triggered icequakes in Antarctica, *Nature Geoscience, doi: 10.1038/NGEO2212.*

Peterson, J. (1993). Observation and modeling of seismic background noise. USGS Technical Report 93-322.

Poppeliers, C., and D. Mallison (2015), High frequency seismic noise generated from breaking shallow water ocean waves and the link to time-variable sea states, *Geophysics Research Letters,* **42**, 8563-8569.

Pratt, M. J., D. A. Wiens, J. P. Winberry, S. Anandakrishnan, and G. G. Euler (submitted), Implications of sea ice on Southern Ocean microseisms using a seismic array in west antarctica, *Geophysics Journal International*.

Pritchard, H. D., and D. G. Vaughan (2007), Widespread acceleration of tidewater glaciers on the Antarctic Peninsula, *Journal of Geophysical Research: Earth Surface*, **112** (F3).

Pritchard, H. D., R. J. Arthern, D. G. Vaughan, and L. A. Edwards (2009), Extensive dynamic thinning on the margins of the Greenland and Antarctic ice sheets*, Nature*, **461** (7266), 971–975

Rhie, J. and B. Romanowicz (2004). Excitation of Earth's continuous free oscillations by atmosphere-ocean-seafloor coupling, *Nature* **431***,* 552-556.

Ringler, A.T. and C.R. Hutt (2010). Self-Noise Models of Seismic Instruments*, Seismic Research Letters* **81,** doi:10.1785/gssrl.81.6.972.

Roth, D. L., E. E. Brodsky, N. J. Finnegan, D. Rickenmann, J. M. Turowski, and A. Badoux (2016), Bed load sediment transport inferred from seismic signals near a river, *Journal of Geophysical Research: Earth Surface*, **121** (4), 725–747.

Rott, H., P. Skvarca, and T. Nagler (1996), Rapid collapse of the northern Larsen ice shelf, Antarctica, *Science*, **271** (5250), 788.

Ryan, S. E. (2007), The role of geology in sediment supply and bedload transport patterns in coarse-grained streams*, Proceedings of the Forest Service National Earth Sciences Conference*, edited by M. Furniss, C. Clifton, and K. Ronnenberg, PNW-GTR-689, pp. 383–390, U.S. Department of Agriculture, Forest Service, Portland, Ore.

Scambos, T. A., J. Bohlander, C. u. Shuman, and P. Skvarca (2004), Glacier acceleration and thinning after ice shelf collapse in the Larsen B embayment, Antarctica, *Geophysical Research Letters*, **31** (18).

Scambos, T. A., C. Hulbre, M. Fahnestock, and J. Bohlander (2000), The link between climate warming and break-up of ice shelves in the Antarctic Peninsula, *Journal of Glaciology*, ***46*** (154), 516-530.

Schmandt, B., R. C. Aster, D. Scherler, V. C. Tsai, and K. Karlstrom (2013), Multiple fluvial processes detected by riverside seismic and infrasound monitoring of a controlled flood in the grand canyon, *Geophysical Research Letters*, **40** (18), 4858–4863.

Schmandt, B., and R. W. Clayton (2013), Analysis of teleseismic P waves with a 5200-station array in Long Beach, California: Evidence for an abrupt boundary to Inner Borderland rifting. *Journal of Geophysical Research: Solid Earth*, ***118***(10), 5320-5338.

Seeger, M., M. P. Errea, S. Beguerıa, J. Arnáez, C. Martı, and J. M. Garcıa-Ruiz (2004), Catchment soil moisture and rainfall characteristics as determinant factors for discharge/suspended sediment hysteretic loops in a small headwater catchment in the Spanish Pyrenees. *Journal of Hydrology*,***288***(3), 299-311.

Sorrells, G. G. (1971). A preliminary investigation into the relationship between long-period seismic noise and local fluctuations in the atmospheric pressure field, *Geophysical Journal of the Royal Astronomical Society* **26***, no. 1-4*, 71-82.

Stephen, R. A., F. N. Spiess, J. A. Collins, J. A. Hildebrand, J. A. Orcutt, K. R. Peal, F. L. Vernon, and F. B. Wooding (2003), Ocean seismic network pilot experiment, *Geochemistry, Geophysics, Geosystems*, **4** (10).

Stutzmann, E., M. Schimmel, G. Patau, and A. Maggi (2009). Global climate imprint on seismic noise, *Geochemistry, Geophysics, Geosystems* **10,** Q11004, doi: 10.1029/2009GC002619.

Tanimoto, T. (2007). Excitation of Microseisms, *Journal of Geophysical Research, 34,* L05308, doi:10.1029/2006GL029046.

Thompson, D. W., and S. Solomon (2002), Interpretation of recent southern hemisphere climate change, *Science*, **296** (5569), 895–899.

Thompson, D. W., S. Solomon, P. J. Kushner, M. H. England, K. M. Grise, and D. J. Karoly (2011), Signatures of the antarctic ozone hole in southern hemisphere surface climate change, *Nature Geoscience*, **4** (11), 741–749.

Thompson, D.W., and J. D. Woodworth (2014), Thompson, D. W., & Woodworth, J. D. (2014). Barotropic and baroclinic annular variability in the Southern Hemisphere. *Journal of the Atmospheric Sciences*, **71** (4), 1480-1493.

Thomson, J., and W. E. Rogers (2014), Swell and sea in the emerging arctic ocean, *Geophysical Research Letters*, **41** (9), 3136–3140, doi:10.1002/2014GL059983.

Tokinaga, H. and S. P. Xie (2011), Wave-and Anemometer-Based Sea Surface Wind (WASWind) for Climate Change Analysis, *Journal of Climate*, **24** (1), 267-285.

Traer, J., P. Gerstoft, P.D. Bromirski, and P.M. Shearer (2012). Microseisms and hum from ocean surface gravity waves, *Journal of Geophysical Research,* **117**, B11307, doi:10.1029/2012JB009550.

Tsai, V. C., and D. E. McNamara (2011). Quantifying the influence of sea ice on ocean microseism using observations from the Bering Sea, Alaska, *Geophysical Research Letters* **38**, L22502, doi:10.1029/2011GL049791.

Tsai, V. C., B. Minchew, M. P. Lamb, and J.-P. Ampuero (2012), A physical model for seismic noise generation from sediment transport in rivers, *Geophysical Research Letters*, **39** (2).

Turner, J., S. R. Colwell, G. J. Marshall, T. A. Lachlan-Cope, A. M. Carleton, P. D. Jones, V. Lagun, P. A. Reid, and S. Iagovkina (2005), Antarctic climate change during the last 50 years, *International journal of Climatology*, **25** (3), 279–294.

Turner, J., J. C. Comiso, G. J. Marshall, T. A. Lachlan-Cope, T. Bracegirdle, T. Maksym, M. P. Meredith, Z. Wang, and A. Orr (2009), Non-annular atmospheric circulation change induced by stratospheric ozone depletion and its role in the recent increase of Antarctic sea ice extent, *Geophysical Research Letters*, **36** (8).

Turner, J., T. Maksym, T. Phillips, G. J. Marshall, and M. P. Meredith (2013), The impact of changes in sea ice advance on the large winter warming on the western Antarctic Peninsula, *International Journal of Climatology*, **33** (4), 852–861.

Van den Broeke (2008). Depth and Density of the Antarctic Firn Layer, *Arctic, Antarctic, and Alpine Research* **40**, 432-438.

Vaughan, D. G., G. J. Marshall, W. M. Connolley, C. Parkinson, R. Mulvaney, D. A. Hodgson, J. C. King, C. J. Pudsey, and J. Turner (2003), Recent rapid regional climate warming on the Antarctic Peninsula, *Climatic Change*, **60** (3), 243–274.

West, M.E., C.F. Larsen, M. Truffer, S. O'Neel, and L. LeBlanc (2010). Glacier Microseismicity, *Geology* **38**, 319-322, doi:10.1130/G30606.1.

White, D.S., (1993), Perspectives on defining and delineating hyporheic zones, *Journal of the North American Benthological Society*, **12** (1), 61-69.

Wielandt, E. and T. Forbriger (1999), Near-field seismic displacement and tilt associated with the explosive activity of Stromboli, *Annali Di Geofisica*, **42** (3), 407-416.

Wiens, D.A., S. Anandakrishnan, J.P. Winberry, and M.A. King (2008). Simultaneous teleseismic and geodetic observations of stick-slip motion of an Antarctic ice stream, *Nature* **453**, 770-775, doi:10.1038/nature06990.

Wiens, D.A., S. Anandakrishnan, J.P. Winberry, and M.A. King (2008), Simultaneous teleseismic and geodetic observations of stick-slip motion of an Antarctic ice stream, *Nature* **453**, 770-775.

Wiens, D., D. Heeszel, X. Sun, A. Lloyd, A. Nyblade, S. Anandakrishnan, R. Aster, J. Chaput, A. Huerta, S. Hansen, and T. Wilson (2013). Lithospheric Structure of Antarctica and Implications for Geological and Cryospheric Evolution, *Porc. IASPEI Meeting*, Gothenburg, Sweden, July, 2013.

Williams, R. A., W. J. Stephenson, J. K. Odum, and D. M. Worley (1997), High-resolution surface-seismic imaging techniques for NEHRP soil profile classifications and earthquake hazard assessments in urban areas (No. 97-501), US Geological Survey; Branch of Information Services.

Wilson, D., J. Leon, R. Aster, J. Ni, J. Schlue, S. Grand, S. Semken, S. Baldridge, and W. Gao (2002). Broadband seismic background noise at temporary seismic stations observed on a regional scale in the southwestern United States. *Bulletin of the Seismological Society of America* **92***,* 3335-3341.

Winberry, J.P, S. Anandakrishnan, R.B. Alley, R. Bindschadler, and M. King (2009). Basal Mechanics of ice streams: Insights from stick-slip motion. J*ournal of Geophysical Research-Earth Surface*, F01016, doi:10.1029/2008JF001035.

Winberry, J.P., S. Anandakrishnan, D.A. Wiens, and R.B. Alley (2011). Dynamics of ice-stream stick-slip motion, *Earth and Planetary Science Letters* **305**, 283-289.

Winter, T. C. (1998), *Ground water and surface water: a single resource*. Vol. 1139. DIANE Publishing Inc.

Withers, M., R. Aster, C. Young, and E. Chael (1996). High-frequency analysis of seismic background noise and signal-to-noise ratio near Datil, New Mexico, *Bulletin of the Seismological Society of America* **86**, 1507-1515.

Yang, X.-Y., R. X. Huang, and D. X. Wang (2007), Decadal changes of wind stress over the southern ocean associated with Antarctic ozone depletion, *Journal of Climate*, **20** (14), 3395–3410

Ying, Y., C. J. Bean, and P. D. Bromirski (2014), Propagation of microseisms from the deep ocean to land, *Geophysical Research Letters*, **41** (18), 6374–6379.

Young, C. J., E. P. Chael, M. M. Withers, and R. C. Aster (1996). A comparison of high frequency (≥1 Hz) surface and subsurface noise environment at three sites in the United States, *Bulletin of the Seismological Society of America,* **86***,* 1516-1528.

Young, I. (1999), Seasonal variability of the global ocean wind and wave climate, *International Journal of Climatology*, **19** (9), 931–950.

Young, I. R., S. Zieger, and A. V. Babanin (2011), Young, I. R., Zieger, S., & Babanin, A. V. (2011), Global trends in wind speed and wave height. *Science*, **332** (6028), 451-455.

Zeiler, C., and A.A. Vekasco (2009). Seismogram picking error from analyst review (SPEAR): Single-analyst and institution analysis, *Bulletin of the Seismological Society of America,* **99,** no. 5, 2759-2770.

Zhang, J., P. Gerstoft, and P.M. Shearer (2009). High-frequency P-wave seismic noise driven by ocean winds, *Geophysics Research Letters* **36.**

Appendix 1: Spectral Resolution and Significance

Tradeoff in Spectral Estimates Between Uncertainty and Resolution

When estimating the power spectrum of a timeseries, an inherent tradeoff exists between the uncertainty in the power estimate attained at each frequency and the spectral resolution. Ultimately, maximal spectral resolution is pre-determined by the length, *T,* of the times series analyzed, with bandwidth given by *1/T*. It is important to note that the spectral bandwidth is independent of the sampling frequency, f_s, which determines the highest resolvable frequencies (i.e. the Nyquist frequency; $\frac{1}{2} f_s$) of the sampled (assumed unaliased) timeseries. In the discussion that follows, we will assume that the timeseries is uniformly sampled, which is the case for seismological data analyzed within the dissertation.

A timeseries of length *T* sampled at frequency f_s will have $N = f_s T$ data points. For a real-valued timeseries the spectrum is Hermitian. Thus, the discrete Fourier transform (DFT) of the timeseries will have *N/2* distinct spectral estimates at frequencies from zero to $\frac{1}{2} f_s$ in intervals of *1/T*. For example, the DFT of a 100 s timeseries sampled at 0.5 Hz will have 25 spectral estimates between zero to 0.24 Hz with a uniform spacing of 0.01 Hz. However, although we have a relatively high degree of spectral resolution, the uncertainty of each of these DFT spectral estimates is high and may exceed the variance of the spectrum itself (*Oppenheim and Schafer*, 1975). In addition, the resolution of a spectrum is controlled by the time domain windowing function applied to the data, so that the expected value of the estimate will be the true spectrum convolved with the Fourier transform of the windowing function.

Why are these spectral estimates so low quality? It is due to the low number of individual pieces of information, called degrees of freedom, which determine each spectral estimate. As the spectral estimate of a given frequency is constructed from one sine wave and one cosine, only two degrees of freedom (corresponding to the real and imaginary parts of the discrete Fourier spectrum) are associated with each frequency. Thus, the simple (periodogram) estimate of a power spectral density from unit variance uncorrelated Gaussian white noise is the sum of squares of two normally distributed (real and imaginary) DFT estimates, which is distributed as the chi-square distribution with two degrees of freedom (Figure A1.1) To obtain statistically significant results that are reproducible, spectra must be computed where each Fourier frequency has an increased number of degrees of freedom.

Techniques to Improve Statistical Significance of Spectral Estimates

One methodology to do this is to average *n* adjacent frequency bands together. This procedure, called band averaging, increases the degrees of freedom of each spectral estimate by up to approximately (depending on window and band overlap details) a factor of *n* with the tradeoff that spectral resolution has been diminished to *n/T*. For instance, say we take our earlier example of a DFT of a 100 s timeseries sampled at 0.5 Hz and average each spectral estimate across five Fourier Coefficients. The new spectrum would contain only five spectral estimates each with 10 degrees of freedom, but a bandwidth of only 0.05 Hz. Thus, in order to attain a more statistically significant result, we have settled for decreased spectral resolution.

Another technique is to break the full timeseries into *m* equal-length windows, calculate a separate spectrum for each window, and then average these individual spectral estimates

together. This methodology, called ensemble averaging, increases the degrees of freedom of each spectral estimate by a factor of *m*, but again with the tradeoff that spectral resolution is decreased by *m/T*. Furthermore, as each spectrogram is taken from a shorter time window, the lowest resolvable frequency estimate drops to *m/T* as well. Taking our 100-s record sampled at 0.5 Hz example again, we could break the timeseries into five windows of 20 s each and take the spectrum of each window. We would now have five separate spectra each with five spectral estimates that range from 0 Hz to 0.20 Hz in steps of 0.05 Hz. Although each spectral estimate now has 10 degrees of freedom, our bandwidth has decreased to 0.05 Hz again.

Statistical Significance of Microseism Peaks Presented in the Dissertation

Both PQLX and the IRIS NTK methodologies of estimating seismic spectra used in the dissertation utilize both band averaging (smoothing) and ensemble averaging to dramatically increase the degrees of freedom in spectral estimates. Welch's method (Welch, 1967) is used for spectral estimation, with each timeseries window divided into 13 overlapping (75%) sub-segments, with each segment demeaned, detrended, and tapered. For the 3-hour window PSD estimates used in Chapter 2, this means that each sub-segment is 45 minutes long and our degrees of freedom for each spectral estimate has increased by a factor of approximately four (180/45 minutes) relative to a single window estimate.

After applying Welch's method, PSD estimates are furthermore band-averaged (smoothed) in 1/8-octave intervals, further increasing the degrees of freedom for the spectral estimate. It is important to note that this method of smoothing is not a simple *n*-point averaging in that the number of adjacent spectral estimates averaged together varies as a function of frequency. A

rough estimate of the number of degrees of freedom associated with each spectral estimate can be determined by dividing the number of data points in each PSD window by the number of spectral estimates (or frequency bins) in the resulting PSD. For the 3-hour window PSD estimates attained in Chapter 2 using 1 Hz data, 108 individual spectral estimates are returned for each PSD estimate. Thus, each spectral estimate has ~100 degrees of freedom and should thus be very stable in terms of having a low uncertainty and high reproducibility (the tradeoff again being decreased spectral resolution, which is not a significant issue for the broad peaks generated by microseism and many other environmental seismic noise processes). For instance, in Figure 1.2, we constructed a probability density function from over 85,000 1-hour PSD estimates and the secondary microseism peak is observed in every estimate (this is similar to the Monte Carlo test of statistical significance). This peak is expected *a priori* based on the fundamental generation mechanism of secondary microseism signals and observations of the period of ocean waves. Thus, the significance of the microseism peaks are well established both from physical first principles and through thousands of PSD estimates in which each frequency band has ~100 degrees of freedom. In the dissertation, we are primarily concerned with how power varies over these broad microseism bands (each band contains 5-7 frequency bins, so the entire primary and secondary microseism bands have ~500-700 degrees of freedom).

Determining the Statistical Significance of a Spectral Peak

However, there are situations when we don't have the luxury of examining thousands of individual PSD estimates to convince ourselves that a peak is significant. For instance, when searching for evidence of the Baroclinic Annular Mode (BAM) in microseism records, we will

have to rely on other methodologies to determine the statistical significance of any peaks (including the 20-30 day BAM peak).

To begin with, we can proceed by formulating a null-hypothesis by fitting background red noise to the spectrogram, with the specific red noise spectrum calculated from the Fourier transform of the timeseries autocorrelation. Red noise commonly appears as a null hypothesis because climatological timeseries data are often correlated. We can then test the significance of a spectral peak at a given frequency by taking the ratio of power spectral density between the calculated spectrum and the red noise spectrum at that frequency. This spectral ratio will be chi-squared distributed with the degrees of freedom specified by the spectral estimation method, which can vary from two (for a simple single window periodogram; Figure A1.1) to large numbers. Generally, the calculation of the effective degrees of freedom in a Welch's or other section averating method will depend on widow overlap and factors associated with the (spectral leakage optimizing) windowing functions used in the algorithm. For large numbers of degrees of freedom, the chi-square distribution approaches a Gaussian distribution. A peak of high statistical significance will thus have a high spectral ratio and occur along the tail of the appropriate chi-squared distribution. Knowing the theoretical distribution of the spectral estimate for the null hypothesis allows us to assess straightforwardly the significance of any spectral peak that may be observed. The probability of a peak of specified value, or larger, occurring anywhere in the spectrum by chance is then found by integrating the area under the appropriate chi-squared distribution from the observed spectral ratio to infinity.

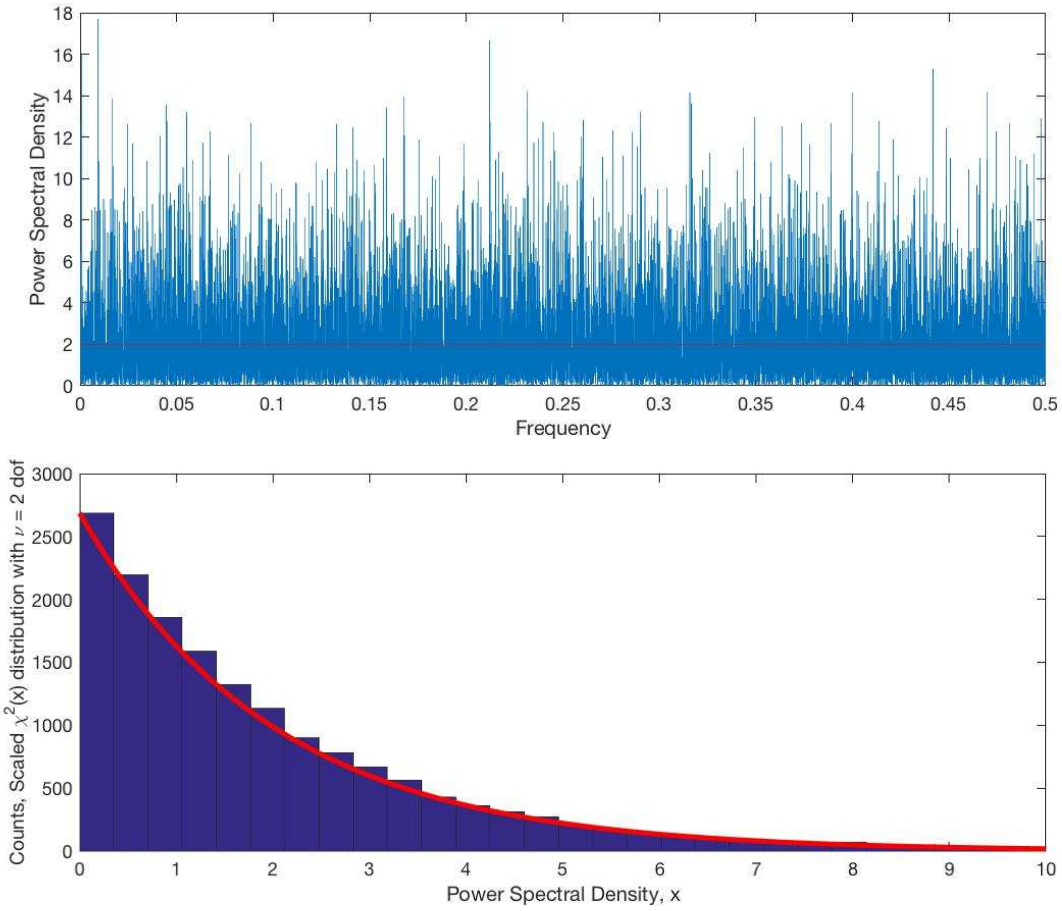

Figure A1.1. Periodogram (positive frequencies) simulation of a random unit variance uncorrelated Gaussian time series of length 2^{15} with unit sampling rate. Top: Periodogram power spectral density estimate, with mean value (~2) indicated. Bottom: Histogram of power spectral density values from the top plot (blue bars), compared with the χ^2 distribution for two degrees of freedom (red curve). The significance of a PSD value being reached or exceeded under the null hypothesis will be the normalized integration of the χ^2 distribution from that particular value to infinity.

References

Hartman, D. (2016), ATMS 552 class notes, chapters 6.1-6.2, University of Washington.

Menke, W and J. Menke (Year Unknown), Environmental Data Analysis with MATLAB class notes, Lecture 24, Lamont-Doherty Earth Observatory.

Welch, P. D. (1967), The Use of fast Fourier transform for the estimation of power spectra: A method based on time averaging over short, modified periodograms*, IEEE Transactions of audio and electroacoustics*, **15** (2), 70-73.

Appendix 2: Supplemental Figures for Chapter 1

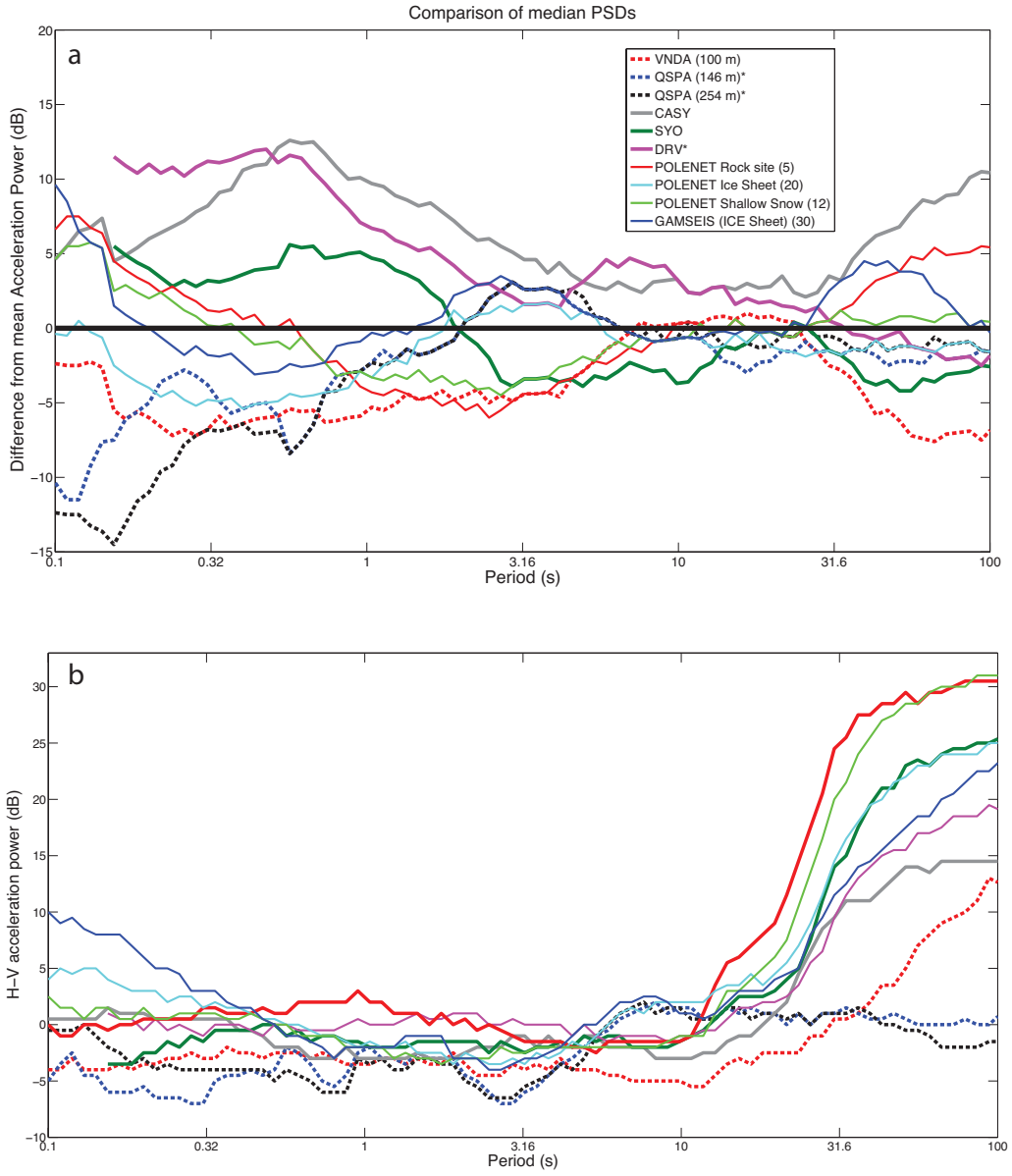

Figure A2.1. (a) Median PSD differences (as in Figure 1.3b) for different emplacement types between 2008-2012. Borehole sensors are indicated by dashed lines and the numbers in the legend represent the number of stations included in the median PSD estimate. Due to instrumentation issues**,** we only used data from February 2011 – December 2012 for the 146 m borehole and didn't include 2012 data for the 254 m borehole. Additionally, due to data availability in the IRIS DMS, DRV data is only through 2010. (b) Subtracting the median horizontal power from vertical power for the different emplacement types is a proxy for sensor tilt.

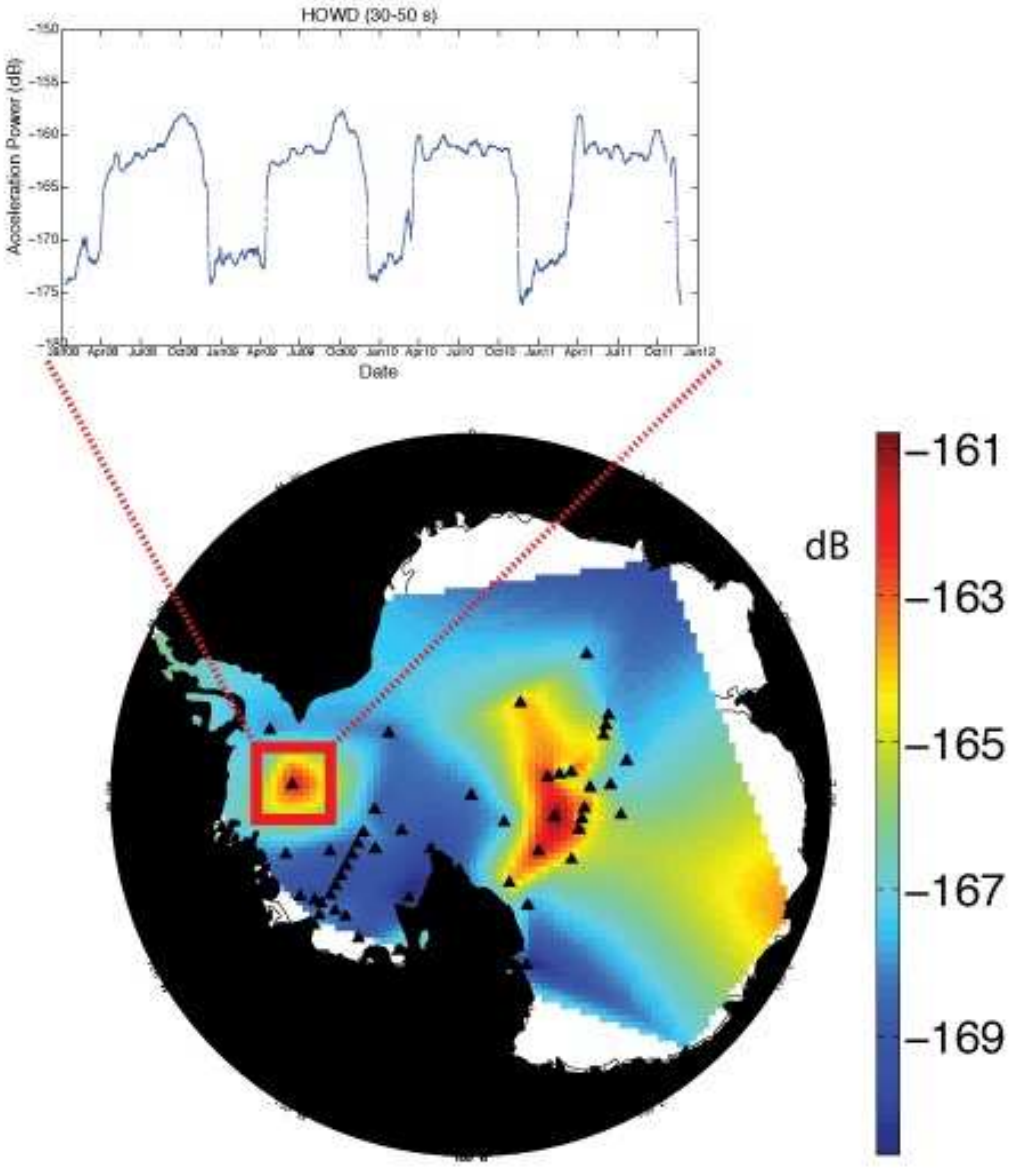

Figure A2.2. Interpolated noise-map of Antarctica for the intermediate period band (20-50 s) median vertical component power for all stations. HOWD and several AGAP instruments were omitted from our final noise-map in this band (Figures 1.5) because their anomalously high noise levels and unique seasonality are caused by the development of long-period convection cells forming within the sensors during the colder months. These air convection cells are caused by the dissipation of heat within the sensor and predominantly impact the vertical components (*Anthony et al.*, 2011; T. Parker (IRIS PASSCAL) pers. comm.). The 2-week moving average of HOWD, shows that this phenomena causes noise in this band to increase by over 10 dB.

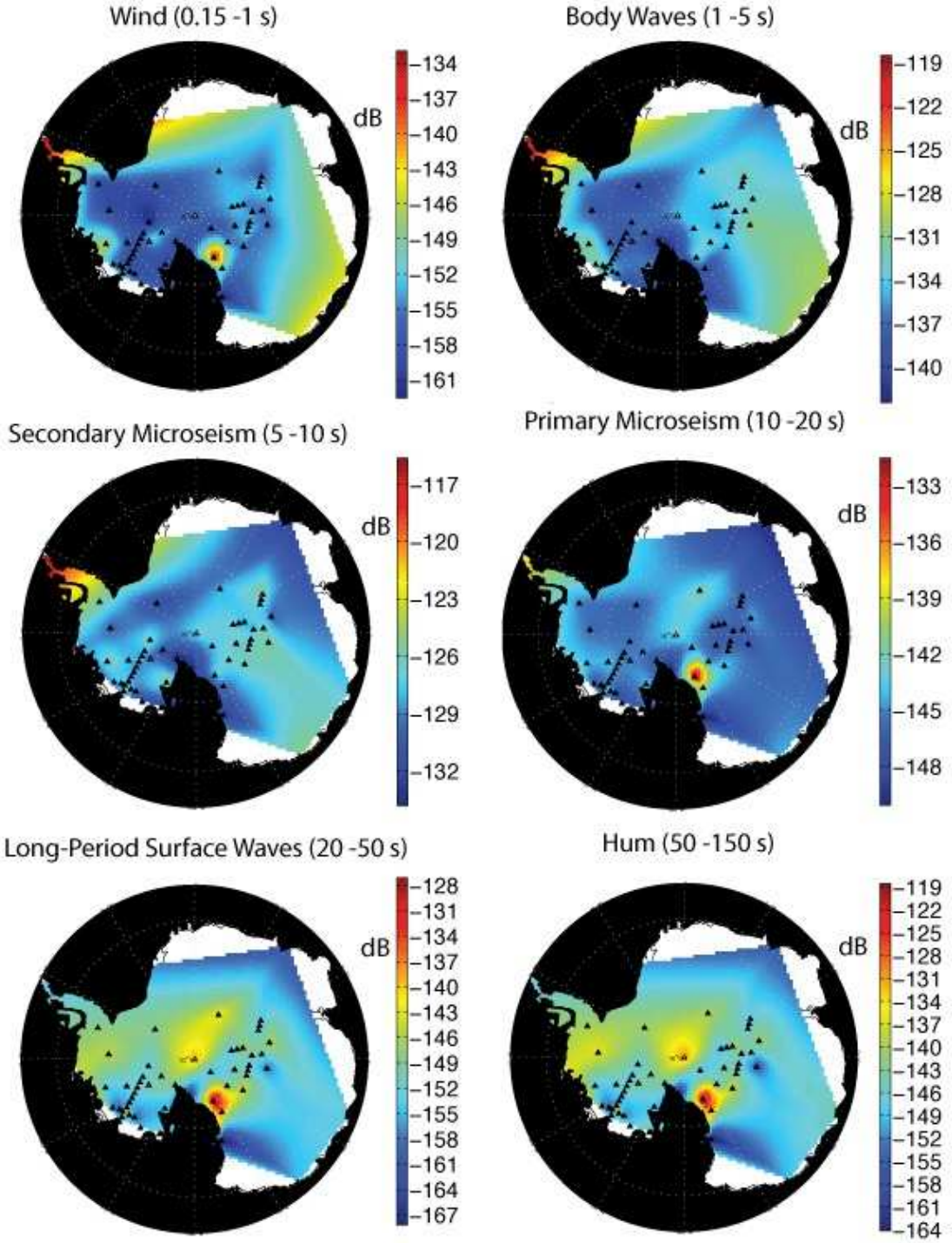

Figure A2.3. Interpolated noise-map of Antarctica for the six period bands using median BHN component power in each for 59 seismic stations (QSPA Surface station used) located across the continent (triangles).

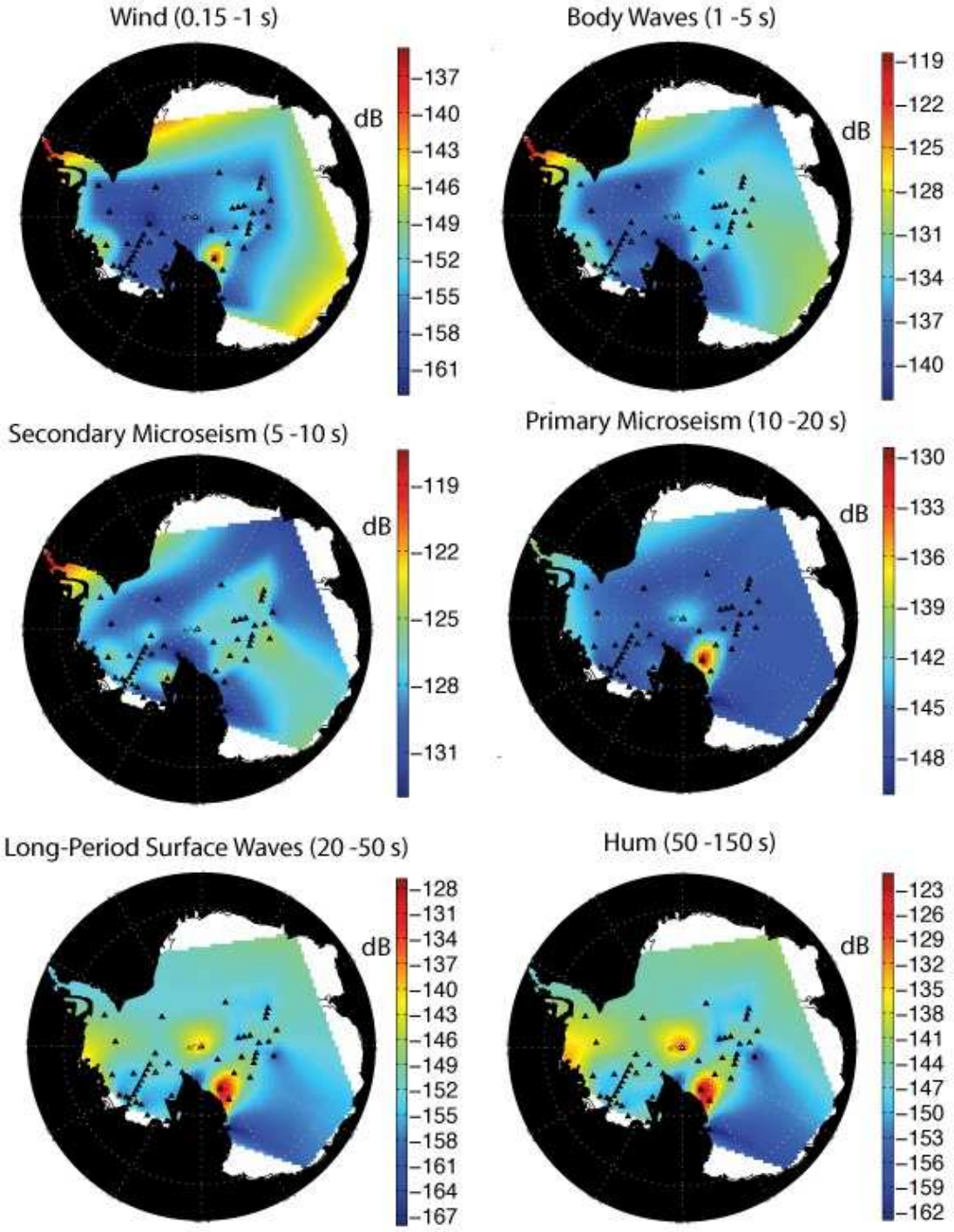

Figure A2.4. Interpolated noise-map of Antarctica for the six period bands using median BHE component power in each for 59 seismic stations (QSPA Surface station used) located across the continent (triangles).

Appendix 3: Significance of Correlation Maps Presented in Chapter 2

In Chapter 2, we inferred the spatial extent to which sea ice can attenuate microseism observations by calculating Pearson's correlation coefficient, *r*, between monthly microseism power and sea ice concentration at numerous grid points around the Antarctic Peninsula. We test the significance of these correlations by identifying sea ice grid points that exceed the 95th percentile statistic of significance for the entire Southern Ocean. We accomplish this using a two-tailed t-test.

The t-test was developed to determine the significance of results derived from a small, randomly selected sample of a larger population. The t-distribution assumes that the independent variable being measured (in this case Pearson's correlation coefficient) is continuous and normally (Gaussian) distributed. The general shape of the t-distribution is dependent on the degrees of freedom associated with the measurement, with lower degrees of freedom having more spread (longer-tails). As the number of degrees of freedom approaches ~30, the t-distribution begins to strongly approximate a normal distribution.

When using the t-test to determine the significance of a correlation coefficient, a null hypothesis is that the correlation coefficient is 0. We use the t-distribution and the length, *n*, of the vectors that we are correlating to determine which correlations would fall outside the 95th percentile of the probability distribution. Since we are interested in testing the validity of both positive and negative correlations, we employ a two-tailed t-test, which will determine the absolute value of the correlation coefficient that is statistically significant. If we had instead used a one-tail

distribution, we would be rejecting the possibility that both positive and negative correlations occur in the data.

The relation between Pearson's correlation coefficient, *r*, and the t-distribution can be expressed as

$$t = r\sqrt{\frac{n-2}{1-r^2}}.$$

Here, the total degrees of freedom in the correlation are given by *n*-2. For example, since we are analyzing 22 years of data at PMSA in Chapter 2, we have 20 degrees of freedom and can easily rearrange the above equation to determine, under the assumption that the observables are independent and Gaussian distributed, that correlation values with an absolute value greater than 0.42 are statistically significant at the 95% confidence interval (i.e., the $t_{0.975}$ value found in a t-distribution table).

Figures A3.1-A3.6 show the correlations expressed in Figures 2.6 and 2.7 in the dissertation but applied to the entire Antarctic sea ice grid with only correlations exceeding the above 95% confidence interval plotted. Significant anti-correlations between sea ice and PMSA microseism power exist in the Bellingshausen Sea during all months plotted and represent the only region with consistent correlation patterns. Spurious positive and negative correlations are seen occasionally over other regions. These may be indicative of a third variable (such as the Southern Annular Mode (SAM) or El Niño-Southern Oscillation) influencing storm and sea ice activity as well random chance correlations, which are expected to occur in ~5% of the SI grid cells. As adjacent 25 km^2 sea ice grid cells are often highly correlated, with significant positive correlations from a single cell capable of extending over several thousand km^2 of regional sea

ice (Figure A3.7), it is unsurprising that occasionally significant correlations with microseism metrics cover large areas not associated with source regions. In Chapter 2, we noted that primary microseism power at PMSA is well coorelated with with the SAM during the month of November (e.g., Figure 2.7). This is further supported by the striking similarity in the sea ice correlation maps between SAM index and primary microseism power observed at PMSA (Figure A3.4).

References

Janda, K. (2001), C10 Elementary Statistics for Political Research Class Notes, Significance of Correlation Coefficient, Northwestern University.

Introduction to SAS (Year Unknown), UCLA Statistical Consulting Group, FAQ: What are the differences between one-tailed and two-tailed tests?, accessed November 17th, 2016.

Maverick, J.B. (2015), What assumptions are made when conducting a t-test?, *Investopedia,* accessed November 20th, 2016.

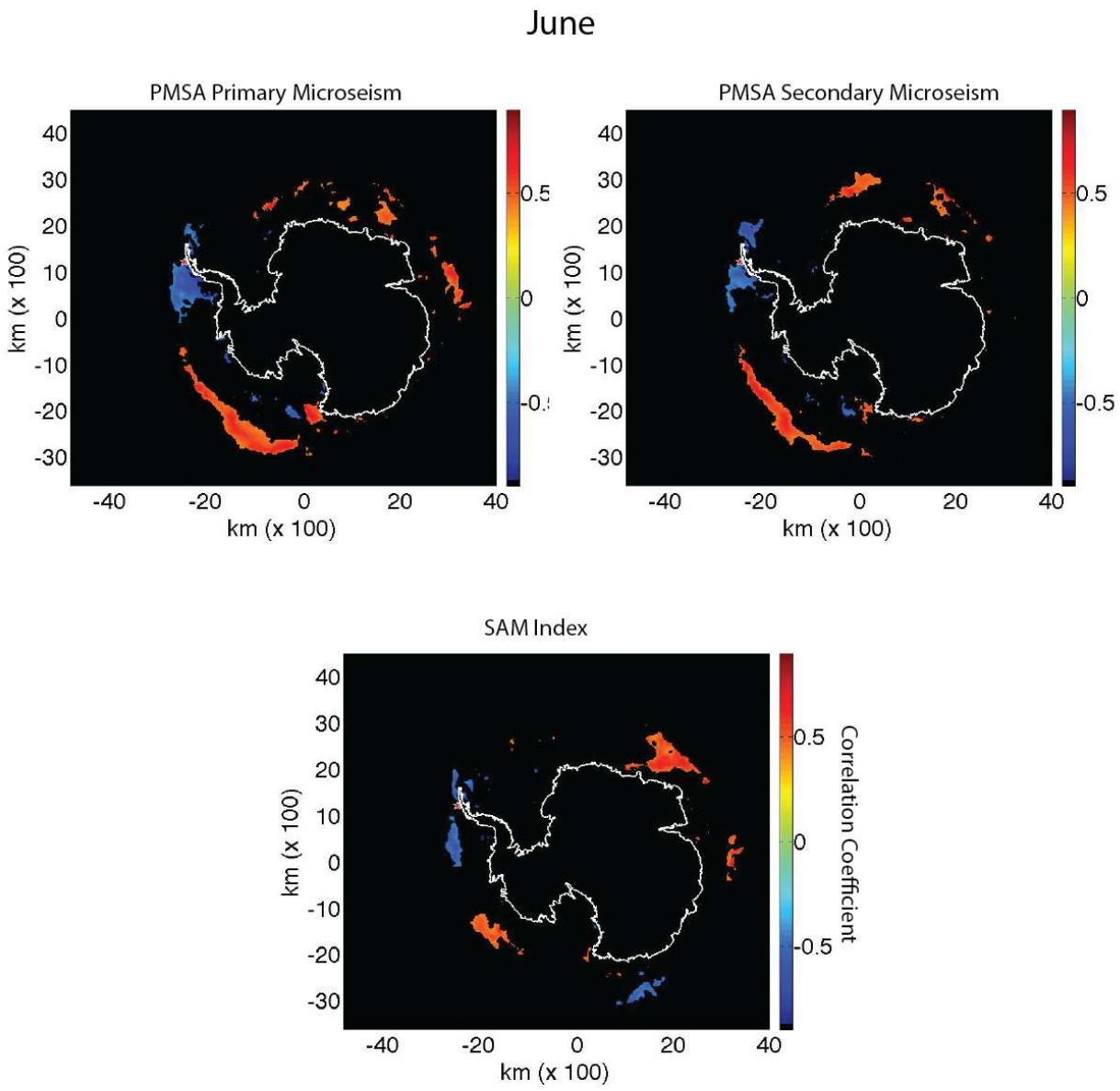

Figure A3.1. June correlations of monthly mean sea ice concentration with integrated primary and secondary microseism power recorded at PMSA (Red Star) and Southern Annular Mode (SAM) Index from 1993-2014. Blue regions indicate anticorrelation between sea ice and microseism/SAM metrics. Only correlations that exceed the 95th confidence interval as determined by two-tail t-test are plotted.

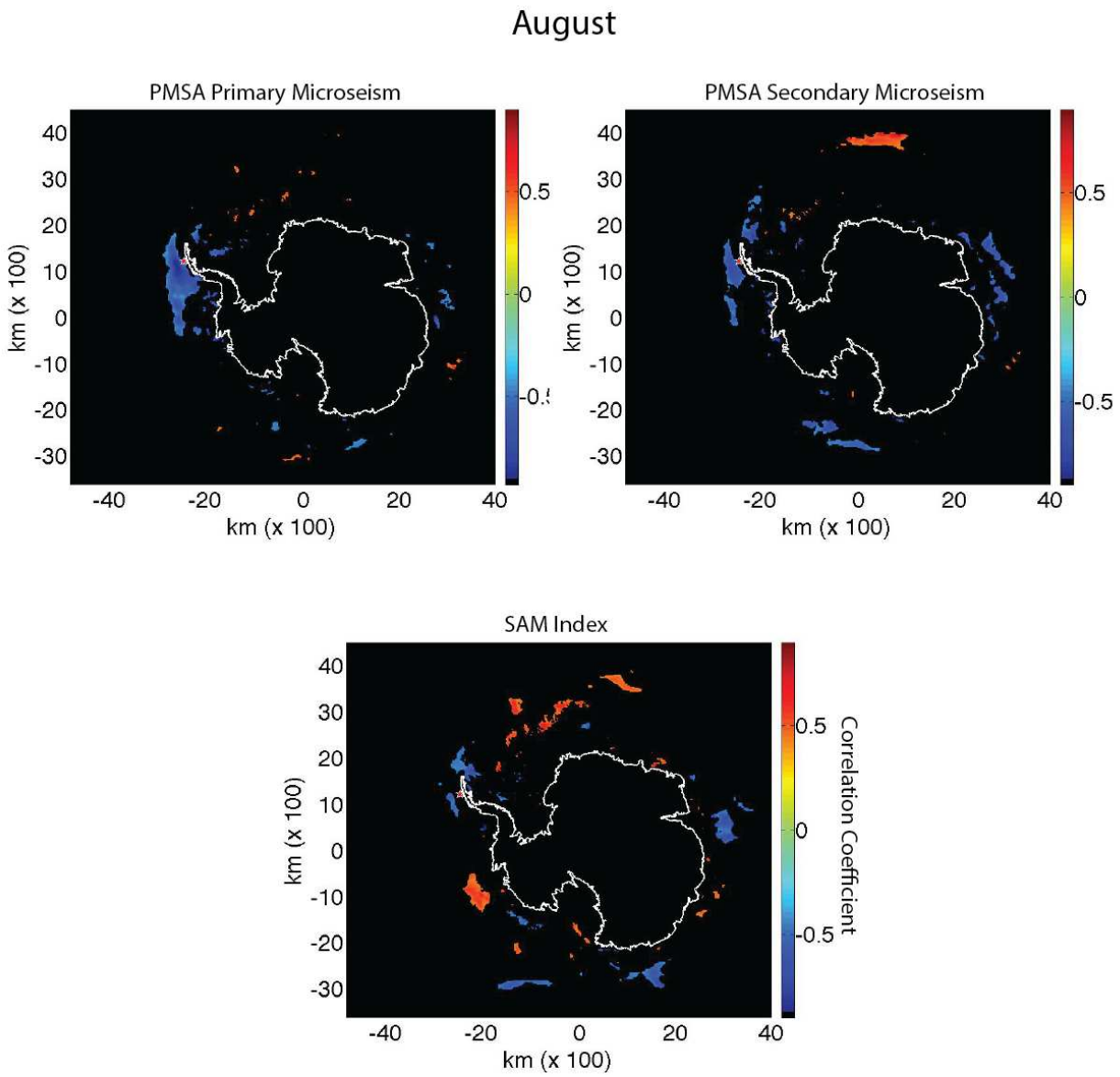

Figure A3.2. Same as figure A3.1, but for the month of August.

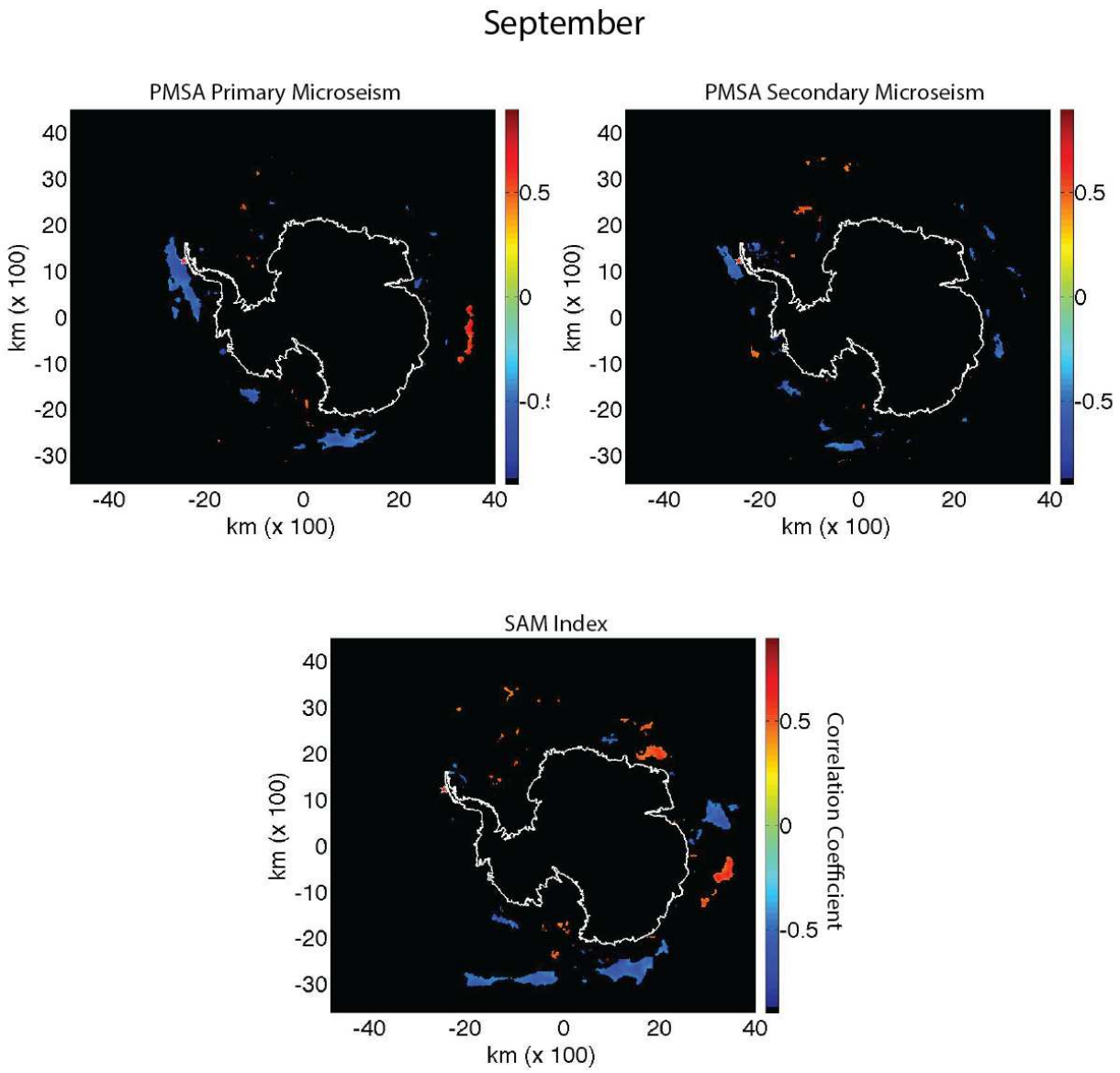

Figure A3.3. Same as figure A3.1, but for the month of September.

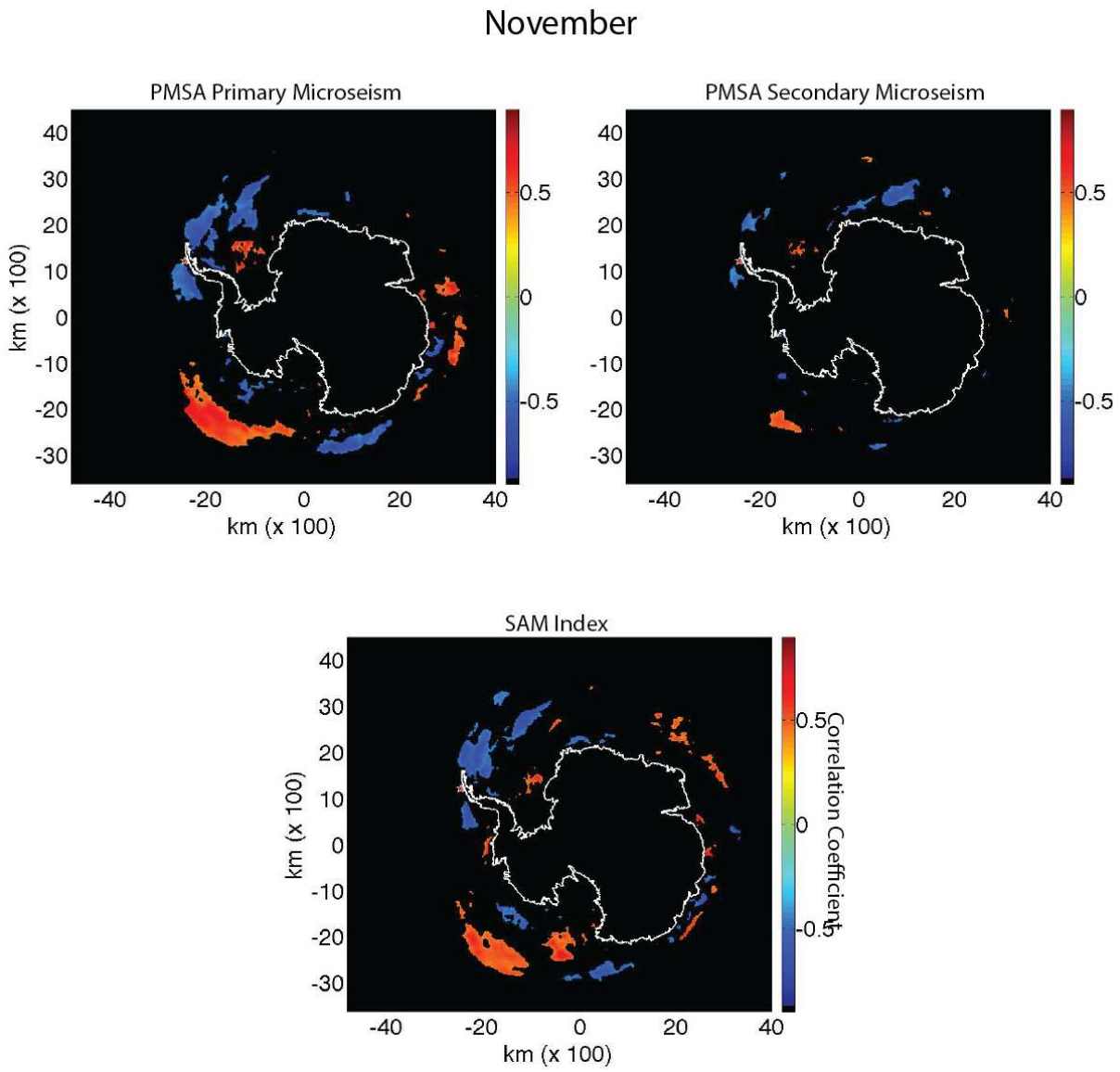

Figure A3.4. Same as figure A3.1, but for the month of September. Note the similarities between the primary microseism and SAM Index maps, further suggesting that wave state in the Drake Passage is exceptionally coupled to phase of the SAM.

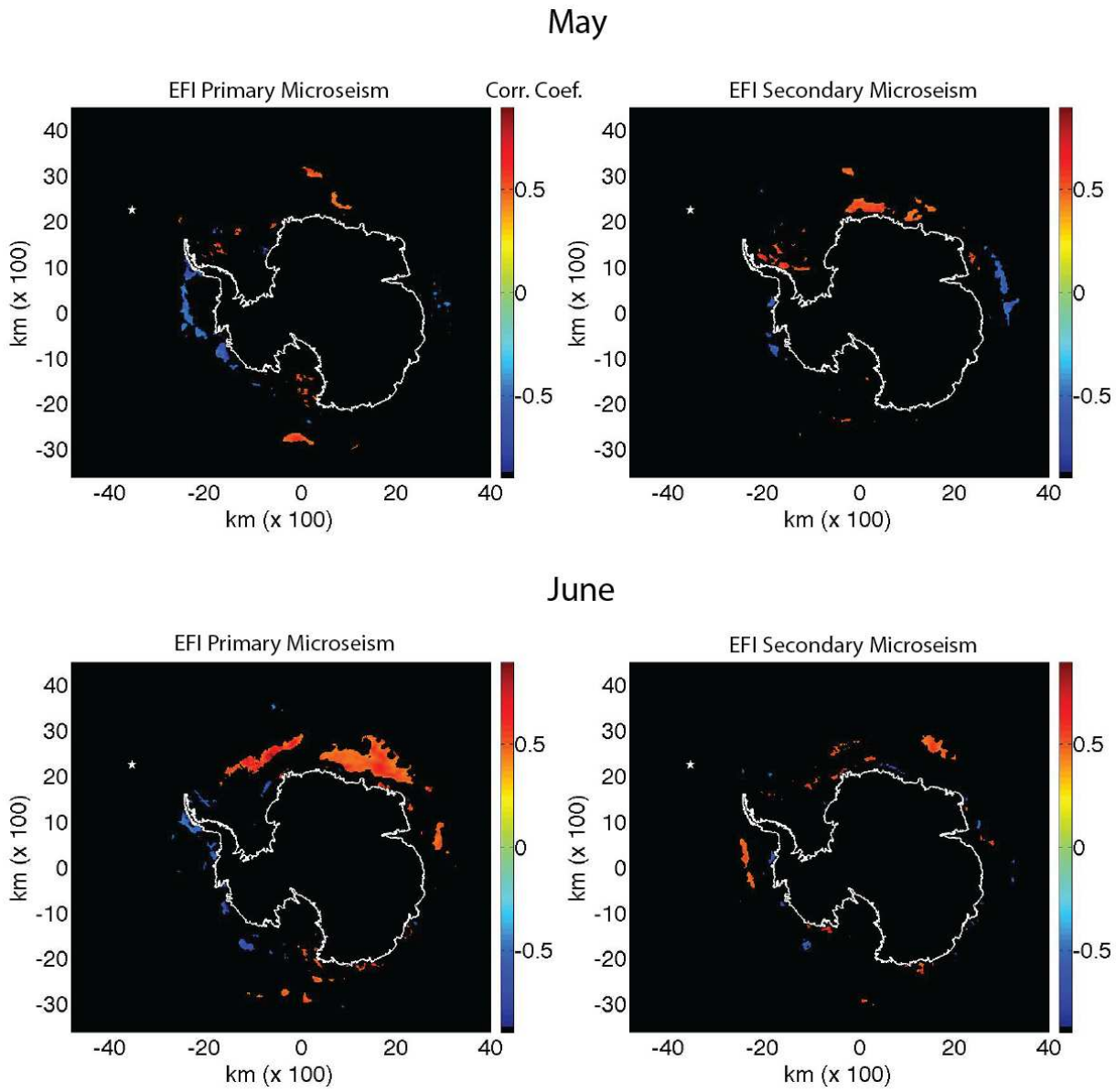

Figure A3.5. May and June correlations of monthly mean sea ice concentration with integrated primary and secondary microseism power recorded at EFI (White Star) from 1996-2014. Blue regions indicate anticorrelation between sea ice and microseism/SAM metrics. Only correlations that exceed the 95th confidence interval as determined by two-tail t-test are plotted.

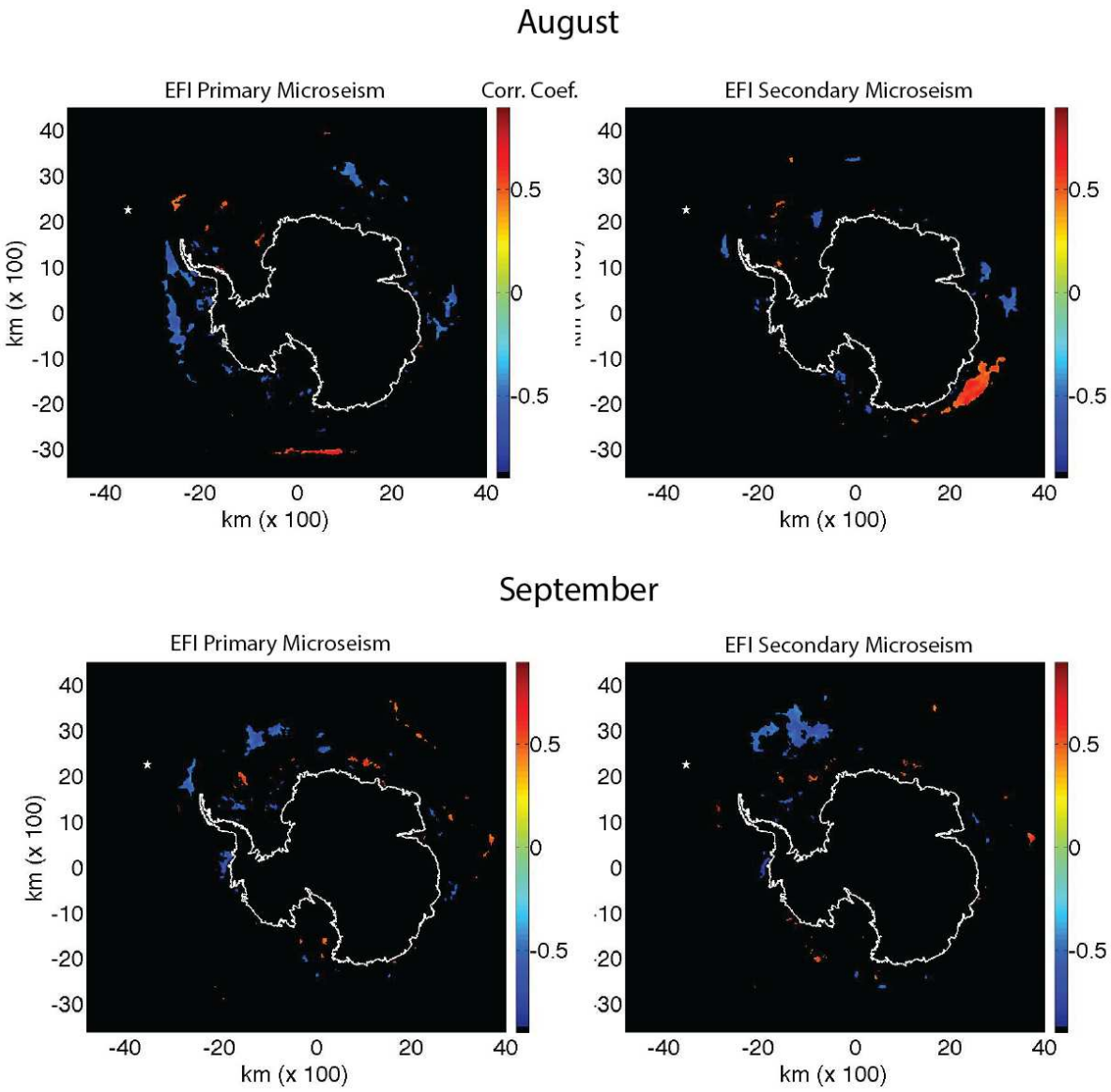

Figure A3.6. Same as figure A3.5, but for the months of August and September.

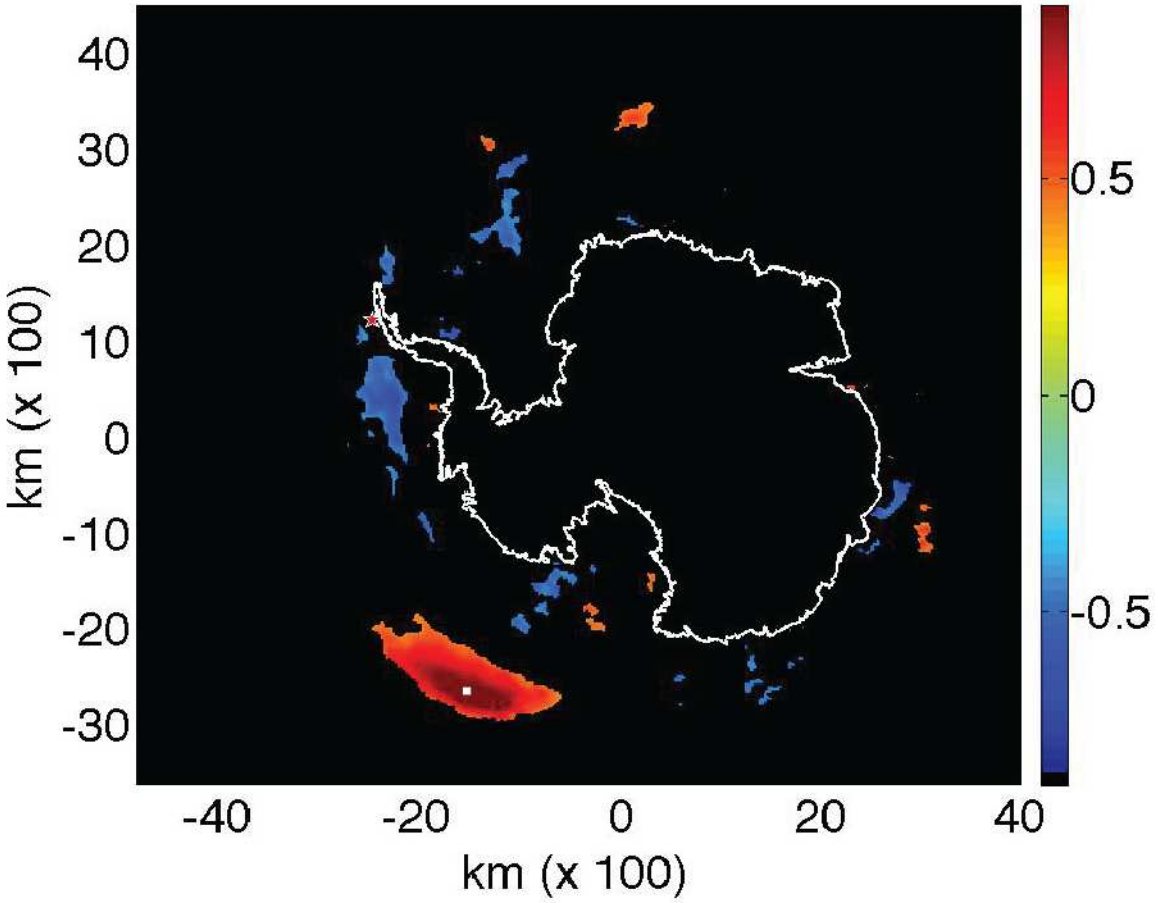

Figure A3.7. November correlations of monthly mean sea ice concentration in the Southern Ocean with sea ice concentration at a single grid point (white box) for 1993-2014. Only correlations that exceed the 95th confidence interval as determined by two-tail t-test are plotted.